CHARACTERIZATION OF A HYPERSPECTRAL CHROMOTOMOGRAPHIC IMAGING GROUND SYSTEM

THESIS

Chad B. Su'e, Captain, USAF

AFIT/EE.ABET/ENP/12-M03

DEPARTMENT OF THE AIR FORCE
AIR UNIVERSITY

AIR FORCE INSTITUTE OF TECHNOLOGY

Wright-Patterson Air Force Base, Ohio

AFIT/EE.ABET/ENP/12-M03

CHARACTERIZATION OF A HYPERSPECTRAL CHROMOTOMOGRAPHIC

IMAGING GROUND SYSTEM

THESIS

Presented to the Faculty

Department of Electrical and Computer Engineering

Graduate School of Engineering and Management

Air Force Institute of Technology

Air University

Air Education and Training Command

in Partial Fulfillment of the Requirements for the

Degree of Master of Science in Electrical Engineering

Chad B. Su'e, BSEE

Captain, USAF

March 2012

AFIT/EE.ABET/ENP/12-M03

CHARACTERIZATION OF A HYPERSPECTRAL CHROMOTOMOGRAPHIC IMAGING GROUND SYSTEM

Chad B. Su'e, BSEE
Captain, USAF

Approved:

//signed//	March 2012
Lt Col Michael Hawks, PhD (Chairman)	Date
//signed//	March 2012
Jonathan T. Black, PhD (Member)	Date
//signed//	March 2012
Maj Milo W. Hyde, PhD (Member)	Date
//signed//	March 2012
Glen P. Perram, PhD (Member)	Date
//signed//	March 2012
Eric D. Swenson, PhD (Member)	Date

AFIT/EE.ABET/ENP/12-M03

Abstract

A field-deployable hyperspectral chromotomographic imager has been developed and tested as a risk-reduction prototype to assist design of a space-based system. The instrument uses a high-speed video camera looking through a rotating direct-vision prism to simultaneously observe the full field of view in all visible wavelength channels. This enables hyperspectral imaging of transient events at high temporal resolution. The chromotomographic process multiplexes the spectral and spatial so an advanced reconstruction algorithm is required to separate the spectral channels.

A physics-based model of the instrument was developed to assist in future trade-space choices for design of the spaced-based system. Additionally, the model is used for the development and assessment of the filtered backprojection reconstruction algorithm. The model is used to simulate various scenarios and gauge the reconstruction algorithm's performance. An assessment on how the reconstruction algorithm performs under chromatic and monochromatic aberrations is included.

Laboratory experiments from the field-deployable instrument were collected, and the results are compared to physics-based model predictions. Prior to reconstructing scenes collected by the field instrument, a transverse offset resulting from an imperfection of the direct-vision prism was characterized and corrected. Results from the simulated and experimental data show that the instrument and algorithm are capable of detecting spectral and spatial information of complex scenes.

Acknowledgements

Table of Contents

List of Figures

List of Tables

List of Abbreviations

AFIT Air Force Institute of Technology
CTEx chromotomography experiment
CT computed tomography
CTI chromotomographic imager
DDE Dynamic Data Exchange
DVP direct-vision-prism
EO electro-optic
FBP filtered backprojection
FFT Fast Fourier Transform
FPA focal plane array
FPN fixed-pattern noise
FOV field-of-view
FS Field Stop
FTS Fourier Transform Spectrometer
FWHM full-width half-maximum
GCTEx ground-based chromotomographic experiment
HSI hyperspectral imager
IR infrared
ISS International Space Station
LMSE Laplacian Mean Square Error
LWIR longwave infrared
MSE Mean Square Error
MTF Modulation Transfer Function
MWIR midwave infrared
NIR near infrared
POCS Projection Onto Convex Sets
PSF point spread function
PTF Phase Transfer Function
OTF Optical Transfer Function
QE quantum efficiency
SCTEx spaced-based chromotomographic experiment
SNR signal-to-noise ratio
STF System Transfer Function
SVD Singular Value Decomposition
SWIR shortwave infrared
VIS visible

CHARACTERIZATION OF A HYPERSPECTRAL CHROMOTOMOGRAPHIC
IMAGING GROUND SYSTEM

1. Introduction

This thesis presents a physics-based model and experimental validation of the ground-based chromotomographic experiment (GCTEx) developed by the Air Force Institute of Technology (AFIT). The optical model is constructed using Zemax and MATLAB. The model provides the mechanism required to analyze future trade-space engineering choices for the design of the space-based system.

Previous work done at AFIT resulted in models [9, 28] and reconstruction algorithms [16, 18] using ideal optics. However, it is apparent that the GCTEx instrument is not ideal and optical aberrations coupled with systemic errors are present [35–37]. These systemic errors and aberrations limit the spectral and spatial performance of the GCTEx.

There are three primary objectives of this research: development of a physics-based model that allows for controlled amounts of systemic error and aberrations, the evaluation of how systemic errors and aberrations impact the reconstruction algorithm, and experimental validation of the physics-based model.

1.1 Motivation

This thesis focuses on one field of remote sensing known as hyperspectral imager (HSI). Hyperspectral imaging detects both the spatial and spectral content from an observed scene. Conventional HSI devices, such as scanned-slit or optical-filtered, are well-suited to observe static or slowly varying scenes and are commonly used

in air and space surveillance. However, these HSI devices have a limited ability to observe scenes that vary quickly. A capability gap throughout HSI devices exists for capturing all the spatial and spectral information of transient events (phenomenology varying more than 10 Hz). One application of collecting all aspects of transient events, such as bomb detonations, allows quick battle damage assessment or detection for secondary detonations. Using a direct-vision-prism (DVP) and a high-speed camera, hyperspectral chromotomographic imagers simultaneously observe the full field-of-view (FOV) in all spectral channels necessary to capture these transient events.

1.2 Hyperspectral Remote Sensing

Hyperspectral remote sensing combines two sensing modalities: imaging and spectrometry. An imaging system captures a picture of a remote scene related to the spatial distribution of the power of reflected and/or emitted electromagnetic radiation integrated over some spectral band. Spectrometry measures the variation in power with the wavelength or frequency of light, which captures information related to the chemical composition of the materials measured. The instrumentation used to capture such spectral information is called a spectrometer. Hyperspectral imaging sensors are able to simultaneously capture both the spatial and spectral content of remote scenes.

Hyperspectral imagers collect radiation from the electro-optic (EO)/infrared (IR) spectral regions, defined as the a portion of the electromagnetic spectrum that nominally ranges from 0.4 to 14 micron wavelength (20 to 750 THz frequency). The electromagnetic radiation is often segmented into five spectral regions:visible (VIS) from 0.4 to 0.7 μm, near infrared (NIR) from 0.7 to 1.1 μm, shortwave infrared (SWIR) from 1.1 to 3.0 μm, midwave infrared (MWIR) from 3 to 5 μm, and longwave infrared (LWIR) from 5 to 14 μm. The spectral region in which hyperspectral imagers

operate is dependent on the object of interest.

For the purposes of this thesis, all objects will be considered passively, vice actively, illuminated. Passive objects use two primary sources of radiation: reflected light and/or self emission from the objects in the scene. Bomb detonations or muzzle flashes are examples of passive sources that self-emit. Reflected sunlight is the dominant radiation source in the VIS, NIR, and SWIR, while thermal emission dominates in the LWIR. Key components of the HSI are selected based on what spectral region the object is best observed at. In general, it more difficult to capture targets in the LWIR region vice the VIS. The primary cause is detectors, or focal plane arrays (FPAs), made for the LWIR are sensitive to objects that have temperatures near room temperature. The FPA, imaging optics, and support equipment must be cooled such that it does not generate signal to overwhelm signal produced by the scene.

Hyperspectral imagers produce data commonly referred to as a hypercube, which, as depicted in Figure 1.1(a), is a three-dimensional data set composed of layers of grayscale images.

(a)   (b)
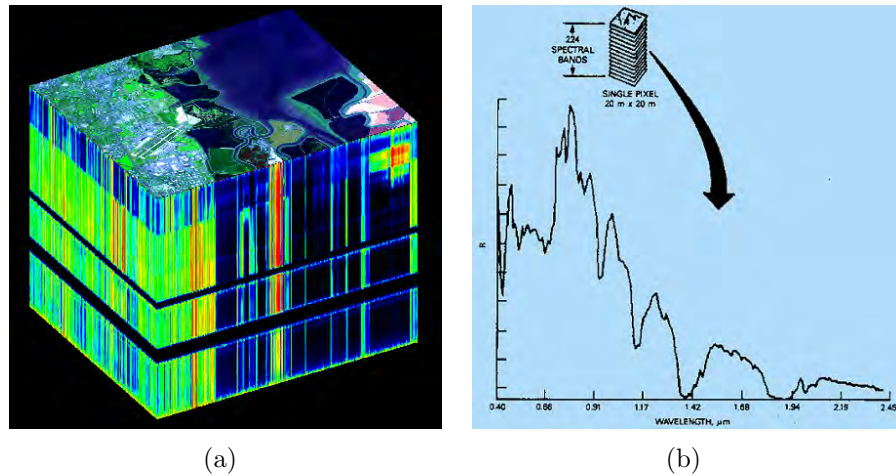
Figure 1.1. (a) Hypercube taken from AVIRIS platform over Moffet Field, CA. (b) Example of the spectrum obtained from a single pixel of the hypercube. [26]

As shown in Figure 1.1(b), each pixel of the hypercube contains a finely sampled spectrum whose features are related to the materials contained within it. Each layer is a spectral band is referred to as a bin. The ability to capture a continual spectrum as opposed to more discrete set of often discontinuous spectral bands distinguishes a hyperspectral imager from a multispectral imager.

1.3 Research Goals

This research complements previous work undertaken by AFIT which has the end goal of fielding a hyperspectral chromotomographic imager (CTI) aboard the International Space Station (ISS). This thesis focuses on developing, evaluating, and validating a physics-based model suitable for future trade-space choices in the design of the space-based system. Furthermore, this research demonstrates how optical aberrations and systemic errors impact the spatial and spectral resolution. Specific goals addressed in this thesis include:

- Further progress the development of the ground-based CTEx instrument
  - Fix the electronics system to accurately log prism angles with camera data
  - Automate the reconstruction process, no manual corrections to produce hypercubes
- Develop model for trade studies for space system
- Investigate the effect of aberrations impact the system performance
- Determine the operating modes/limits of the system and the reconstruction algorithm
- Collect laboratory and field data to demonstrate the utility of a CTI

1.4 Organization

Chapter 2 provides an overview of the optical concepts and that are used throughout the thesis. Furthermore, Chapter 2 also tackles the analytical expressions that

govern the device and an overview of the reconstruction algorithm. Chapter 2 concludes with a detailed overview of AFIT's GCTEx. Chapter 3 is a development of the physics-based models made from the combination of Zemax and MATLAB. The validation of the models and the source of the transverse offset is also explained. Chapter 4 is an assessment of the reconstruction algorithm from a variety of simulations. Laboratory data collected from the GCTEx is also presented. Chapter 5 concludes this thesis summarizing key results and recommendations for future research.

2. Background

This chapter provides an overview of the concepts used to construct the simulation and reconstruction algorithm. The beginning sections cover the foundation of linear system theory, basic principles of Fourier optics, and how aberrations impact the optical system. The following section is a brief overview of conventional hyperspectral imagers and how a trade study of how they are capable of measuring transient events compared to CTIs. The principles of the hyperspectral chromotomographic imager operation, development reconstruction algorithm, and its performance limits are then covered. Finally, a detailed overview the AFIT GCTEx instrument is given.

2.1   Linear Systems Theory of Optical Systems

These two sections briefly cover the basic principles of optical linear system theory and Fourier optics. See the texts by Holst and Lomheim [23] and Goodman [15] for a thorough treatment. Linear system theory was developed for electronic circuitry and has been extended to optical, electro-optical, and mechanical systems [23]. For a system to be linear, it must meet the principles of superposition and homogeneity. Optical linear systems make use of the property known as *shift invariance* to calculate how images are formed from objects. Shift invariance states that a shift of the input causes a corresponding shift in the output. For electronic circuits, the shift is in time, whereas for optical systems, the shift is in space. For example, with an imaging system, as a target moves from the top of the field of view to the bottom, the image also moves from the top to the bottom.

Goodman showed that when an optical system produces an image using incoherent light (the phase of the source is a random variable), then the function which describes the intensity in the image plane produced by a impulse in the object plane is called

the point spread function (PSF) [15]. The object is represented as a sum of impulses within its boundaries. The object, $o(x, y)$, is modeled as a series of weighted Dirac delta functions. For small increments, the response to these impulses, $h(x, y)$, form the image intensity distribution, $i(x, y)$ given by the convolution integral

$$i(x, y) = \int_{-\infty}^{\infty} \int_{-\infty}^{\infty} o(x', y') h\{\delta(x - x')\delta(y - y')\} \mathrm{d}x' \mathrm{d}y'. \tag{2.1}$$

Equation (2.1) is symbolically represented by the two-dimensional convolution operator,

$$i(x, y) = o(x, y) \otimes h(x, y), \tag{2.2}$$

and by transforming to the Fourier domain the convolution becomes a multiplication

$$I(u, v) = O(u, v) H(u, v). \tag{2.3}$$

The function $H(u, v)$ is called the Transfer Function and in the case of optical systems, it is known as the Optical Transfer Function (OTF). The OTF is a complex valued function, composed of real and imaginary parts:

$$OTF(u, v) = |H(u, v)| \, e^{j\phi(u,v)}. \tag{2.4}$$

The real portion is the modulus of $H(u, v)$ and is called the Modulation Transfer Function (MTF). The MTF is the ratio of output modulation to input modulation normalized to unity at zero frequency. The phase, $\phi(u, v)$ is termed Phase Transfer Function (PTF). The impact of the PTF is significant to the response of the optical system; however, the MTF is more effective in describing the optical system's performance.

2.1.1 Modulation Transfer Function.

Modulation Transfer Functions provide an objective mechanism for describing the optical system's ability to resolve spatial content. Additionally, individual subsystems, such as lenses and mirrors, have their own MTF which can be cascaded with all other the system components to yield the system MTF. Figure 2.1 is a normalized, diffraction-limited MTF of a symmetrical optical system with a circular aperture.
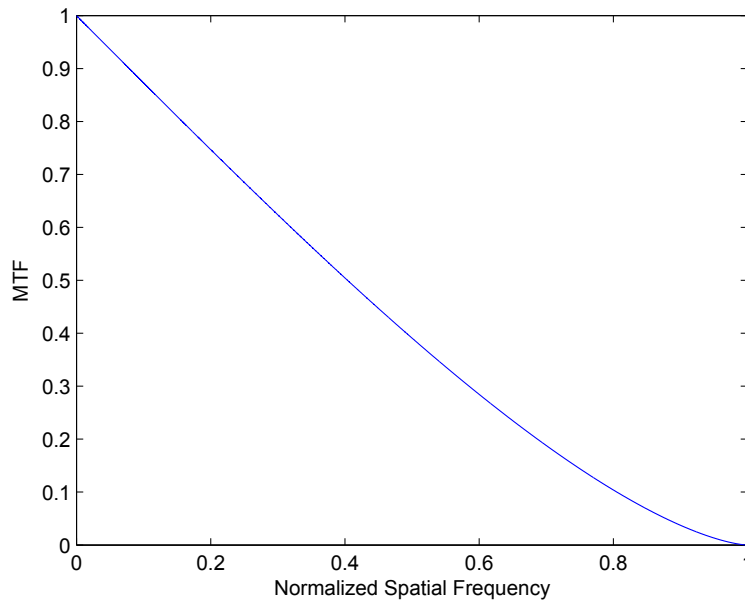
Figure 2.1. MTF of a diffraction-limited system with frequency normalized to the cutoff frequency, assuming a circular aperture.

The horizontal axis indicates the spatial frequency, typically specified in lines/mm, for which the optical system can resolve. The vertical axis is the amount of modulation, or contrast, defined as

$$Modulation = \frac{I_{max} - I_{min}}{I_{max} + I_{min}}. \tag{2.5}$$

The variables I_{max} and I_{min} are the maximum and minimum signal levels, respectively.

I_{max} is the maximum intensity produced by an image (white) and I_{min} is the minimum intensity (black). As the frequency increases, the amount of modulation decreases, assuming a clear aperture and no apodization is applied. The highest input frequency that can be resolved is defined as the cutoff frequency, f_c. For a circular aperture and incoherent imaging, the cutoff frequency is

$$f_c = \frac{D}{\lambda f_{eff}} = \frac{1}{\lambda F/\#}, \tag{2.6}$$

where f_{eff} is the optical system effective focal length and D is the entrance pupil diameter. The F-number, $F/\#$, is the ratio of the effective focal length over the entrance pupil

$$F/\# = \frac{f_{eff}}{D}. \tag{2.7}$$

Because the cutoff frequency is wavelength dependent, polychromatic MTFs are calculated individually for all the wavelengths of interest.

A diffraction-limited system is the theoretical best performance for an optical system to achieve. If a point source was imaged by a diffraction-limited system with a circular aperture, an Airy disk pattern would form on the image plane. The Rayleigh Criterion [22] states that this in order to resolve two points, the minimum distance, r, between the peaks is given by

$$r = 1.22\frac{\lambda f_{eff}}{D} = 1.22\lambda F/\#. \tag{2.8}$$

Aberrations within an optical system will degrade, and thereby lower the MTF response below the diffraction limit. Aberrations may have a significant impact on the performance of the optical system.

9

2.2 Aberrations

Aberrations are the result of optical components having non-ideal characteristics from those set by Gaussian optics. Gaussian optics make use of the paraxial approximation to assume that all light rays from one point of the object through the optical system converge to, or diverge from, a single point. Aberrations fall into two primary categories: chromatic and monochromatic. Monochromatic aberrations are often associated with the geometry of the optical component resulting in rays that do not converge to a single point. Seidel aberrations are often used to describe these monochromatic aberrations. Chromatic aberrations are the result of the wavelength dependence in the index of refraction. Chromatic aberrations primarily exist in only lens-based optical systems. The following sections provide an overview of aberrations, see the text by Hecht [22] for in-depth coverage.

2.2.1 Chromatic Aberrations.

The velocity of light changes when it passes through different mediums. Short wavelengths travel slower in glass than long wavelengths causing the colors to disperse. Chromatic aberrations are the result of this dispersion. In some applications, this dispersion is desirable such as prisms. However, for most image-forming optical systems, chromatic aberrations cause the focus to vary as a function of wavelength. This usually results in the optical system to be in focus for a narrow band of wavelengths leaving the other wavelengths to be defocused.

Achromatic lenses are a method of correcting for chromatic aberrations. By combining sets of low dispersion and high dispersion lenses, the effects of the chromatic aberrations can be reduced. However, it becomes exceedingly difficult to design an achromatic lens systems over a large spectral range. Commonly mirrors are used to avoid the detrimental effects of chromatic aberrations.

2.2.2 Seidel Aberrations.

Seidel aberrations are the result of incorporating an additional term from the Taylor series expansion made in the paraxial approximation. There are five Seidel aberrations: spherical, coma, astigmatism, field curvature, and distortion. Defocus and tilt are first-order aberrations often included in the Seidel aberrations.

Seidel aberrations are useful metrics for designing optical systems to gauge system performance. The Seidel aberrations are a function of object's location in terms of exit pupil coordinates, polarmetrically described by ρ and θ, along with a field-height dependence, h. The Seidel aberrations are summarized in Table 2.1.

Table 2.1. First-order and Seidel Aberrations.

Description	Term
Focus	$W_{020}\rho^2$
Tilt	$W_{111}h\rho\cos(\theta)$
Spherical Aberration	$W_{040}\rho^4$
Coma	$W_{131}h\rho^3\cos(\theta)$
Astigmatism	$W_{222}h^2\rho^2\cos(\theta)^2$
Field Curvature	$W_{220}h^2\rho^2$
Distortion	$W_{311}h^2\rho^2\cos(\theta)^2$

The coefficients in front of each term describe the severity of the aberration on the system. The weight of the Seidel coefficient is based upon the optical path difference caused by the aberration in terms of the wavelength of interest. It is often convenient to measure and describe aberrations in terms of a wavefronts. A method for describing the shape of the wavefront is known as the Zernike Polynomials discussed in the next section.

2.2.2.1 Zernike Polynomials.

The Zernike polynomials are a set of orthogonal functions that are useful for representing wavefront aberrations. They describe most real-world optical surfaces or wavefronts to be represented as a short string of coefficients. Interferometers often output their measurements in terms of Zernike polynomials. Additionally, they have convenient mathematical properties [45]:

- Continuous and orthogonal when used over a circular-shaped domain

- Complete basis set, any well-behaved function is described by a linear combination of Zernike polynomials

- Rotationally symmetric

- Computationally efficient being polynomial in form

Zernike polynomials arise in the expansion of a wavefront function for optical systems with circular pupils. The odd and even, respectively, Zernike polynomials are given by [42]

$$
\begin{aligned}
Z_n^{-m}(\rho, \theta) \\
Z_n^m(\rho, \theta)
\end{aligned}
= R_n^m(\rho) \frac{\sin}{\cos}(m\theta),
\tag{2.9}
$$

where θ is the azimuthal angle defined within $0 \leq \theta \leq 2\pi$ and ρ is the radial distance bounded between $0 \leq \rho \leq 1$. The radial function $R_n^m(\rho)$ is defined for n and m integers with $n \geq m \geq 0$ by

$$
R_n^m(\rho) = \begin{cases} \sum_{l=0}^{(n-m)/2} \frac{(-1)^l (n-l)!}{l!(\frac{1}{2}(n+m)-l)!(\frac{1}{2}(n-m)-l)!} \rho^{n-2l} & \text{for } n-m \text{ even} \\ 0 & \text{for } n-m \text{ odd} \end{cases}
\tag{2.10}
$$

Equations (2.9) and (2.10) are evaluated to produce the commonly used FRINGE set of Zernikes that is composed of 37 terms. The FRINGE polynomials a subset

of the standard Zernike polynomials developed by Born and Wolf [3] that have been arranged in a different order. Only the first nine terms are listed in Table 2.2 and like the Seidel aberrations they are represented polarmetrically of the pupil.

Table 2.2. First nine Zernike terms used to represent the first and third-order aberrations. [43]

Term #	n	m	Polynomial	Description
0	0	0	1	Piston
1	1	1	$\rho \cos(\theta)$	X-tilt
2	1	-1	$\rho \sin(\theta)$	Y-tilt
3	2	0	$2\rho^2 - 1$	Focus
4	2	2	$\rho^2 \cos(2\theta)$	Astigmatism @ 0° & Focus
5	2	-2	$\rho^2 \sin(2\theta)$	Astigmatism @ 45° & Focus
6	3	1	$\rho(3\rho^2 - 2) \cos(\theta)$	Coma & X-tilt
7	3	-1	$\rho(3\rho^2 - 2) \sin(\theta)$	Coma & Y-tilt
8	4	0	$6\rho^4 - 6\rho^2 + 1$	Spherical & Focus

In Table 2.2, the first 3 terms represent the first-order terms associated with Gaussian optics. Term 0 is a constant or piston term, while terms 1 and 2 are tilt terms and term 3 represents focus. The third-order aberrations are represented by terms 4 through 8. Terms 4 and 5 are astigmatism plus defocus and terms 6 and 7 represent coma plus tilt, while term 8 represents third-order spherical with focus. Terms 9 or higher represent the higher-order aberrations.

Wyant showed that by using a combinations of the first nine Zernike terms, the Seidel aberrations can be represented and are shown in Table 2.3 [43]. However, the Zernike terms have no dependence on field height so the representations are not *true* Seidel terms. Thus tilt and distortion are indistinguishable from one other. Additionally, field curvature appears to be focus, or vice versa.

The Zernike aberrations are used to add controlled amounts of aberrations into the simulation. Since Seidel aberrations are often used to evaluate optical system performance, the Zernike combinations listed in Table 2.3 are used.

Table 2.3. Zernike combinations equivalent to Seidel Terms. The Zernike combinations describe the magnitude and the phase terms have been excluded.

Seidel Coefficient	Zernike Combination	Description
W_{11}	$\sqrt{(Z_1 - 2Z_6)^2 + (Z_2 - 2Z_7)^2}$	Tilt
W_{20}	$2Z_3 - 6Z_8 \pm \sqrt{Z_4^2 + Z_5^2}$	Focus
	sign chosen to minimize absolute value of magnitude	
W_{22}	$\pm 2\sqrt{Z_4^2 + Z_5^2}$	Astigmatism
	sign opposite that chosen in focus term	
W_{31}	$3\sqrt{Z_6^2 + Z_7^2}$	Coma
W_{40}	$6Z_8$	Spherical

2.3 Hyperspectral Imagers

Hyperspectral imagers are broken into two categories: dispersive and interferometric. Each type has their own advantages which is dependent on the application. A brief overview on conventional HSI instruments and a trade study on how capable each are on capturing transient events is now given.

2.3.1 Fourier Transform Spectrometers.

A common interferometric HSI is the Michelson interferometer based Fourier Transform Spectrometer (FTS). One path of the Michelson interferometer is varied in length with respect to another using a beamsplitter and a set of mirrors. Figure 2.2 illustrates the hypercube generated from the FTS. As the mirror sweeps, thereby changing the optical path length, the resulting images of the changing interference patterns are then correlated with the Fourier transform of the spectrum of the scene.

Fourier Transform spectrometers offer high spectral resolutions but require time to sweep the mirror. Additionally, FTSs require very precise tuning of their optical path and therefore are susceptible to vibration and noise amplification. These disadvantages make FTSs less than ideal for capturing transient scenes.
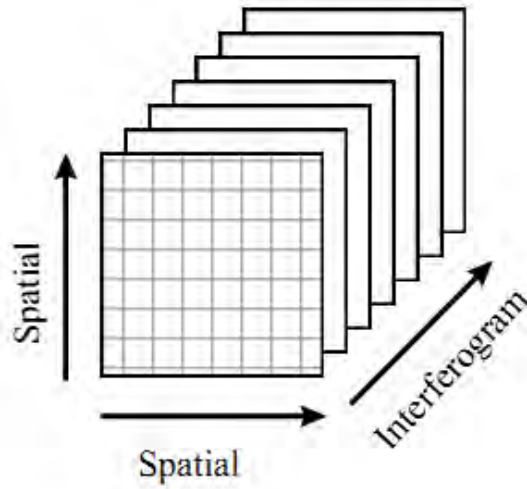
Figure 2.2. Data collected from FTS. Results are then converted into hypercubes using Fourier Transforms. [12]

2.3.2 Dispersive Spectrometers.

Diffraction gratings, prisms, or optical filters are the dispersive components often used in these spectrometers. Three classes of dispersive spectrometers are considered for capturing transient events: scanned-slit, optical filter, and tomographic. Each class collects hypercubes using different methods schematically represented in Figure 2.3.
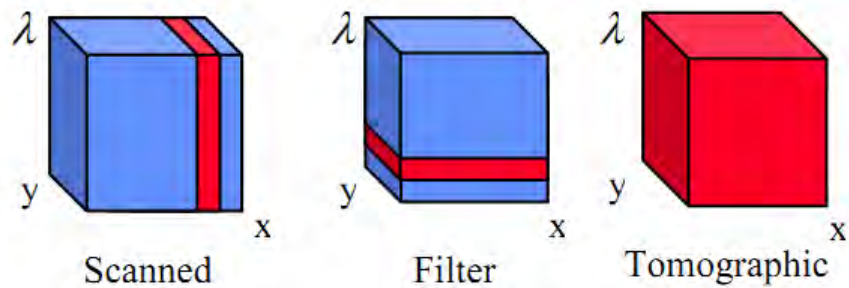
Figure 2.3. Example of the spectrum obtained from three classes of dispersive HSI devices. Scanned-slit and filter classes require scanning while the tomographic devices do not. [33]

15

The x-y plane represents the FPA and the red band is the spectral-spatial information collected at each measurement. Both the scanned and filter classes require multiple collections to capture the entire hypercube, while tomographic instruments capture the hypercube in one measurement. Each class is explained in the next sections.

2.3.2.1   Scanned-Slit Hyperspectral Imagers.

Scanned-slit hyperspectral imaging systems operate by dispersing the light from a slit onto the FPA. The slit is narrowly-sized to achieve high spectral resolution and is imaged onto one dimension of the FPA which is the x-axis of Figure 2.3. The dispersed light is spread over the other dimension, the y-axis, of the FPA. Figure 2.4 shows the concept of a conventional scanned-slit HSI.
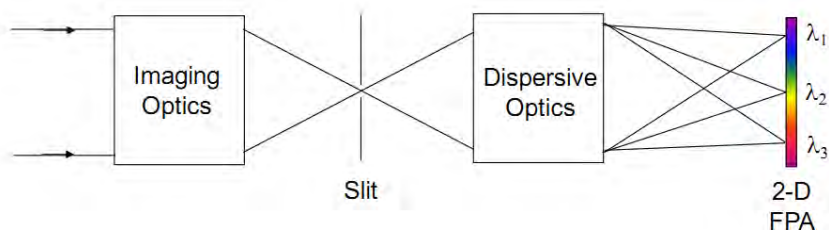
Figure 2.4. Concept of a scanned-slit HSI. The system images a slit and a dispersive element spreads the spectrum along one dimension of the FPA. [12]

To obtain a hypercube, these devices must scan for the remaining spatial dimension. These instruments use pushbroom or wiskbroom schemes aboard a moving platform, such as a satellite or aircraft, as the scanning mechanism. The use of a slit limits the area coverage at any given time and reduces the optical throughput therefore reducing the signal-to-noise ratio (SNR). Increasing the exposure interval remediates the lack of signal at the cost of system response. Both of these limitations restrict the ability to capture transient events.

2.3.2.2 Spectral Filters Hyperspectral Imagers.

Spectral filters capture two spatial dimensions and use a series of spectral bandpass filters to obtain the spectral content. The spectral performance is limited by the bandpass filters coverage. This method provides good area coverage and the ability to spatially capture the transient event. However, it must sweep through the spectral filters therefore cannot capture all the spectral information of transient events.

2.4 Chromotomographic Imagers

CTIs were first conceptualized by Russian scientists [13]. Since its concept, a significant amount of research focusing on the generation of proof-of-concept devices [11, 32]. See Mantravadi and Cain [30] for a more extensive history of chromotomographic imagers. AFIT began working on modeling chromotomographic instruments in 2004 and have since then constructed the GCTEx based off the design proposed by Mooney [31].

Unlike conventional HSIs, which require scanning or filtering in either the spatial or spectral dimensions to generate hypercubes, chromotomographic imagers capture all three dimensions (two spatial dimensions and one spectral) simultaneously. Chromotomography use a dispersive element, either a prism or diffraction grating, to project the three-dimensional object cube onto the two-dimensional FPA. The results of the projections are illustrated in Figure 2.5.

As shown in Figure 2.5, the image formed at one wavelength is multiplexed with the images formed at all the wavelengths over the spectral range of the dispersive element. All information of the object cube is captured simultaneously, no loss of information due to scanning or filtering occurs, making chromotomographic imagers ideal for capturing transient events. In order to generate hypercubes of the object, projections from multiple angles are required. Furthermore, a complex reconstruction
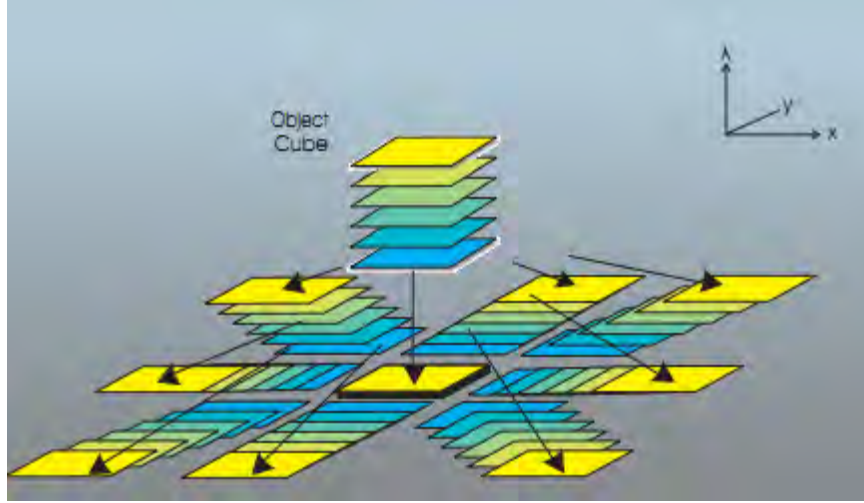
Figure 2.5. Chromotomography takes a 3D object cube and projects the information onto a 2D detector array. The varying colors represent each spectral bin of the object cube. This figure illustrates a diffraction-based chromotomgraphic imager where a set number of projections are spread spectrally. In the center of the detector, the object cube is not dispersed.

algorithm is necessary. Chromotomographic imagers offer the following advantages over conventional HSIs:

- no slit or filtering required therefore high throughput enabling lowered SNR constraints

- high temporal resolution due to the lack of a scanning mechanism

Diffraction grating chromotomographic imagers have been successfully demonstrated [11, 19]. They offer the advantage of being able to provide multiple projections instantaneously which may be advantageous for capturing transient events. However, Mantravadi demonstrated in simulated scenarios that prism-based chromotomographic imagers offer higher spectral resolution than diffraction-based ones [29]. High spectral resolution is required for classification of detonation events [4]. Thus, the focus of this thesis is on chromotomographic imagers that use prisms as the dispersive element.

2.4.1 Principles of Operation.

Chromotomographic instruments operate under similar principles as medical computed tomography (CT) instruments. Like medical CT instruments, projections collected at multiple angles are used to reconstruct a three-dimensional cube from two-dimensional detectors. However, the third dimension in chromotomography cubes is spectral rather than spatial [13].

Figure 2.6 shows the optical layout of the CTI which uses a rotating DVP to achieve varying spectral dispersion. As shown in the figure, the object is imaged through the optical system and results in a 3-channel hypercube. Figure 2.6 demonstrates that the hypercube has been separated into its red, green, and blue components.
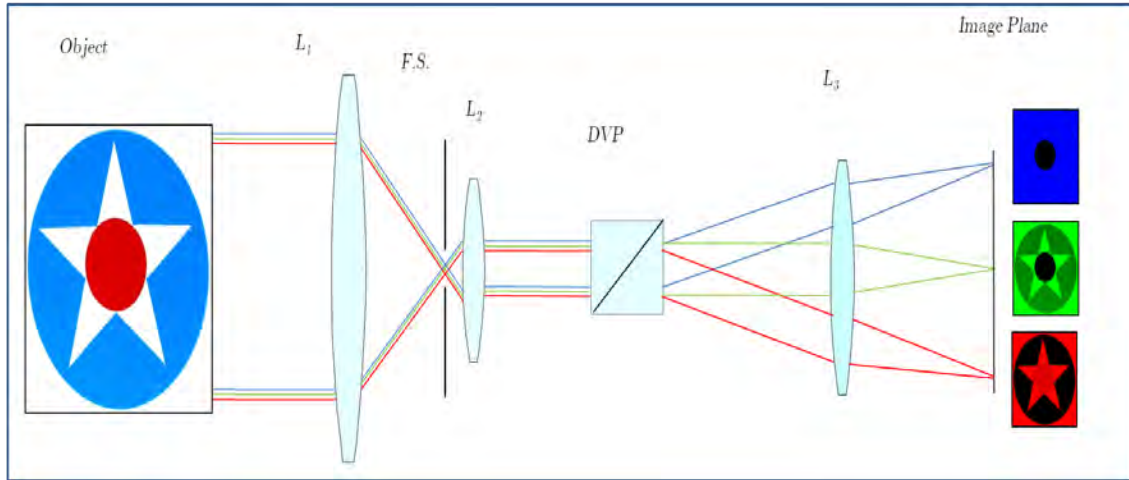
Figure 2.6. Optical layout of the CTI system using a rotating Direct Vision Prism to vary the spectral dispersion.

The telescope segment of the CTI consists of two lenses, L_1 and L_2, spaced to the sum of each focal length thereby by making it afocal. Assuming that the incoming light into the first lens is collimated, the light refracted by the second lens once again becomes collimated and angular magnification is produced. A Field Stop (FS) is

placed on the intermediate image plane at the focal length of L_1. Since the prism spreads the object, a field stop is required to ensure the imaged object does not exceed the dimensions of the FPA. The collimated light is then dispersed by the prism and then is imaged by the focusing lens, L_3, onto the FPA.

The prism rotates the spectral contents about the undeviated wavelength, shown in green. With each integration time, a single object cube projection is collected. Mooney [31] showed that the radial shift from the center of the FPA, referred to as the spectrometer constant, k, is defined as

$$k(\lambda) = f_3 \tan \gamma(\lambda), \tag{2.11}$$

where f_3 is the focal length of the focusing lens and γ is the dispersion of the prism as a function of wavelength.

Since the collected data has spatial and spectral information interlaced with one another, a reconstruction algorithm is required to deconvolve the spectral information. The following section discusses the reconstruction algorithm.

2.5   Reconstruction

The single greatest deficiency in chromotomographic imager's performance is caused by the *limited-angle* problem. Due to the nature of device operation coupled with the central slice theorem, a missing cone of information is formed preventing all of the object cube from being collected. In order to produce reliable results, reconstruction algorithms must fill in this missing information. Therefore, it is imperative that a full understanding of the central slice theorem and missing cone be developed. This section is then followed by the analytical expressions that are common amongst the reconstruction algorithms.

2.5.1 Central Slice Theorem.

The Fourier slice theorem, commonly referred to as the central slice theorem, is the fundamental theory that governs tomographic systems. The central slice theorem is defined as [24]:

Definition. *The Fourier transform of a parallel projection of an object f(x, y) obtained at angle θ equals a line in a 2D Fourier transform of f(x, y) taken at the same angle.*

By performing the Fourier transform on a projection, a line through the center in the 2D Fourier transform of the object is obtained. Figure 2.7 is an example of the central slice theorem of a image collected by a medical CT instrument.
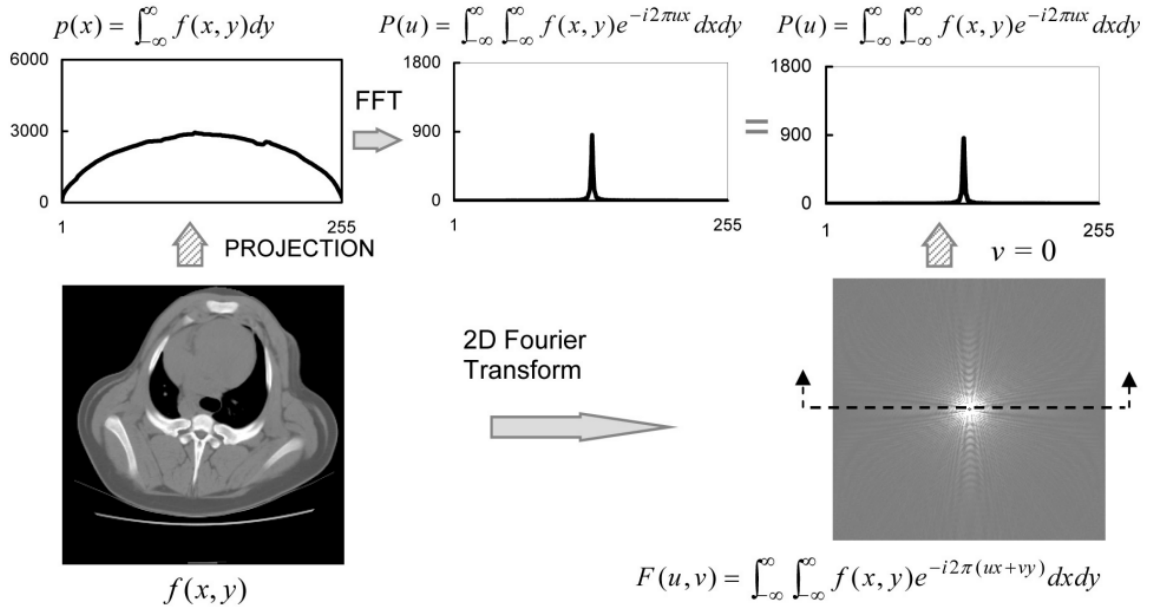
Figure 2.7. Illustration of central slice theorem for a single projection collected. The Fourier transform of the projection is equal to a line through the center in the 2D Fourier transform of the object. [24]

If a sufficient number of projections is collected over the range from 0 to π, the entire Fourier space of the object being reconstructed is filled. Once the object's

Fourier transform is obtained, the object can be fully recovered by taking the inverse Fourier transform. The tomographic reconstruction process is a series of 1D Fourier transforms followed by a 2D inverse Fourier transform.

2.5.2   The Missing Cone.

The central slice theorem extends to three dimensions. For a object cube, the 2D Fourier transform of the tomographic projection is equal to the 3D Fourier transform of the image evaluated on a plane through the origin in a direction perpendicular to the projection bean [6], this is called the x-ray projection plane. The projection beam angle is controlled by the spectrometer constant defined in Equation (2.11). Figure 2.8 depicts how the object cube creates tomographic projections onto the detector via the x-ray transform. The recovery of a 3D distribution from 2D projections is known as the x-ray transform [11].

Similar to the 2D CT reconstruction discussed in Section 2.5.1, the entire 3D Fourier space of the object needs to be filled to reconstruct the object cube. By rotating the prism, different slices through the origin are obtained. However, the same projection beam angle remains constant throughout all the prism rotations. The constant projection beam and failure to fill in the entire 3D Fourier space is known as the *limited-angle* problem for tomographic instruments.

In the limit of an infinite number of different projections, the projections will define a cone, where the half-angle of the cone vertex is approximated to be 45 degrees [32]. Since none of the projections provide any information about the image inside this cone, it is referred to as the missing cone. Figure 2.9 illustrates how the missing cone's shape is formed in the frequency space.

As clearly evident, there are gaps within the frequency space. Discussed in the next section in more detail, these gaps in the frequency space are the reason why
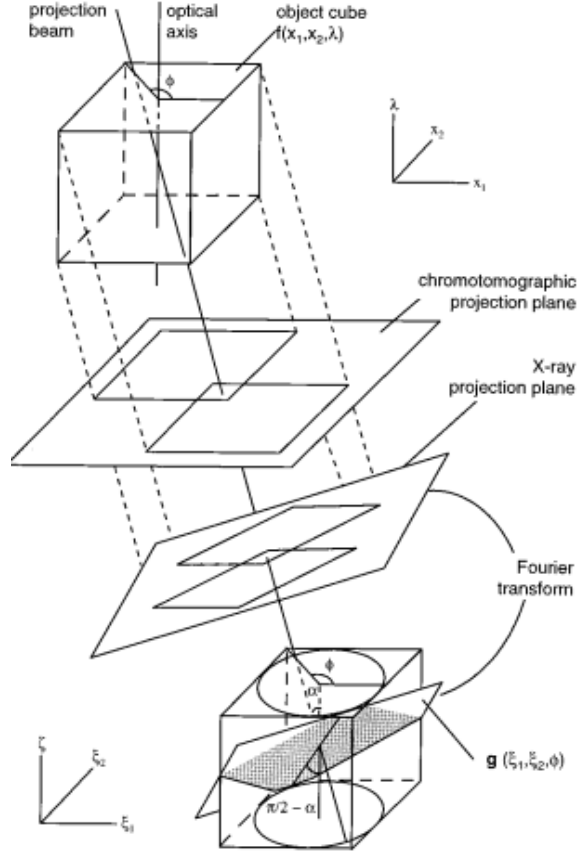
Figure 2.8. Geometry of chromotomographic data collection and its relation to the x-ray transform. [6]

a direct inversion method for producing a hypercube is ill-posed. Some mechanical techniques of filling in the missing cone described in [32] exist; however, some reconstruction algorithms is devised to fill in the missing cone. It is worth noting that a monochromatic source would fill in all the frequency space information as a monochromatic object is essentially a two-dimensional object, reverting back to the 2D central slice theorem.

2.5.3 System Transfer Function.

The System Transfer Function (STF) is shared among all the reconstructions in literature. The STF is a matrix that contains the location of all the spectral point
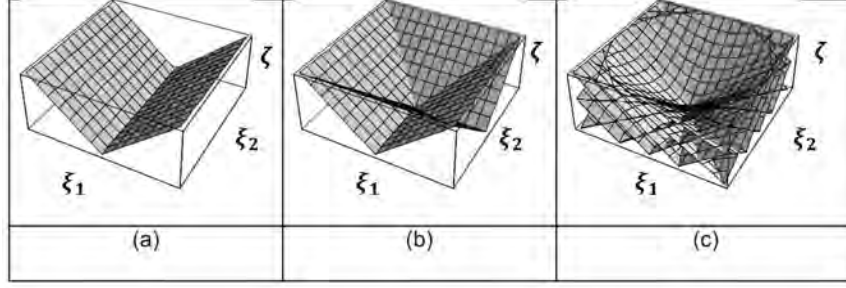
Figure 2.9. 2D Fourier transform of each projection equals a plane through the 3D frequency-space(ξ_1, ξ_2, ζ) representation of the object cube. The missing cone is the result of *limited-angle* problem and the inability to fill in all of the frequency space. As the number of projections increases, as shown in (a)-(c), the shape of the missing cone becomes more prominent. [14]

spread functions created from the prism.

Mooney showed in [31] that the measured projected data, $g(x_1, x_2, \phi)$, is found by summing each tomographic projection of the desired hypercube, $f(x_1, x_2, \lambda)$ with respect to λ

$$g(x_1, x_2, \phi) = \int_{-\infty}^{\infty} f(x_1, x_2, \lambda) * \delta(x_1 - k(\lambda)\cos(\phi), x_2 - k(\lambda)\sin(\phi))\mathrm{d}\lambda, \qquad (2.12)$$

where x_1 and x_2 are the pixel coordinates of the measured data cube and hypercube, ϕ is the projection angle bound between 0 and 2π, and $k(\lambda)$ is the spectrometer constant defined in Equation (2.11). Similar to the imaging convolution integral in Equation (2.1), the imaged formed is the result of shifts from prism onto the object. These shifts are summed for all wavelengths yielding the measured data cube. Equation (2.12) can be expressed more succinctly as

$$g(\bar{x}, \phi) = \int_{-\infty}^{\infty} f(\bar{x} - k(\lambda)\bar{p}_\phi, \lambda)\mathrm{d}\lambda, \qquad (2.13)$$

where $\bar{x} = (x_1, x_2)$, and $\bar{p}_\phi = (\cos(\phi), \sin(\phi))$. Taking the 2D Fourier transform of

24

Equation (2.13) becomes

$$G(\bar{\xi}, \phi) = \int_{-\infty}^{\infty} \exp[-2\pi k(\lambda)\bar{\xi} \cdot \bar{p}_\phi]F(\bar{\xi}, \lambda)\mathrm{d}\lambda, \tag{2.14}$$

where $\bar{\xi}$ is the spatial frequency representation of $\bar{x}$, and $\bar{\xi} \cdot \bar{p}_\phi$ denotes the vector dot product. Considering that the data cubes are sampled at a discrete spectral band, n, and discrete projection, m, Equation (2.14) is now a summation

$$G_m(\bar{\xi}) = \sum_{n=0}^{N-1} \exp[-2\pi n\bar{\xi} \cdot \bar{p}_m]F_n(\bar{\xi}, \lambda)\mathrm{d}\lambda, \tag{2.15}$$

where $\bar{p}_m = (\cos(2\pi m/M), \sin(2\pi m/M))$ for M projections measured, $0 \le m \le M$, and $n = k(\lambda)$ for N spectral bands of the device.

In terms of linear algebra, the spatial frequency representations of the projection images and object cube are related by

$$G(\bar{\xi}) = A(\bar{\xi})F(\bar{\xi}), \tag{2.16}$$

where $A(\bar{\xi})$ is a $M \times N$ matrix known as the STF. For each spatial frequency, the elements of $A(\bar{\xi})$ are

$$A_{m,n}(\bar{\xi}) = \exp[-2\pi n\bar{\xi} \cdot \bar{p}_m]. \tag{2.17}$$

The image cube is obtained by inverting $A(\bar{\xi})$,

$$F(\bar{\xi}) = A(\bar{\xi})^{-1}G(\bar{\xi}). \tag{2.18}$$

In order to invert the matrix, $M \ge N$; however, $A(\bar{\xi})$ is often rectangular and does not have full rank. Singular Value Decomposition (SVD) is used to find the pseudo-inverse and the minimum-norm solution is obtained. Since there are gaps within the

frequency space, advanced reconstruction algorithms must fill in the cone of missing information to achieve more accurate results.

2.6 Reconstruction Development

An alternative approach in finding the minimum-norm solution is to use a filtered backprojection (FBP) technique modeled from the medical tomography field [2]. Filtered backprojections essentially "shift-and-add" the collected projection images. For each projection angle, m, of the spectral bin, n, the projected image is shifted by the conjugate of Equation (2.17). This centers the projected imaged for the given spectral bin. For all M projections, the shifted projection images are summed resulting in a "stack" of shifted projected images. As the shifted projected images are summed, the information within the spectral bin increases its structural integrity and overcome the residual artifacts from the other spectral bin content. Filtering mechanisms are applied at either each successive shift or after summing the shifted images to reduce the residual artifacts. The filtered backprojection algorithm needs one iteration and is computationally efficient as Fourier transforms and matrix multiplications are required.

To fill in the missing cone, an iterative process such as Projection Onto Convex Sets (POCS) or maximum likelihood algorithms is required. The iterative reconstruction algorithms achieve recovery of the unknown object by utilizing *a priori* information about the image. Typically, an initial estimate about the unknown object is made, which is then subjected to a sequence of corrections, forcing it to satisfy a number of desirable characteristics. This sequence of corrections is applied repetitively until convergence occurs. Mooney *et al.* developed algorithms that used SVD to calculate the minimum-norm solution and feed it into a iterative POCS [6, 7] algorithm. Gould developed an reconstruction algorithm using Estimation Theory that

uses the STF to produce the maximum likelihood estimate of the object [16]. Both of these algorithms demonstrated the ability to reconstruct the scene accurately.

A computationally efficient reconstruction algorithm is desirable for AFIT. The space-based CTI has embedded processing and runs the risk of overheating [27]. Lowering the computational demands of the algorithm reduces the risk of overheating. In that spirit, a computationally efficient filtered backprojection algorithm developed by Deming in [10] is implemented for this thesis.

2.6.1 Fast Reconstruction Algorithm.

The fast reconstruction algorithm is a filtered backprojection which obtains the minimum-norm solution using closed-form expressions. The algorithm avoids calculating the pseudo-inverse by using a series of matrix multiplications, Fast Fourier Transforms (FFTs), and applying a spectral filter. Fewer computations are needed in calculating the FFT verse computing the pseudo-inverse. The amount of processing required is compounded when dealing with large focal plane array formats and collecting a large number of projections.

The reconstruction algorithm can be summarized as follows. For each spatial frequency, the preliminary (unfiltered) Fourier domain representation of the image cube (referred to as the Fourier cube), $F'(\bar{\xi}, \lambda)$, is computed by first backprojecting the data, $G(\bar{\xi}, \phi)$ with the Hermitian adjoint of $A(\bar{\xi})$

$$F'(\bar{\xi}, \lambda) = [A^H G](\bar{\xi}, \lambda) = \int_0^{2\pi} \exp[2\pi i k(\lambda)\bar{\xi} \cdot \bar{p}_\phi] G(\bar{\xi}, \phi) \mathrm{d}\phi. \qquad (2.19)$$

The filtered Fourier cube, $\tilde{F}_\mu(\bar{\xi}, \omega_\lambda)$, is found by 1D Fourier transforming the unfiltered Fourier cube from Equation (2.19) relative to λ to compute $\tilde{F}'(\bar{\xi}, \omega_\lambda)$ and

then applying the spectral filter

$$\tilde{F}_\mu(\bar{\xi}, \omega_\lambda) = \frac{\tilde{F}'(\bar{\xi}, \omega_\lambda)}{\mu + \tilde{M}(\bar{\xi}, \omega_\lambda)}. \tag{2.20}$$

The filtering parameter, μ, and the spectral filter, $\tilde{M}(\bar{\xi}, \omega_\lambda)$, are derived from filtering methods in the medical CT FBPs. $\tilde{M}(\bar{\xi}, \omega_\lambda)$ is a zero-order Bessel function that has been 1D Fourier transformed with respect to λ, simplified to

$$\tilde{M}(\bar{\xi}, \omega_\lambda) = 2(k^2 \xi_r^2 - \omega_\lambda^2)^{-1/2} \tag{2.21}$$

where $\xi_r = (\xi_1^2 + \xi_2^2)^{1/2}$ and k is the spectrometer constant defined in Equation (2.11). The final step is inverse Fourier transforming with respect to ω_λ to obtain the filtered Fourier cube. The value of μ depends on the noise level in the data, ideally μ will approach 0 but remain large enough to ensure stability in the presence of noise.

2.7 Spatial and Spectral Resolution Limits

The limits of the spatial and spectral resolution is based upon the most simplistic of objects, a point-source. In [5], Bostick built mathematical models and collected experimental data using point-sources to determine the spatial and spectral resolution. Bostick concluded that the spatial resolution is defined by full-width half-maximum (FWHM) of the point spread function as asserted by the Rayleigh Criterion. If the optical system is aberration free, the spatial resolution will be diffraction limited. The spatial features should not be impacted as the result of the prism dispersion, this is evident when considering a monochromatic object. The spatial features of a monochromatic object are preserved as there is no other spectral information is multiplexed with it. In the presence of aberrations, the size of the PSF will blur thereby limiting the ability to resolve.

28

Bostick determined that the limit of the spectral resolution is dependent on the prism dispersion and the FWHM of the spectral PSF. Under the assumption the reconstruction algorithm works ideally, if two objects which require a minimum spatial separation of w to be resolved, the minimum spectral separation $\triangle\lambda_m$ given by

$$\triangle\lambda_m = \frac{w}{f_3 \frac{\mathrm{d}\gamma(\lambda)}{\mathrm{d}\lambda}}.$$

(2.22)

In other words, the change in radial shift from one wavelength to another must be greater than the FWHM of the spot size for the wavelengths of interest. Consider a polychromatic point source in a diffraction-limited CTI system and ignoring performance and operation of the FPA. In order to resolve the spectral contents, the radial shift from the prism must be greater than the radius of the Airy disk given by Equation (2.8). If aberrations are present, the size of the Airy disk increases thereby lowering the spectral resolution.

2.8   Ground-based CTEx

AFIT has developed several iterations of laboratory and field instruments, collectively referred to as GCTEx, over the past several years. With each revision, the devices performance and capabilities have incrementally increased. The first lab tests where conducted by LeMaster [28] followed by Bostick [5]. O'Dell [36] created a Newtonian based instrument and collected the first set of field data. This system was challenging to align and did not maintain calibration which made deployment into the field difficult. Niederhauser [35] revamped the GCTEx into a linear system where all the components are centered along the optical axis, resulting in better performance and more robust field deployment.

2.8.1 Optical System.

The linear system developed by Niederhauser [35] follows the layout of Figure 2.6. It utilizes three telephoto lenses to mitigate aberrations, specified in Table 2.4, and the spinning DVP is housed in a solid block of aluminum to reduce vibrations from the motor. The linear system is machined such that no adjustments are necessary and is quick to assemble.

Table 2.4. GCTEx Lens Specifications.

Lens	Model	Focal Length (mm)	F/#	Mount Type
L_1	AF-S Nikkor 400m f/2.8G ED VR	400	2.8	F
L_2	Tamron 1A1HB 75mm	75	3.9	C
L_3	AF Nikkor 85mm f/1.8D	85	1.8	F

The linear system is shown in Figure 2.10. The system uses a high-speed video camera, Phantom v5.1, from Vision Research which collects images at rates up to 10 kHz.
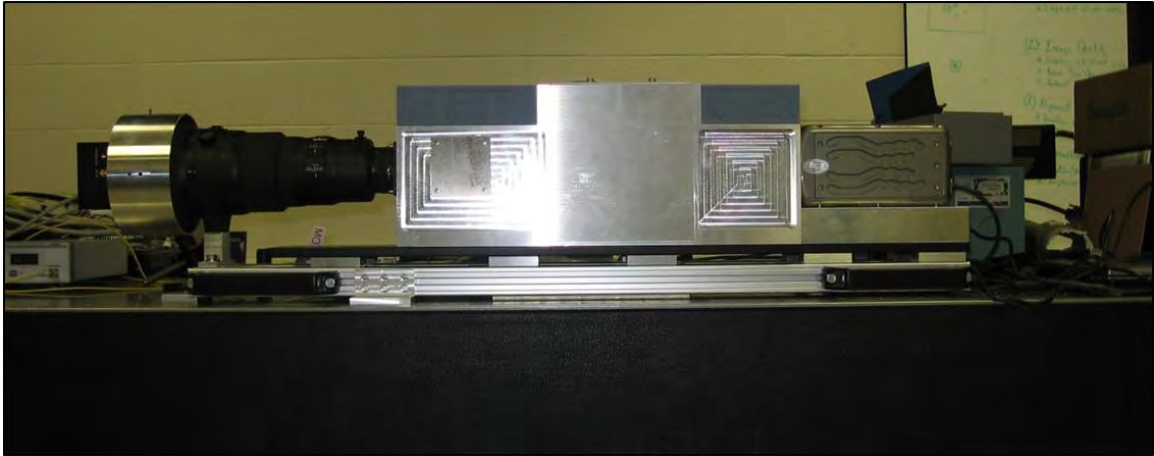
Figure 2.10. Linear GCTEx instrument developed by Niederhauser. [35]

The DVP is housed in a circular shaft that spins at rate up to 25 rev/s. For each

revolution, a complete hypercube produced, therefore the GCTEx produces up to 25 hypercubes per second. For the space-based system, the prism will rotate nominally at 100 rev/s. The DVP was designed by Bostick and is made of an optically-bonded assembly of Schott LaSF N30 and SFL6 glass 8 components as shown in Figure 2.11.
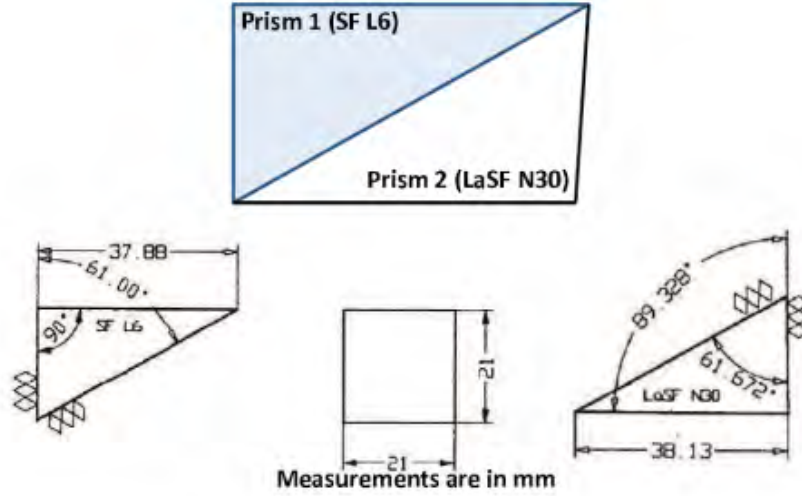
Figure 2.11. Geometry and components of the Direct Vision Prism. [36]

The dispersion of the prism could be solved using Snell's law; however, it has been more convenient to express the deviation angle caused by the prism in the form of the power model,

$$\gamma = a\lambda^b + c. \tag{2.23}$$

The DVP curve fit parameters: a, b, c for the deviation angle (degrees), γ, for a given wavelength (μm) are listed in Table 2.5. The data used for the power model is based off of calculations from Zemax model of the DVP. The undeviated wavelength, $\gamma = 0$, of the prism is at ≈ 547 nm.

The linear system demonstrated that the optical performance increased from the Newtonian design. The polychromatic MTFs measured where significantly higher and most importantly, the measured deviation angles matched the theoretical values

31

Table 2.5. Theoretical DVP Curve-fit Parameters from by Zemax model.

Term	Value
a	.2182
b	-3.329
c	-1.633

predicted by Zemax. In Figure 2.12, three emission lines from a mercury pen lamp match the Zemax model.
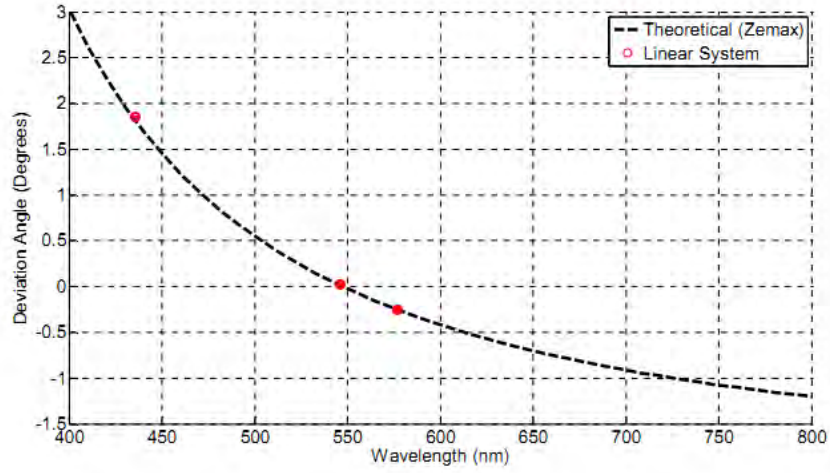
Figure 2.12. Mercury pen lamp emission lines matching the Zemax model. [35]

The match in deviation is crucial for reconstruction; however, tests of the linear system concluded that a transverse offset which laterally shifts the deviation angle from its predicted center was present. Additionally, since the GCTEx uses telephoto lenses where multiple groups of lenses are used to reduce monochromatic aberrations, the system has a significant amount of chromatic aberrations. Both of chromatic aberrations and transverse offset are discussed in the next sections.

2.8.1.1 Chromatic Aberrations.

To demonstrate chromatic aberrations, mercury (Hg) and neon (Ne) pen lamps are used in the laboratory. Mercury and neon pen lamps are used to calibration sources because of of their distinct spectral lines features. Table 2.6 lists the spectral lines and the corresponding relative normalized intensity [34, 38] for each source used throughout this thesis.

Table 2.6. Normalized Relative Intensity Emission Lines of Hg and Ne Pen Lamps.

Hg Lines μm	Ne Lines μm	Normalized Relative Intensity
0.40465		0.44
0.43583		1.00
0.54683		1.00
0.57696		0.11
0.57907		0.12
	0.5853	0.2000
	0.5882	0.1000
	0.5945	0.0500
	0.6096	0.0300
	0.6153	0.1000
	0.6217	0.1000
	0.6267	0.1000
	0.6334	0.1000
	0.6402	0.2000
	0.6506	0.1500
	0.6601	0.0100
	0.6678	0.0500
	0.6717	0.0070
	0.6923	1.0000
	0.7028	0.3400
	0.7245	0.7700
	0.7489	0.3200

A point source was simulated by placing and iris in front of the mercury and neon pen lamps. The results taken using GCTEx are shown in Figures 2.13(a) and Figure 2.13(b).
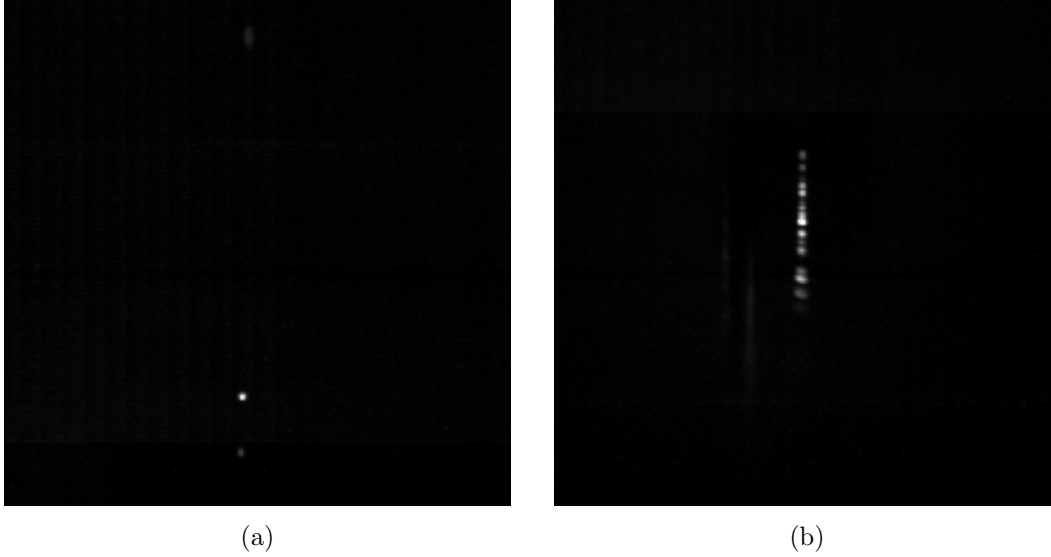
Figure 2.13. (a) Chromatic blurring of the 435.8 nm line, near the top of the image, from a Hg pen lamp. (b) The shorter wavelengths, closest to the top of the image, of the Ne pen lamp are in focus while the longer wavelengths are blurred.

From the mercury pen lamp, the FWHM of the 546.8 nm line is 2.30 pixels while the 435.8 nm line has a FWHM of 7.37 pixels.

2.8.1.2   Transverse Offset.

The transverse offset, or pinwheel offset, presents a serious problem for the reconstruction algorithm. The fast reconstruction algorithm relies on the location of the spectral PSFs. Not accounting for the offset results in an error in the location and thus a significant performance drop in reconstructing the scene. Figure 2.14 shows measured center is offset from the predicted center of the circular dispersion path. It is important to note that dispersion within the radial line remains consistent with the predicted dispersion values.

Niederhauser equated the offset as a jump discontinuity and averaged the radii to obtain a correction in the power model fit parameters. However, it is important to realize the lateral shift is constant for all wavelengths and is symmetric for all
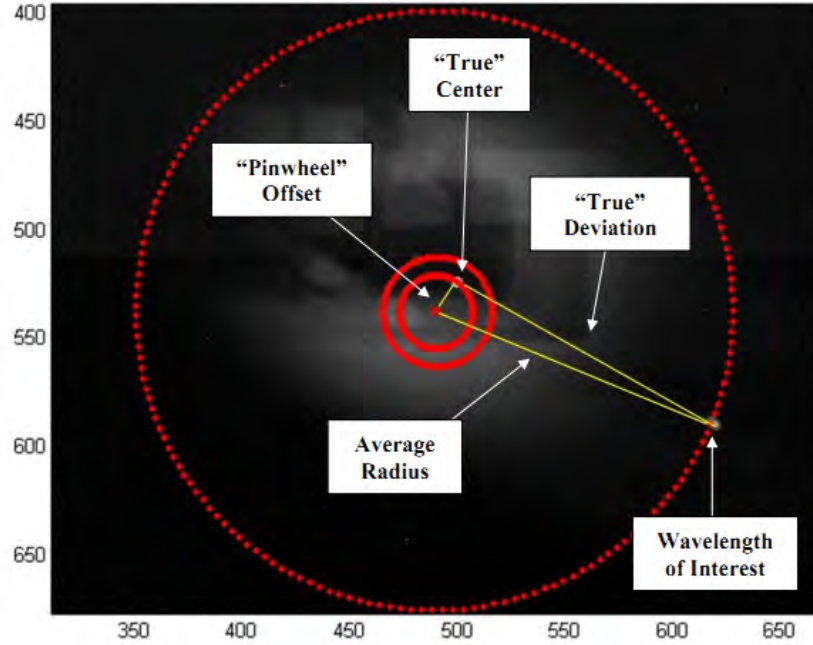
Figure 2.14. Demonstration of the transverse offset from a mercury pen lamp point source. The dispersion along the "true" deviation line matches the predicted model; however, the transverse, or "pinwheel", offset shifts the center of the deviation from the predicted center. [35]

rotations. Figure 2.15 displays a mercury pen lamp point source at projection angles in 90 degree increments. For each projection angle, the 435.8 nm, 546.8 nm, and 576.9 nm emission lines are shown with the 435.8nm line being the outermost.

For the 546.8 nm line, a blue circle is added to illustrate that offset is radially symmetric over the projections. Also note there is a phase lag for each projection. Ideally, all of the projections for the 546.8 nm line would align perfectly with dashed green line which is the center of the radial offset. The phase lags for shorter wavelengths under the undeviated wavelength and leads for the longer wavelengths. This phase lag changes with wavelength and must also be accounted for in the reconstruction algorithm.
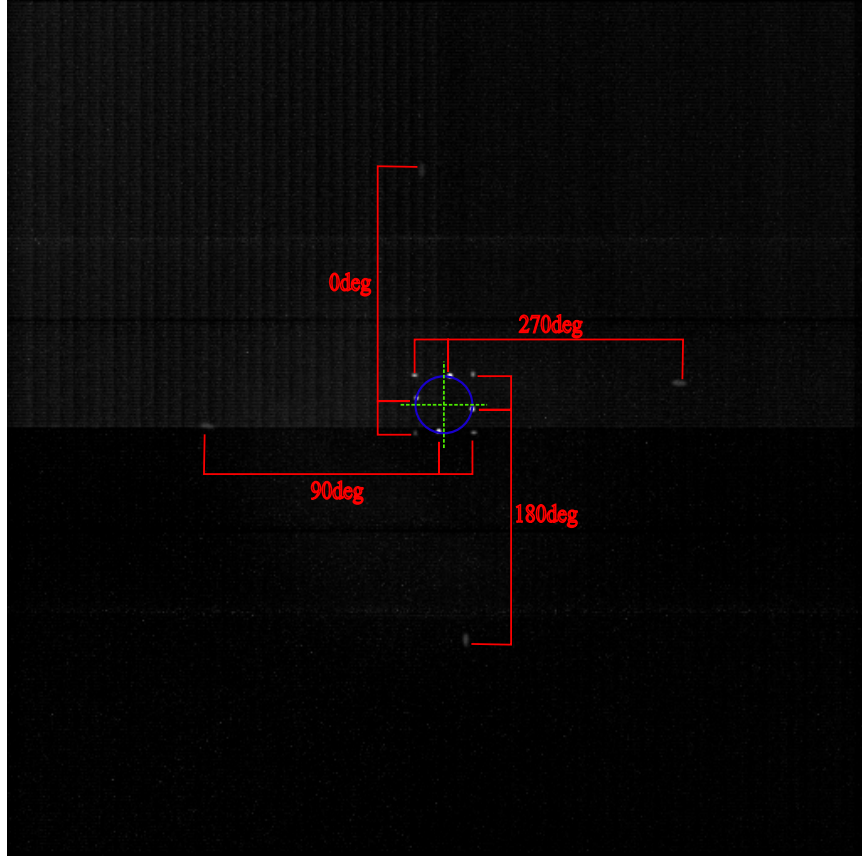
Figure 2.15. Four orthogonal projections measured using a mercury pen lamp point source.

2.8.2 Phantom Camera.

GCTEx uses the Vision Research Phantom v5.1 monochrome CMOS sensor. The camera is capable of collecting data at fast frame rates, up to 95 kHz at the smallest resolution of 64x32 pixels. However, the dispersion of the prism and a 85 mm focusing lens require that 512x512 resolution be used, yielding a maximum frame rate of 4380 frames per second. If larger formats are required, the maximum rate will drop accordingly. Table 2.7 summarizes the list of camera specifications. The pixels of the camera are assumed to be square.

The camera is able to frame quickly by storing the collected data to internal memory. The camera will continuously run until a trigger is received by the user.

36

Table 2.7. Phanton v5.1 Camera Spefications.

Parameter	Value
Detector	Silicon
Full Resolution (pixels)	1024x1024
Frame Rate at Full Resolution (Hz)	1200
Minimum Exposure Time (μs)	2
Pixel Pitch (μm)	20
Bit Depth (bits)	8
On-board Memory(MBytes)	4096

The frames are placed in a circular buffer, so the oldest frame is overwritten once the memory is full. The camera's system gain, noise performance, and quantum efficiency (QE) are necessary for estimating the amount of signal necessary to detect a target. The manufacturer provides documentation on the camera parameters; however, the documentation is limited and not sufficient. A photon transfer curve, as described in [25], was generated to determine system gain and noise performance. A monochromator and calibrated photodiode setup were used to calculate quantum efficiency. The results from the photon transfer curve are listed in Table 2.8.

Table 2.8. System gain, K_{ADC}, and read noise of the Phantom Camera.

Parameter	Value	Uncertainty
K_{ADC} (e$^-$/DN)	143.12	$\pm$ 7.73
Read noise (e$^-$)	34.87	$\pm$ 7.92

The camera's performance is poor, the sensitivity, K_{ADC}, of the camera is low and the amount of photo-electrons are required to rise above read noise floor is high. Furthermore, the camera has considerable amounts of fixed-pattern noise (FPN), the pixel-to-pixel gain non-uniformity, which had to be subtracted to obtain these results. Additionally, the camera exhibited a nonlinearity in the system gain. This nonlinearity prevents a flat-field correction to be applied over the entire dynamic range. The poor performance and the nonlinearity are thought to be attributed to

the high speed nature of the device. These results are reported but ignored and assumed to be ideal for the purposes of creating a simulation and evaluating the reconstruction algorithm.

The QE of the camera was calculated from the wavelength from 400 nm to 740 nm in increments of 20 nm. The QE measurements were taken at lower frame rate in order to increase the integration time to achieve a higher signal. The results are shown in Figure 2.16 below.
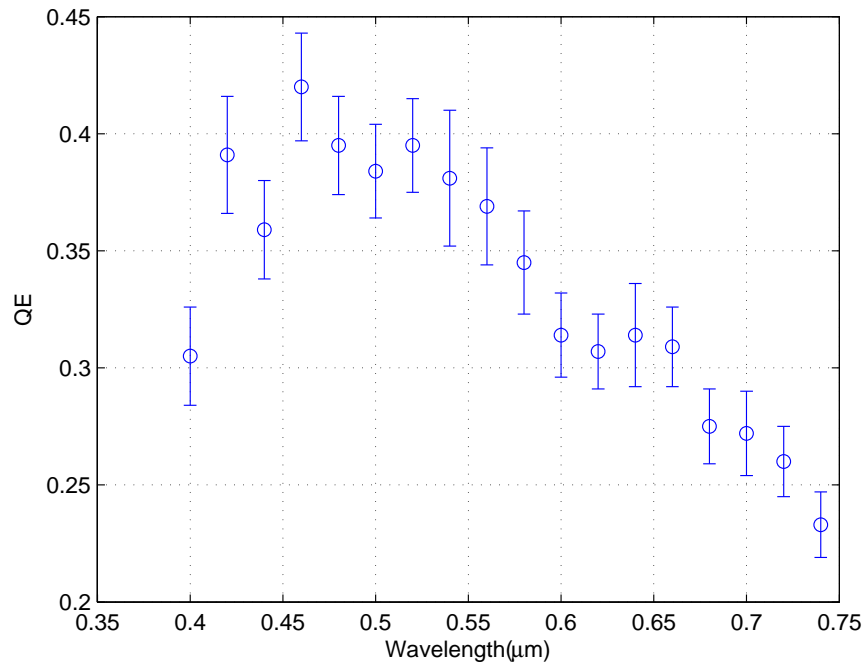
Figure 2.16. Quantum efficiency over the visible regime. The oscillations are consistent with those observed by O'Dell and the camera manufacturer's datasheet.

The camera's QE has a peak response at 460 nm of 0.42 and remains above 0.20 over the entire wavelength range. As expected, the shorter wavelengths have lower QE due to reflections. At the longer wavelengths, QE drops off because it is more difficult to generate photo-electrons as the energies approach the required band gap energy. The QE measurements published by the camera vendor advertise QE's above

0.50 from 450 nm to 650 nm; however, these measurements published were for a newer model [41]. The QE oscillates over the spectral range and the oscillation is more pronounced if smaller increments are used and is averaged out with 20 nm increments. The shape of the QE curve matches the relative measurements made by O'Dell [36] and are consistent with datasheets from the manufacturer.

2.8.3 Electrical Support System.

Fixing the electronics system was one of the main research goals in this thesis. Knowledge of the prism angle is imperative for the reconstruction algorithm. Previous AFIT had to manually calculate prism angles based off of poorly synchronized timestamps and made it difficult for reconstructing scenes. Thus, the entire electronics and software system were redeveloped in order to fix the logging of the prism angles in relation to the camera files.

The GCTEx Electrical System controls the speed of the prism, operation of the Phantom v5.1 camera, and collects the encoder data associated with the prism's angle. A rackmount computer houses the SAM-3 data acquisition module and controls the camera. The motor control and a custom electronics board that converts the encoder signals into prism angles are housed in a custom enclosure. Finally, a network switch connects the camera, computer, and any other peripheral using the local network. All of the electrical equipment is bundled into a small 8U portable rack for ease of transportation as shown in Figure 2.17. See Appendix B for the electrical system block diagram.

The prism angle is measured by a quadrature encoder and has a resolution of 4096 bits per revolution. This means that the angular resolution of the prism angle is within 0.088 degrees or 1.534 milliradians. The prism angle is sampled by the SAM-3 module and is synchronized with the captured images using timing signals provided

Figure 2.17. Portable CTEx rack for easy transportation to field.

by the camera. The timing signals allow the prism angle to be captured at the start and end of the camera's integration time. This architecture avoids interpolating the prism angles using timestamps from the SAM-3 and camera, which posed a significant problems for previous AFIT students.

The electronics are capable of sampling the encoder data at 1 MHz, which correlates to the maximum speed of 244 rev/sec before the prism has traveled a distance more than the encoder resolution. This maximum speed is well above the notional operating speed of 100 rev/sec.

3. System Model Methodology and Validation

The need for a high fidelity simulation of the optical system is imperative for future development of AFIT's chromotomography experiment (CTEx) project as the system has yet to be fully characterized and understood. Furthermore, a high fidelity simulation provides an invaluable tool for developing the reconstruction algorithm and determining design criteria for the spaced-based system, referred to as SCTEx.

CTEx's optical system has been modeled in Zemax over the past several years. Zemax is an industry standard for computer-aided optical system design and is a well-vetted optical system analysis tool. Zemax is a physics-based model that uses geometric ray traces and wave propagation to obtain more realistic simulations. Zemax's capabilities will be heavily leveraged upon to build the simulation. The simulation model uses MATLAB to serve as an interface to Zemax using the Dynamic Data Exchange (DDE) interface tools created by Griffith[17]. The design goals for the simulation are:

- Provide a mechanism to simulate a variety of scenarios
- Move away from paraxial approximations and develop more representative models that demonstrate the effects of aberrations
- Decouple the simulation from the model, i.e. the simulation will work with any Zemax model

3.1 Assumptions

Several assumptions are made to reduce complexity while maintaining the integrity of the simulation:

1. Transmission loss due to atmospheric absorption is negligible operating in the VIS/NIR

2. No loss of image quality or transmission due to atmospheric effects

3. All sources are incoherent

3.2   Overview of Simulation

The foundation of the chromotomographic simulation lies within the Zemax model for the optical system. In order for the simulation to be accurate, requires that the Zemax model be accurate as well. Once the Zemax model is developed, the simulation can be executed. The simulation is setup by MATLAB so interchanging Zemax models requires minimal effort. This capability allows different Zemax models to be quickly evaluated.

The DDE interface allows MATLAB to control Zemax functions autonomously. Almost all Zemax functions are available through the DDE interface, if they are not available, functions can be created using Zemax's scripting language. MATLAB is able to rotate the prism, vary wavelengths, and perform image analyses. Figure 3.1 is a flowchart of the simulation using all the DDE function calls.

The simulation defines the object, both spatially and spectrally, as a function of prism angle. Time is controlled by varying the prism speed, and the angular displacement of the prism angles varies with according to prism speed. For each simulation, the user defines the spatial and wavelength profiles of interest.

Using the set spatial profile, MATLAB creates or defines an image source file to be simulated at each prism rotation. An image simulation is completed for all wavelengths listed in the wavelength profile. The results of the image simulation are then scaled according the the wavelength profile. After all wavelengths have been simulated and scaled, the results of all simulations are summed to produce the simulated output for each prism angle defined.
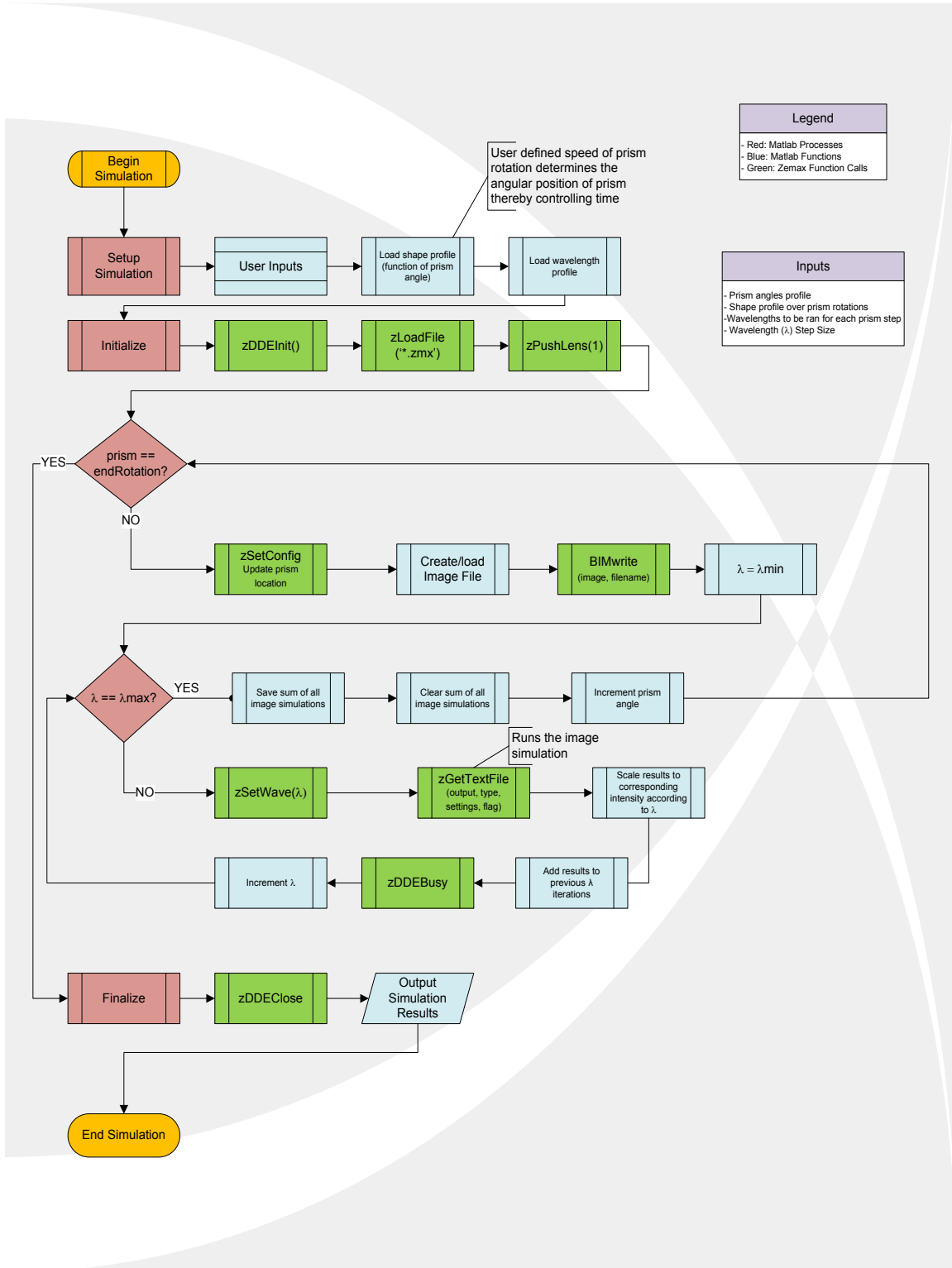
Figure 3.1. Flowchart of the chromotomographic simulation.

3.2.1 Zemax Image Simulation.

The Zemax image simulation is based upon Equation (2.2), where a grid of point spread functions are convolved with the image source file to form the simulated image through the optical system. The grid spans the field size and describes the aberrations at selected points in the field of view defined by the source image file and field size settings.

The Image Simulation tool performs the following operations to produce the simulated image:

1. The source image file is oversampled and a guard band is applied specified by the user

2. A grid of PSFs are computed

3. The PSF grid is interpolated for every pixel in the modified source image file

4. At each pixel, the effective PSF is convolved with the modified source image file to determine the aberrated bitmap image

5. The resulting image bitmap is then scaled and stretched to account for the detected image pixel size, geometric distortion, and lateral color aberrations

An example of the image simulation PSF grid and the resulting simulated image are shown in Figures 3.2(a) and 3.2(b), respectively.

The calculation of the PSF grid is critical for accurate results. There are two methods for modeling the aberrations using the PSF: diffraction and geometric. The diffraction method computes the PSF using direct integration of Huygens wavelets method[44]. The geometric method computes the PSF based upon an integration of the radial spot size that is calculated by a geometric ray trace. If the aberrations are twenty times the diffraction limit, the diffraction method will independently switch to the geometric method.

(a)	(b)
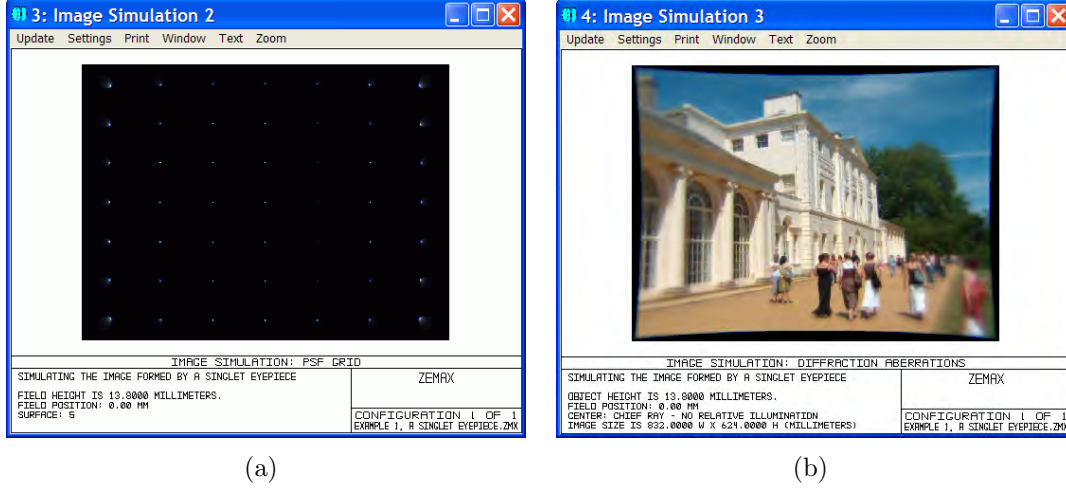
Figure 3.2. (a) A PSF grid displaying the effects of distortion. (b) The resulting image simulation by convolving an image source file with the PSF grid.

3.3 Zemax Models

Three models were developed in this thesis for all the scenarios simulated. A paraxial model, were an ideal lens refracts all rays (for all wavelengths) perfectly. A chromatic model, were multi-element telephoto lenses are modeled to demonstrate the effects of chromatic aberrations. A aberrated model, were a Zernike phase surface adds controlled amounts of aberrations. These models incorporate the same focal lengths and DVP described in Section 2.8.1.

3.3.1 The Paraxial Model.

The first Zemax model created uses paraxial, or ideal, lenses for the development and assessment of the reconstruction algorithm. Paraxial lenses behave ideally and all rays converge to a single point resulting in perfect optical system response. The model is shown in Figure 3.3.

This model matches the theoretical operation as described in literature, thereby any deficiencies in the reconstruction results are attributed to the algorithm.

L1

L2   DVP   L3
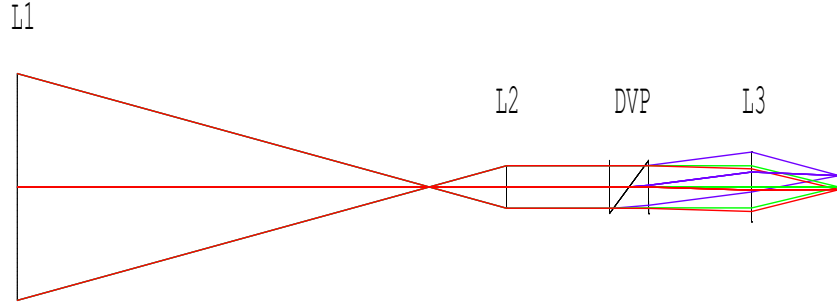
Figure 3.3. Zemax model using paraxial lenses.

3.3.2 Chromatic Model.

The chromatic model uses telephoto lenses modeled after prescriptions from patents[39, 40]. Due to the difficulty of canvassing through thousands of patents, these prescriptions are not an exact match of the GCTEx lenses. The number of lens elements differ and the F-numbers are larger; however the focal lengths are the same. The goal is to have something representative of GCTEx to demonstrate the effects of chromatic aberrations. Since the aperture sizes of the chromatic model lenses are smaller, the focal length of L_2 was increased to ensure that the theoretical Airy disk radius was the same as the paraxial model. A paraxial lens was used to ensure the change in longer focal lengths did not negatively impact the system performance. The increased focal length of L_2 lowers the angular magnification but is compensated by adjusting the field height of the source image file. Figure 3.4 displays the chromatic model.

This model demonstrates the impact of chromatic aberrations on the reconstruction algorithm and the wavelength dependent degradation of the optical system's spatial resolution.
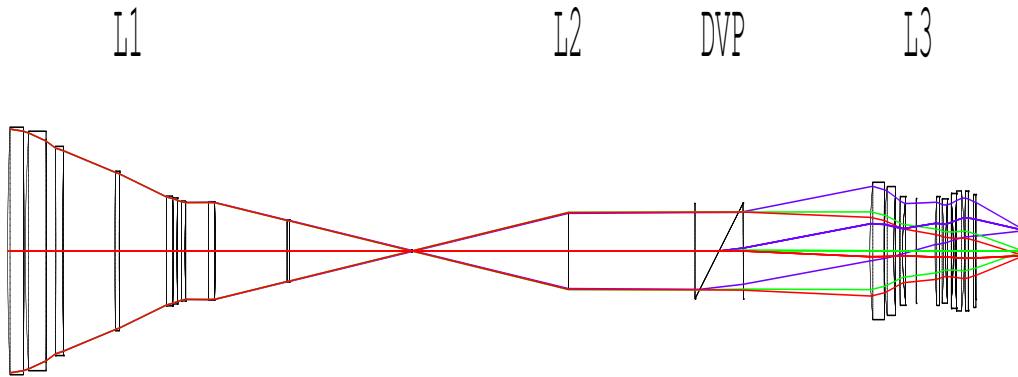
Figure 3.4. Zemax model using telephoto lenses.

3.3.3   Zernike Phase Surface Model.

The Zernike Phase Surface function in Zemax was designed to model optical systems as a black box so that optical designers can share the performance of the system without the giving the exact prescription. The surface can also be used to incorporate interferometric measurements of optical components and model them in Zemax.

The model uses a Zernike Phase Surface to control the amount of aberrations projected onto the image plane from the focusing lens. The Zernike Phase Surface modifies the incoming wavefront according to the 37 term Zernike FRINGE polynomials. However, only the first nine Zernike terms are used to represent the Siedel aberrations. The Zernike Phase Surface is placed directly after a paraxial lens which focuses the light onto the detector. The telescope portion of the GCTEx is also made of paraxial lenses so the model looks exactly like the paraxial model shown in Figure 3.3.

3.4   Validation of Model and Simulation

To validate the paraxial model and simulation, the radial shift given by Equation (2.11) needs to match the deviation angle measured by Niederhauser. A monochromatic point source, modeled as a perfect circle, centered in the field-of-view was simulated. The point source's wavelengths was varied from 400 nm to 750 nm in 25 nm increments. The deviation angle was calculated by simulating 50 evenly-spaced projections for each wavelength increment. Using a modified script from Niederhauser, the deviation angle is computed by calculating the centroid of each projection and finding a circular fit for all of the centroids as shown in Figure 3.5.
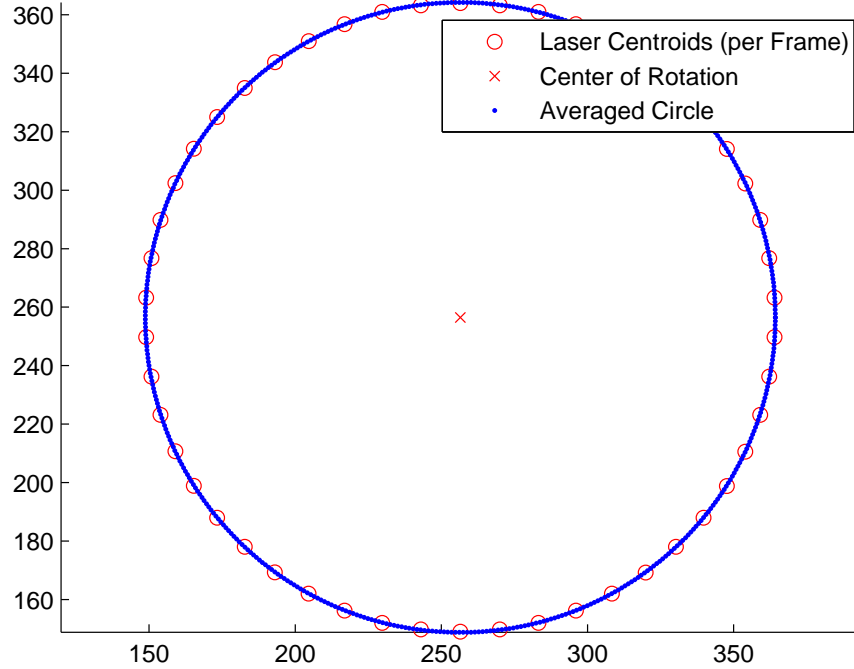
Figure 3.5. Radial shift of a 425 nm point source at multiple projections.

This method is representative of how the measured deviation angles were obtained by Niederhauser. The results of the validation are shown in Figure 3.6. As expected, the radial shift of the simulation matches the theoretical results.
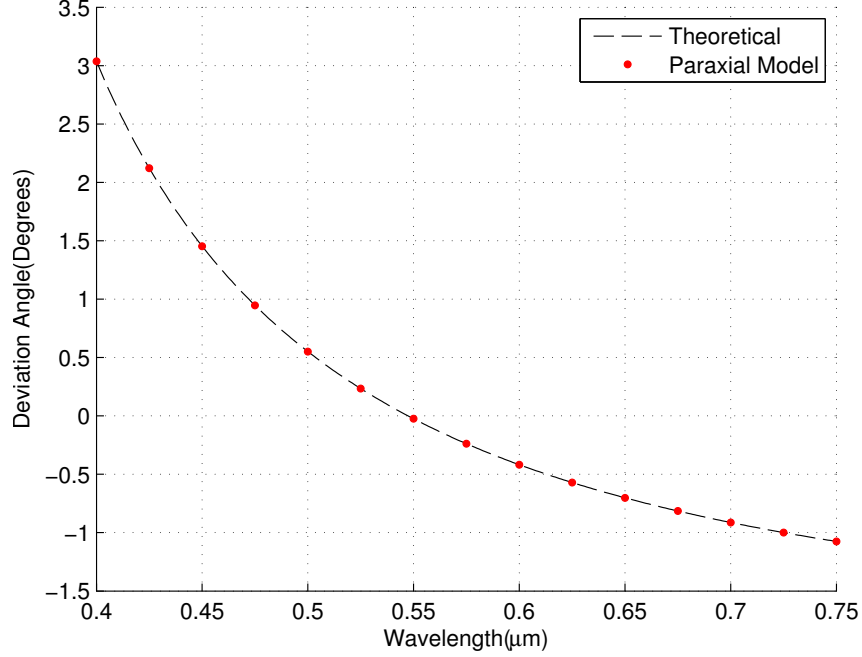
Figure 3.6. Measured deviation angle from a simulated point source at multiple wavelengths.

The chromatic model is validated by simulation of mercury and neon pen lamp point sources and comparing them to the measured lab experiments. The chromatic simulation uses the normalized relative intensities from Table 2.6 for each pen lamp. The model was focused to the undeviated wavelength of 547.5nm, near the center of the spectrum of interest. The size of the simulated spot size was adjusted to match that of the measured data. Figures 3.7(a) and 3.7(b) are the measured and simulated outputs for the mercury pen lamp.

Qualitatively, the model matches the measured data well. The positions of each emission line match with each other and the blurring on the 435.8 nm line is observed on both. The 404.6 nm line has a faint signal that is close to the noise floor, making it difficult to observe on the measured data set. The lower intensity of the line, the low QE response at that wavelength, detector noise, and the blurring of the spot are the primary causes why the line has a faint signal.

<div align="center">(a)   (b)</div>
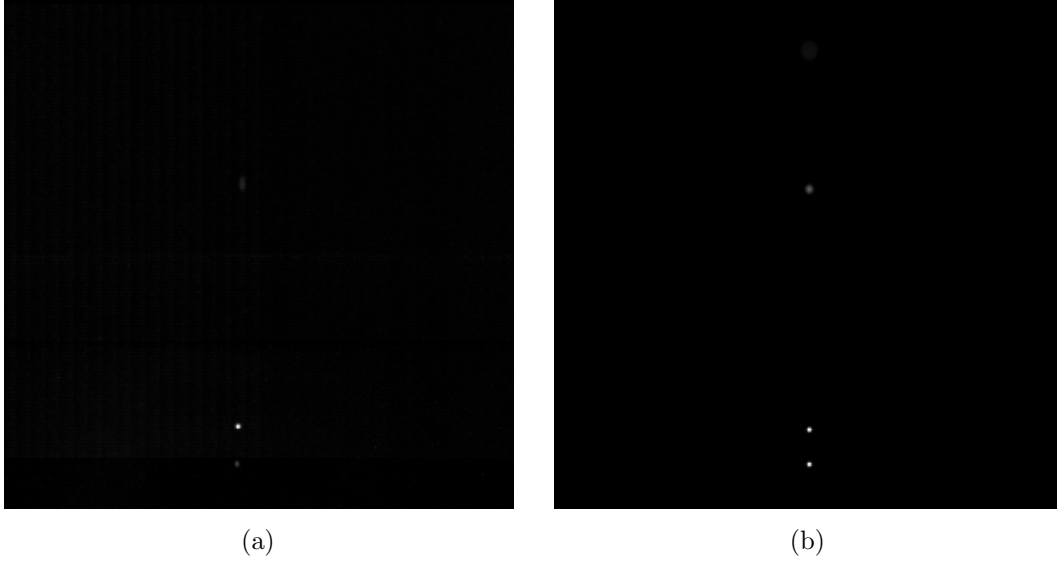
Figure 3.7. Measured and simulated, respectively, mercury pen lamp data. The longer wavelengths are near the bottom of the images.

Using the same configuration as the mercury pen lamp, the neon pen lamp was simulated for its respected wavelengths. Figures 3.8(a) and 3.8(b) are a comparison of the measured data verse the simulated.

The simulation also models the GCTEx chromatic aberrations well for the longer wavelengths. The blurring of the model is more pronounced at the longer wavelengths; however, considering the telephotos are not an exact match the results are acceptable.

The Zernike model is not validated experimentally but the model is able to add controlled amounts of aberrations as shown in Figures 3.9(a)- 3.9(d). With respect to 550nm, 10 waves are placed on each of the Zernike coefficients, Z_6 and Z_7, to demonstrate the effects of coma.

The simulation consists of four projections and wavelengths varying from 400-750 nm in 50 nm increments. The shorter wavelengths are the outermost and have more pronounced effects from the aberrations than those wavelengths in the center.

<center>(a)   (b)</center>

Figure 3.8. Measured and simulated, respectively, neon pen lamp data. The longer wavelengths are near the bottom of the images.

3.5 Source of Transverse Offset

Determining the source of the transverse offset is important so that it can be corrected or avoided in future designs. To find the root cause, tilt and centration errors for each surface were modeled. Additionally, the Zernike model was used to determine if any aberrations may be the cause. The main criteria for finding the root was looking for a tilt or offset that caused a shift in the undeviated wavelength when the prism is rotated.

No tilts, offsets, and aberrations on the lenses result in the undeviated wavelength to shift with prism rotation. This lead to investigating the prism and was quickly identified as the likely candidate. Hawks[21] identified the transverse offset is likely an alignment error from rotating, or "twisting", one of the glasses about the normal to the interface surface where the glasses meet. Figure 3.10 illustrates an exaggerated rotation of a simple top-down or bottom-up perspective of the prism, separated into the two glass components (red and blue).

The resulting "twist" causes the lateral shift and phase lag observed in Figure 2.15.

<center>51</center>
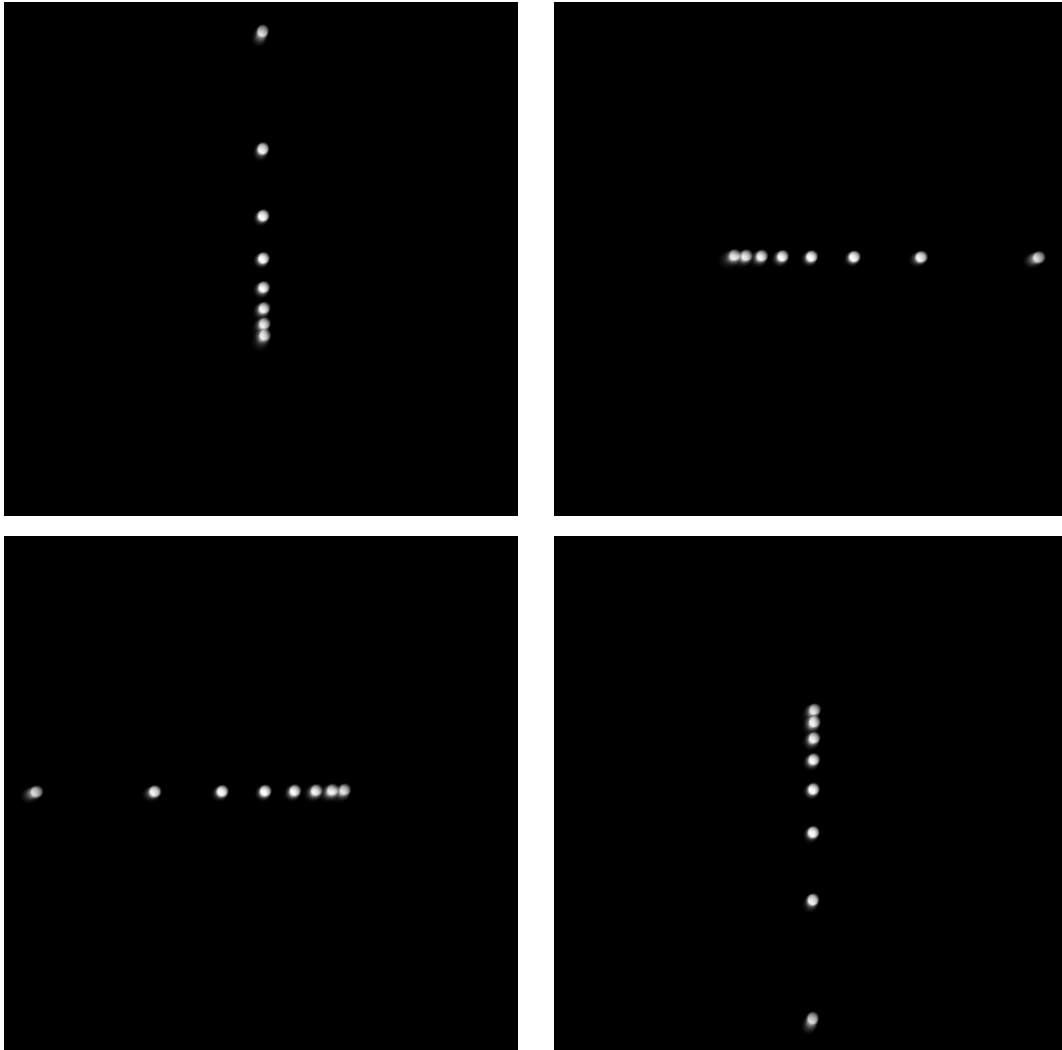
Figure 3.9. Four orthogonal projections created by the Zernike model displaying the effects of coma. A uniform spectral intensity point source sampled at 25 nm increments is shown for each projection. The "tail" of coma is more pronounced for the shorter wavelengths (closer to the edges of the figures).
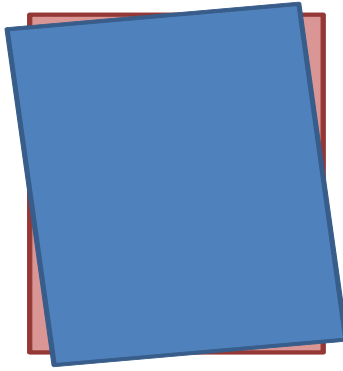
Figure 3.10. A top-down or bottom-up perspective of an exaggerated rotation about the normal to interface surface where the glasses (shown by the red and blue rectangles). This rotation is believed to be the source of the transverse offset.

Figure 3.11 is a Zemax generated footprint diagram of orthogonal projections using the mercury pen lamp emission lines. The 546.8 nm projections, designated by squares, share the same symmetric offset and the lag in phase with the measured data.

Figure 3.12 plots the transverse offset as a function of the amount of prism misalignment using the Zemax model. A 85 mm lens and a detector with a 20 μm pixel pitch were used produce the amount of error in pixels. The transverse error, is the lateral shift perpendicular to the dispersion path while the wavelength error is along with the path.

The results of this simulation are used to provide an estimate of how much the prism is misaligned. The next section covers how the transverse offset was measured.

3.5.1 Correcting for the Transverse Offset.

The first step towards correcting the transverse offset was to determine the amount of lateral shift. To do so, a elliptical-fit MATLAB script developed by Niederhauser that calculates the radius and eccentricity of elliptical shapes was used. From mea-
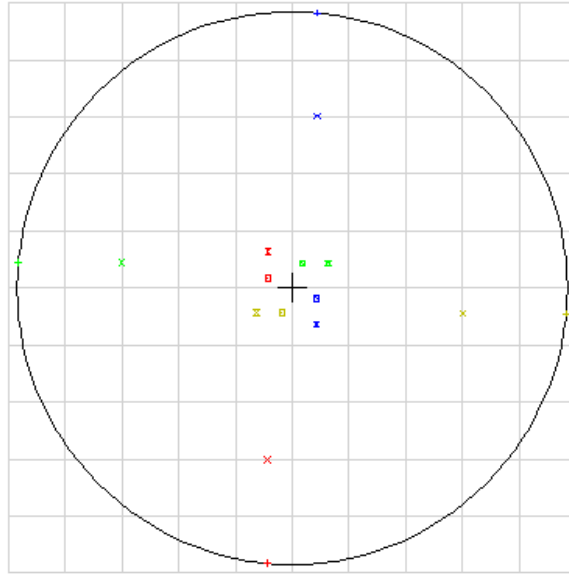
Figure 3.11. Footprint diagram showing a "twist" in the prism alignment. Four orthogonal projections of the mercury pen lamp wavelengths are shown. The 546.8 nm projections, designated by squares, have a symmetric offset and lag in phase like the measured data set in Figure 2.15.[21]
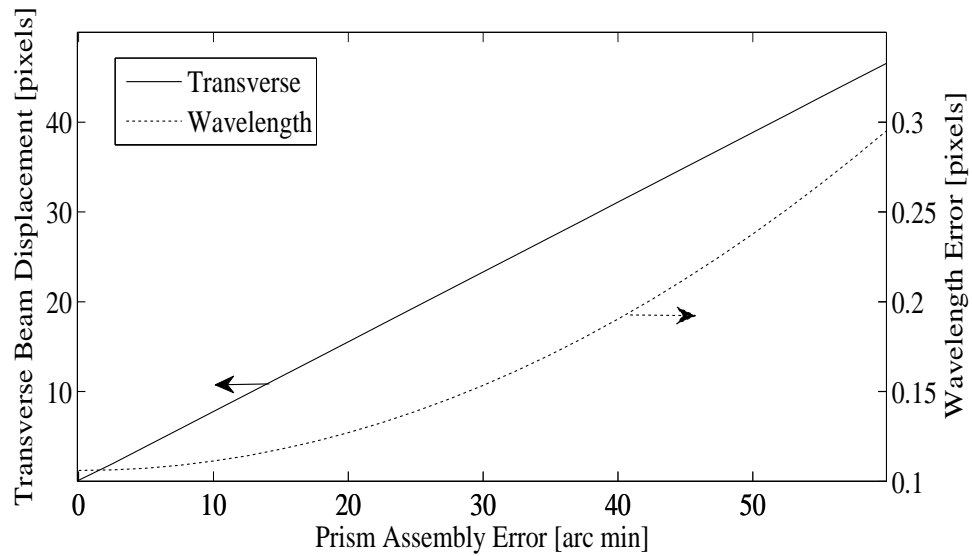
Figure 3.12. Transverse and wavelength errors for varying degrees of prism alignment error. Transverse error is the perpendicular shift from the dispersion path while the wavelength error is along the path.[21]

sured the same mercury pen lamp data used to observe the chromatic aberrations, the centroid of the 546.8 nm line from each projection was calculated and plotted as shown in Figure 3.13. These centroids are then input into the elliptical-fit script for calculation.
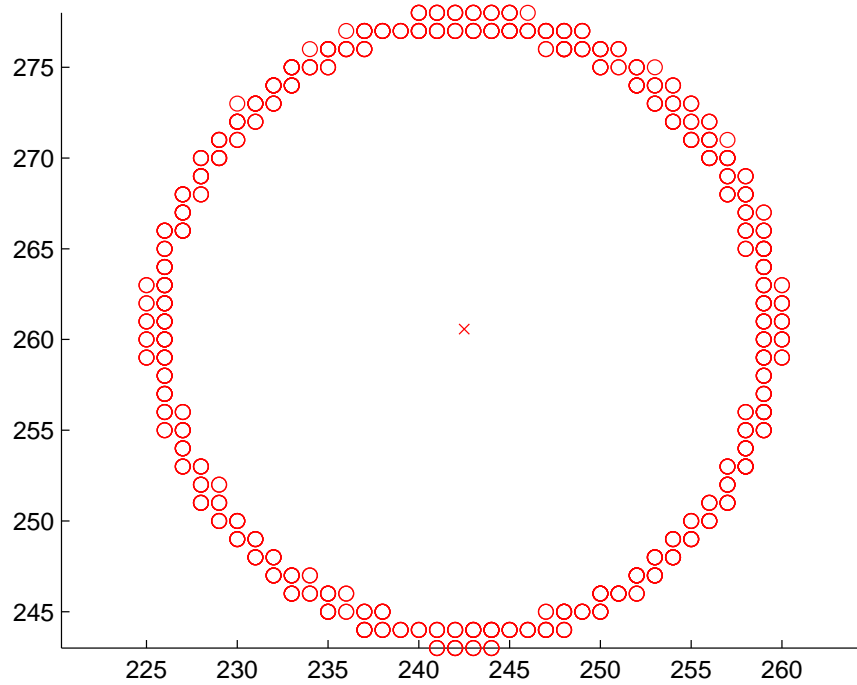
Figure 3.13. Centroids from each projection of the 546.8 nm line of a mercury pen lamp were used to determine the amount of lateral shift. The elliptical-fit script calculates the center, radius, and its eccentricity of the shape. The radius of the elliptical shape must be accounted for in the reconstruction.

The results from the elliptical-fit script computed the transverse offset as 16.9 ± 0.4 pixels and was nearly a perfect circle. From Figure 3.12, an alignment error of 20.5 arc minutes produces a transverse offset of 16 pixels. A 20.5 arc min error is reasonable if the "twist" tolerance was not specified during fabrication of the prism.

To correct for the offset, an additional shift must be applied to account for the transverse offset. Figure 3.14 depicts the two shifts necessary for reconstruction, the first shift is the uncorrected shift defined in Equation (2.17) which places the object

onto the circumference of the transverse offset and the second shift then moves the object into the center of the reconstructed image.
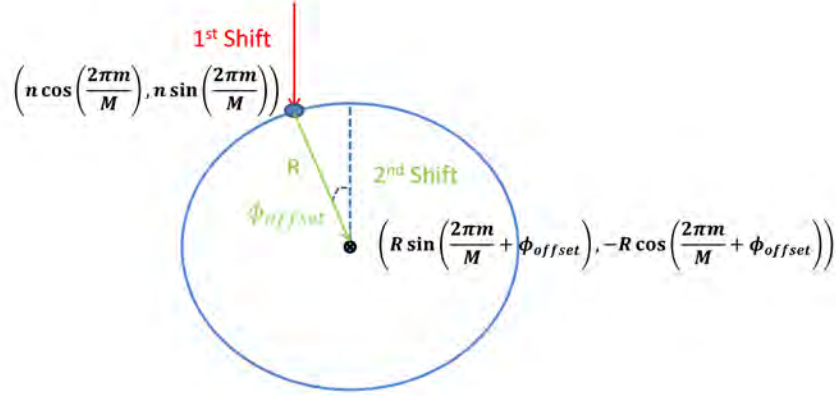
Figure 3.14. The first shift, described by the STF, places the object on the circumference of the transverse offset. A second shift then places the object to the center of the reconstructed image. Each shift is broken into its corresponding spatial components.

Applying the second shift to each element of the STF, Equation (2.17) now becomes

$$A_{m,n}(\bar{\xi}) = \exp[-2\pi\bar{\xi} \cdot \bar{p}_{shift}]. \qquad (3.1)$$

The projection angle shift, $\bar{p}_{shift}$ is

$$\bar{p}_{shift} = (n\cos(2\pi m/M) + R\sin(2\pi m/M + \phi_{offset}), n\sin(2\pi m/M) - R\cos(2\pi m/M + \phi_{offset})),$$
$$(3.2)$$

where R is the radius of the transverse offset and ϕ_{offset} is the observed phase term for each wavelength of interest. The phase term is found empirically using calibrated light sources. Failure to account for the transverse offset causes the shifted projection not to align properly and the quality of the reconstructed image degrades significantly.

3.6   Summary

In this chapter, the development of the simulation was covered. MATLAB controls functions within Zemax to produce simulations of object's spatial and spectral content. Three Zemax models were created: the paraxial, chromatic, and zernike phase surface. Each of these models have their utility in assessing different aspects of the reconstruction algorithm. The paraixal model was validated by matching the deviation angles measured by the GCTEx instrument. The chromatic model matches the blurring observed in the GCTEx. The Zernike phase surface demonstrated that controlled amounts of aberrations can be injected into the system. This chapter covered the source of the transverse offset had a lateral shift of 16.9 pixels, corresponding to a 20.5 arc minute alignment error within the prism. Finally, to correct for the transverse offset, a second shift in the reconstruction algorithm was added.

4. Reconstruction Assessment

With the models and simulations set, an evaluation of the reconstruction algorithm is required. For this thesis, only the fast reconstruction algorithm by Deming [10] is evaluated. There are four sets of test cases in this chapter, a set for each of the models described and an additional set taking data from the GCTEx instrument.

4.1 Metrics

The metrics for evaluating reconstruction performance are based off image quality measures used to gauge performance in compressing digital images. Since compression and the reconstruction process lose information original content, the image quality metrics are suited for measuring the reconstruction's performance. There are two categories of image quality metrics used: pixel-difference-based and edge based measures [1, 8].

A common pixel-difference-based metric is the Mean Square Error (MSE). For an image where there are M and N number of pixels in the row and column directions, respectively, the MSE is given by

$$MSE = \frac{1}{MN} \sum_{j=1}^{M} \sum_{k=1}^{N} \left(x_{j,k} - x'_{j,k} \right)^2, \tag{4.1}$$

where $x_{j,k}$ denotes pixel (j, k) of the original image and $x'_{j,k}$ pixel (j, k) of the reconstructed image. Higher values of MSE corresponds to poor image quality.

The Laplacian Mean Square Error (LMSE) has emphasis on the edges of the scene. This metric will gage the sharpness of the edges, offset in edge position, and missing

edges. The LMSE is defined as

$$LSME = \frac{\sum_{j=1}^{M} \sum_{k=1}^{N} \left[O(x_{j,k}) - O(x'_{j,k}) \right]^2}{\sum_{j=1}^{M} \sum_{k=1}^{N} O(x_{j,k})^2},$$ (4.2)

where the Laplacian operator, $O(x_{j,k})$ is

$$O(x_{j,k}) = x_{(j+1),k} + x_{(j-1),k} + x_{j,(k+1)} + x_{j,(k-1)} - 4x_{j,k}.$$ (4.3)

A larger value corresponds to a poor image quality. Together, these metrics will provide an objective method of measuring blurring or signal loss in the reconstructed images.

4.2 Paraxial Model Test Cases

The ideal optical system test cases use the paraxial model to isolate the reconstruction algorithm as the source for any degradation in image quality. Simulations evolve from a simple scene illuminated by a mercury pen lamp, to a static scene, and then a polychromatic scene.

4.2.1 Parameters for Reconstruction.

A simple scene with distinct spectral features is the first test case scenario. A 5x5 grid of the alphabet is illuminated by a mercury pen lamp. The mercury pen lamp produces spectrally narrow emission lines, therefore it is assumed the width of the emission lines are negligible. Four of the five strong mercury emission lines in the visible region are used, the 579.0 nm line is ignored due to the close proximity of the 576.9 nm line. Figure 4.1 is the result of one projection simulated. Note that each wavelength has been scaled according to Table 2.6.

The fast reconstruction algorithm has a filtering parameter, μ, which provides
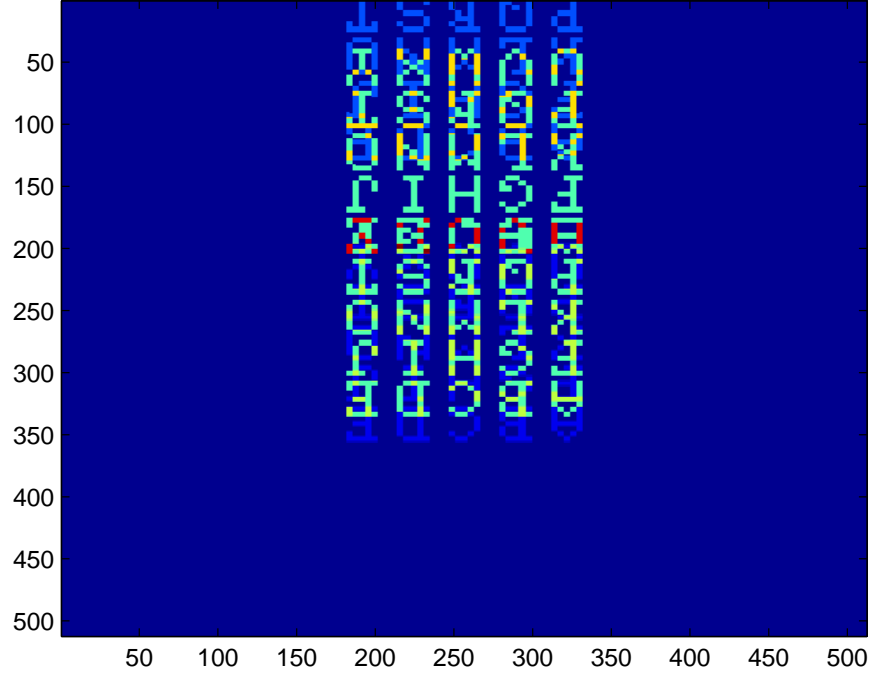
Figure 4.1. A 5x5 grid of letters illuminated by a mercury pen lamp. The wavelengths are scaled according to their relative intensities.

stability. Different values of the filtering parameter were tested, ultimately leading to the conclusion that μ must be greater than or equal to one for stability. Setting μ much larger than one essentially applies no filter and the results are similar to the unfiltered response. The filtering also forces the reconstructed images to have positive and negative values, centered about zero. The user must select which range provides the best results, and then set the other half equal to zero. If the negative range was selected, the absolute value was taken to provide more physical results.

The results of reconstructing the mercury pen lamp are shown in Figures 4.2(a)-4.2(d). For each wavelength of the mercury pen lamp, the unfiltered (left) and the filtered (right) reconstructed image is shown. This first set of results are from 100 projections simulated. The 404 nm and 576 nm, Figures 4.2(a) and 4.2(d) respectively, the negative range of the filtered reconstructed image were chosen.

As shown in Figures 4.2(a) and 4.2(d), the reconstruction algorithm is able to

60

(a) 404 nm

(b) 435 nm

(c) 546 nm

(d) 576 nm
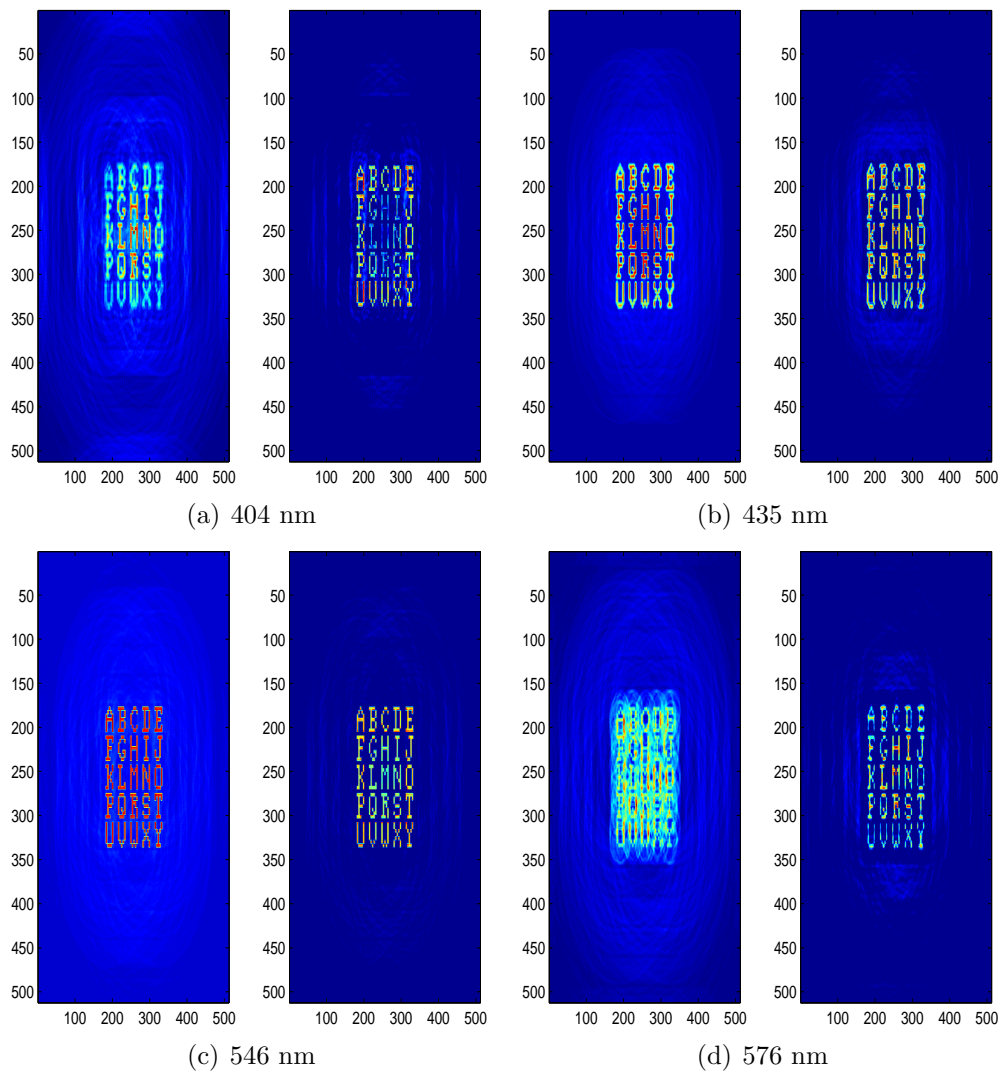
Figure 4.2. (a-d) Displays the reconstructed image for the unfiltered (left) and filtered (right) of each wavelength of the mercury pen lamp.

piece together the spectral contents well. The filtered images clean the surrounding noise but at the cost of signal drop. To calculate the signal, the reconstructed images must be scaled by the number of projections used in reconstruction. Since half of the filtered range is chopped, it must be multiplied by two to achieve signal strengths on par with the unfiltered images. A different multiplication factor is required if using values outside of $\mu = 1$. Figure 4.3 plots the mean signal of the grid (not the entire image) for each wavelength and compares it with input signal. The mean of the grid is computed because the reconstructed images do not have a uniform response across the grid.
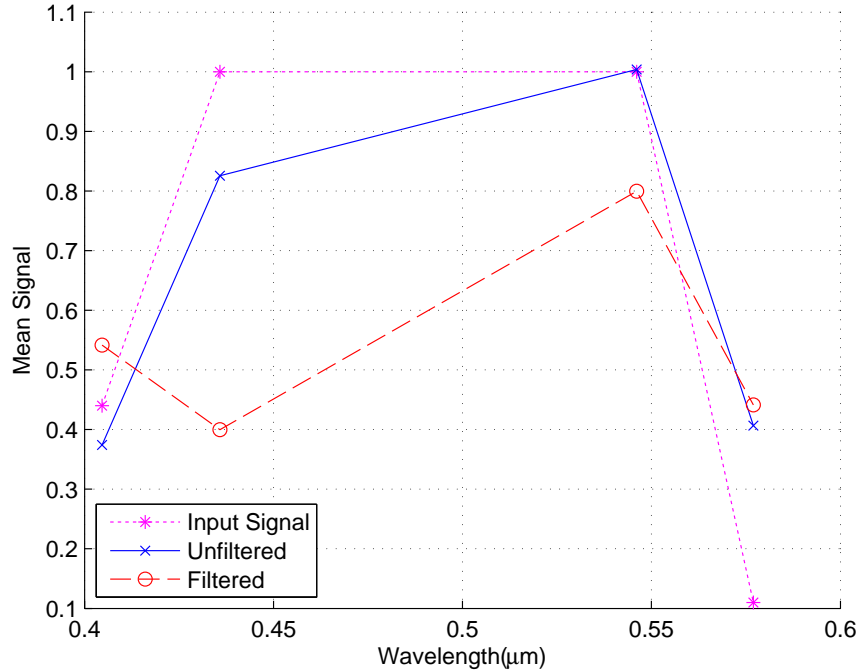
Figure 4.3. The mean signal of the grid for the filtered and unfiltered reconstructed images. The filtered images are have a large drop where the input signal is strong.

Where the input signal is at its peaks, the filtered signals are significantly lower, up to 60% lower than the input signal. The MSE is used to quantify the quality of the images are shown in Figure 4.4.
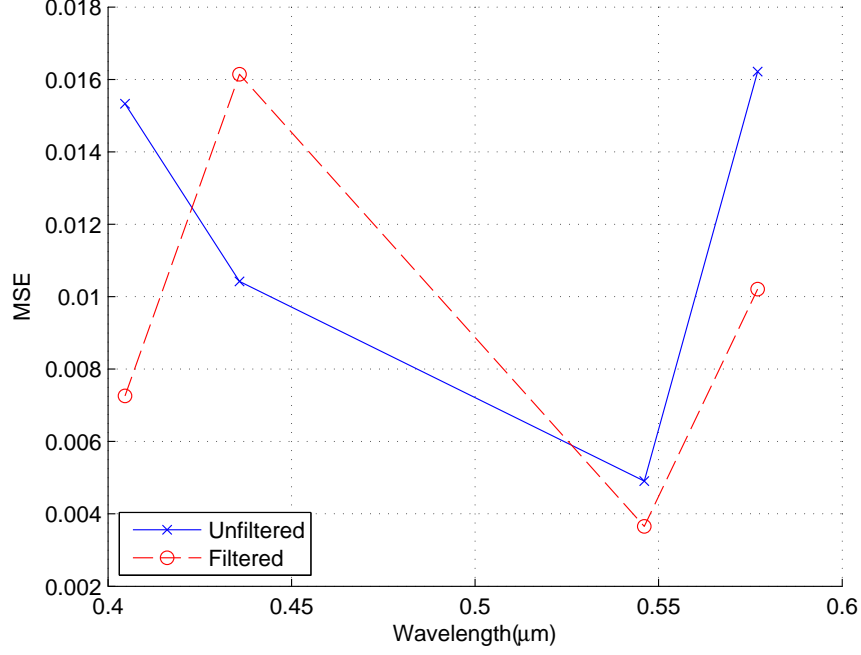
Figure 4.4. MSE for the unfiltered and filtered reconstructed images. With the exception of the 435 nm line, the filtered response has a better image quality.

Figure 4.4 shows the filtered images have higher image quality with the exception of the 435 nm line. As mentioned earlier, the filtered 435 nm reconstructed mean signal is substantially lower than the input signal and as a result the image quality is degraded as well.

The image quality is dependent on the number of projections used in the reconstruction algorithm. Figure 4.5 plots the MSE for unfiltered images with the number of projections, evenly spaced from 0 to 2π, are increased.

This shows that a minimum of 64 projections are required to obtain the best reconstructed images. After 64 projections, the marginal improvement is effectively zero for all the wavelengths.
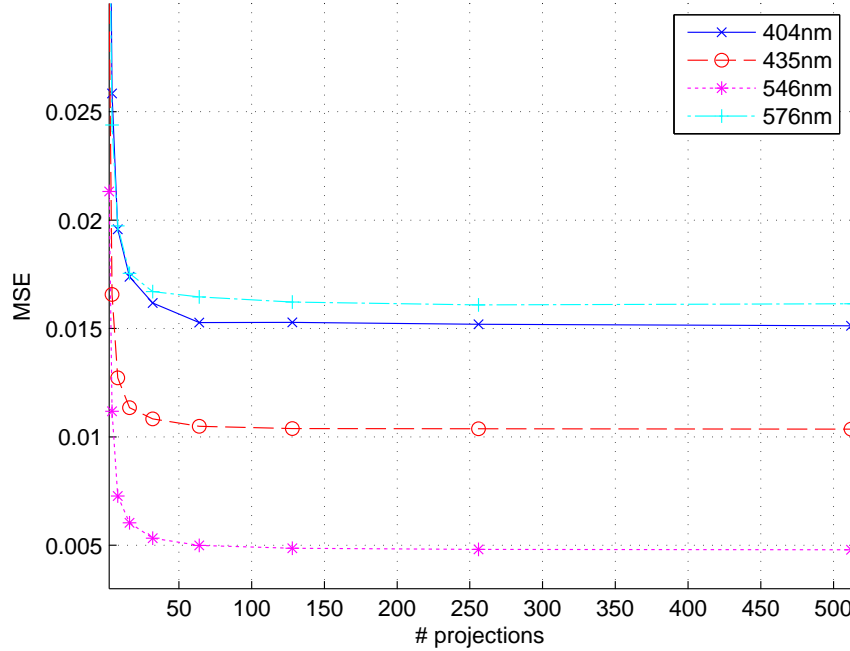
Figure 4.5. The performance of the reconstruction varies with the number of projections used. The reconstruction performance will not increase after 64 projections.

4.2.2 Static Scene.

A more complex scene is used to determine if the reconstruction algorithm can extract spectral features of a scene. A hypercube taken from the AVIRIS platform database [26] was simulated. This scenario demonstrates the effects of the chromo-tomographic process and reconstruction algorithm data taken from a calibrated HSI instrument.

The AVIRIS spectral range covers 224 bins with a resolution of approximately10 nm for each bin. AVIRIS frames from the 400-740 nm range were selected. For each bin, a 256x256 pixel clip of the scene was selected and zero padded to a 768x768 file size. This zero-padding is necessary to ensure the 256x256 scene was not truncated from the dispersion of the prism. The image field height was set such the output simulations matched the same dimensions as the inputted image so it is easily comparable. Each frame was normalized by the maximum bit-size of the AVIRIS format.

64

A projection simulated at 0 degrees is shown in Figure 4.6.
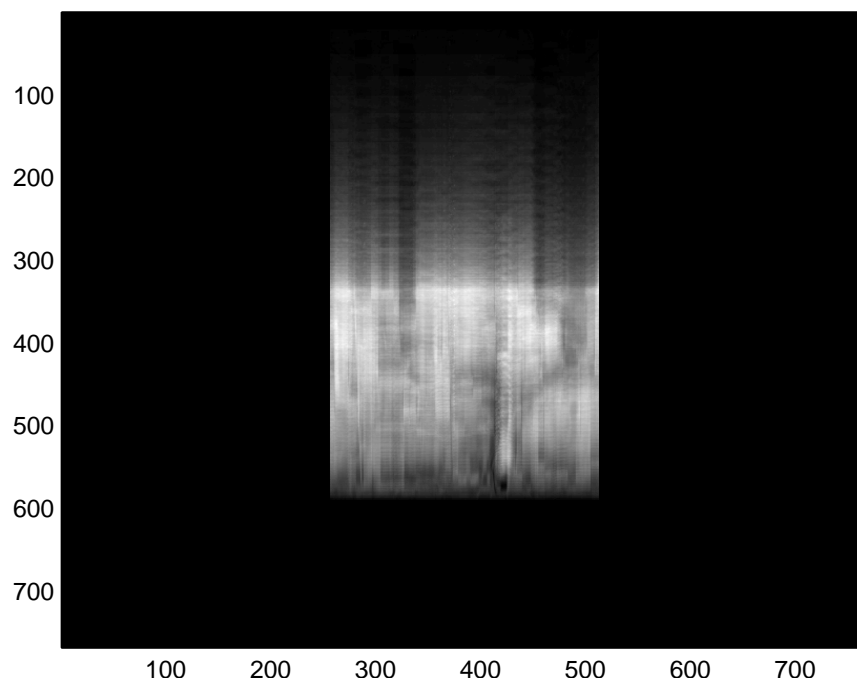
Figure 4.6. Simulation of the AVIRIS scene at a single projection. A zero-padding was adding to ensure all information was collected.

A total of 36 projections were simulated and placed through the reconstruction algorithm. A high-pass filter was added to both the unfiltered and filtered reconstruction to remove the lower spatial frequency content that was degrading the contrast of the scene. Figures 4.7(a)-4.7(c) shows the results of the reconstruction at the beginning, middle, and end of the band.

The unfiltered reconstruction clearly outperforms the filtered method at the middle wavelengths. However, the filtered reconstruction performs better than the longer wavelengths. Considering the entire data set, the longer wavelengths produced better quality reconstructed images. Shorter wavelengths lack of performance are attributed to the cone of missing information, i.e. the volume of the cone is larger for the shorter wavelengths. The middle wavelengths are inundated with the all of the other spectral

(a) 400 nm

(b) 550 nm

(c) 740 nm
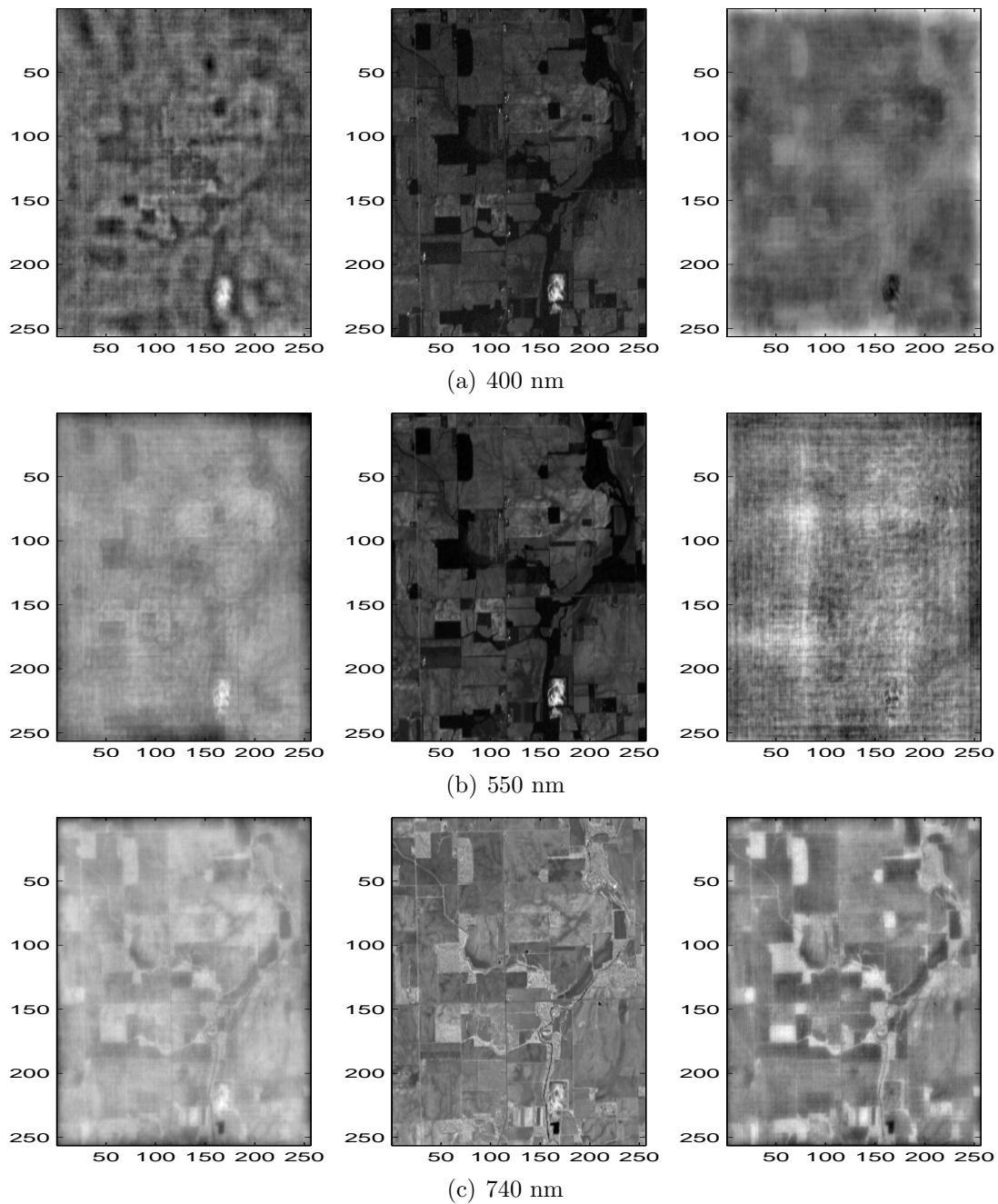
Figure 4.7. (a-c) Displays the reconstructed image for the unfiltered (left) and filtered (right). The center image is from the AVIRIS hypercube at the given wavelength.

(a) 695 nm
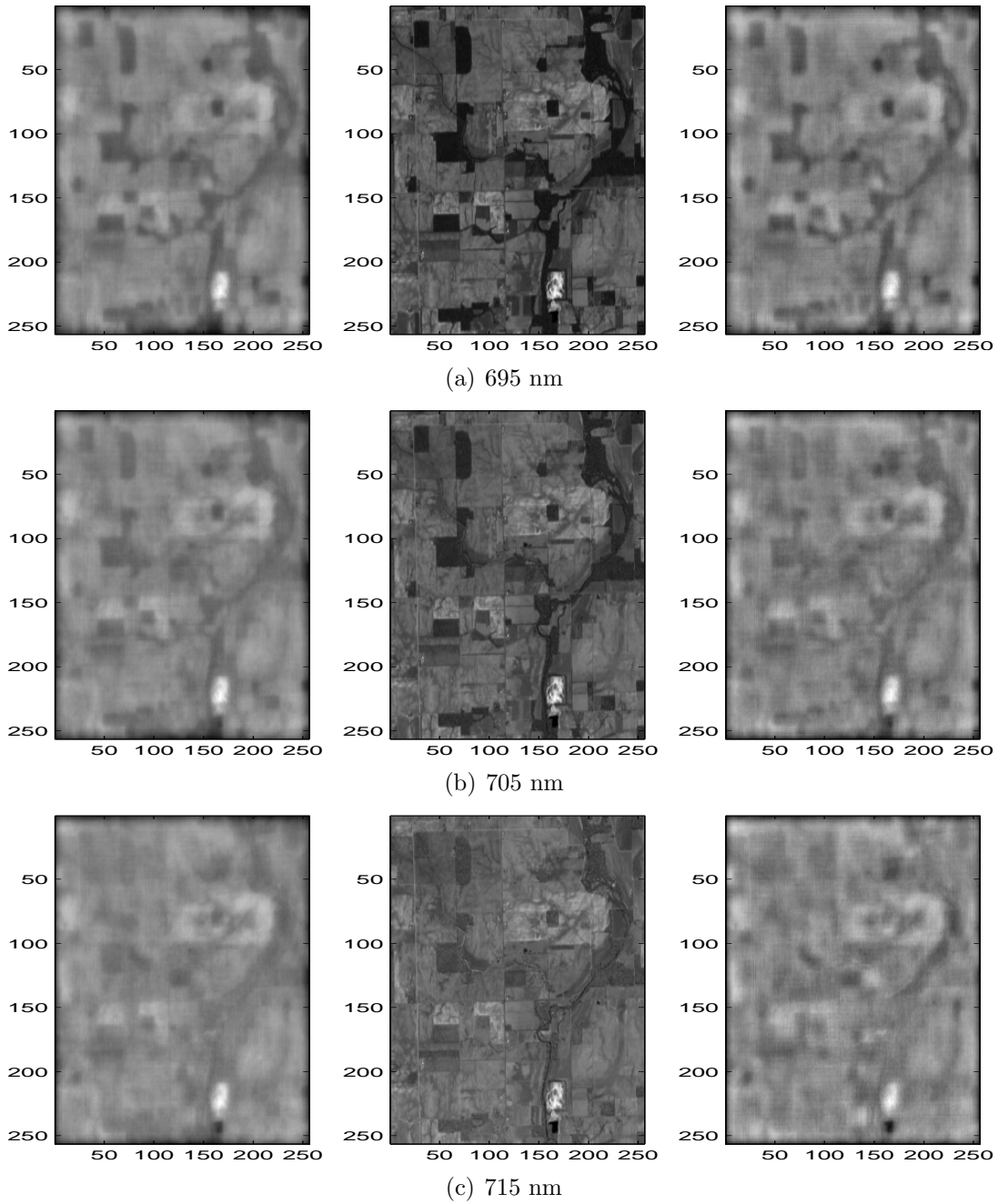
(b) 705 nm

(c) 715 nm

Figure 4.8. Demonstrates that the reconstruction process can identity spectral features such as when water begins to absorb light at 700 nm. Three successive bins at (a) 695 nm, (b) 705 nm, and (c) 715 nm are shown. The image on the left is from the unfiltered method, the center image is from the AVIRIS hypercube, and the filtered method is on the right.

content, its reconstructed image is thereby degraded.

Both the filtered and unfiltered reconstruction algorithms are able to pick out the distinct spectral features such as the water absorption line. Figures 4.8(a)-4.8(c) show three bands that show when water starts to absorb at 700 nm.

The dark patches in the scene are vegetation and as water starts to absorb the vegetation's reflectance is increased thereby the reflected signal from vegetation increases. These test demonstrated the fast reconstruction algorithm is able to reconstruct the longer wavelengths adequately; however, more advanced reconstruction algorithms are necessary to fill in the cone of missing information.

4.2.3 Polychromatic Scene.

A polychromatic scene is modeled by four Gaussian sources, representative of a light-emitting-diode, at varying wavelengths. Each of these sources are then spatially tied to a letter in the acronym, AFIT, as shown in Figure 4.9. The letter A is associated with the red source, letter F with the blue, letter I with green, and the letter T with yellow.

The sources are arranged such that they overlap spectrally but not spatially. Each source has a maximum intensity of one and a FWHM of 50 nm. The blue, green, and yellow sources intersect at their corresponding FWHM, while the red source is separated further to cover more of the visible spectrum. Figure 4.10 plots the spectral distribution of for all the sources.

Like the static scene, the size of the image file is zero-padded to ensure that all of the dispersed scene is captured and rescaled for comparison. The granularity of the spectral profile is in 10 nm increments and a total of 36 projections were simulated. Figure 4.11 shows the simulation output from a projection at 0 degrees. Note that the letters are dispersed at different distances onto the FPA.
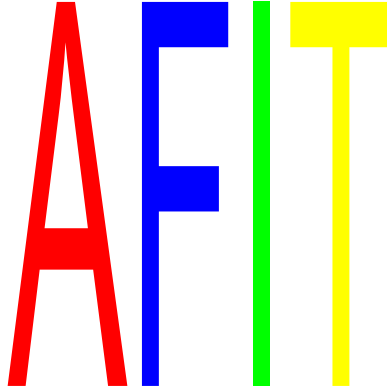
Figure 4.9. Illustration of the scene simulated, with no spatial overlap but spectral overlap from each source.
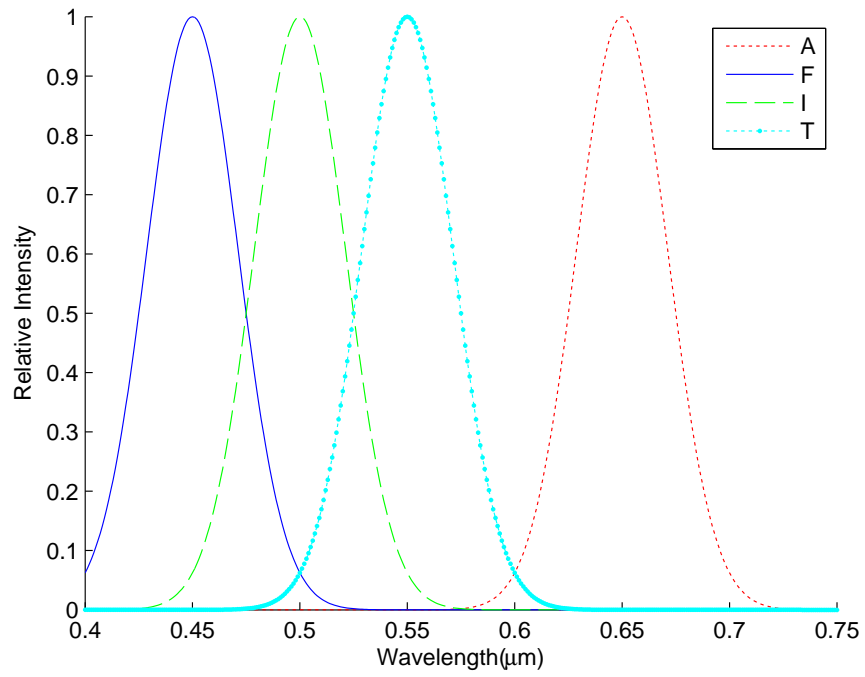
Figure 4.10. Spectral profile of the simulation. The FWHM of each Gaussian source is 50 nm and spaced to overlap one another.
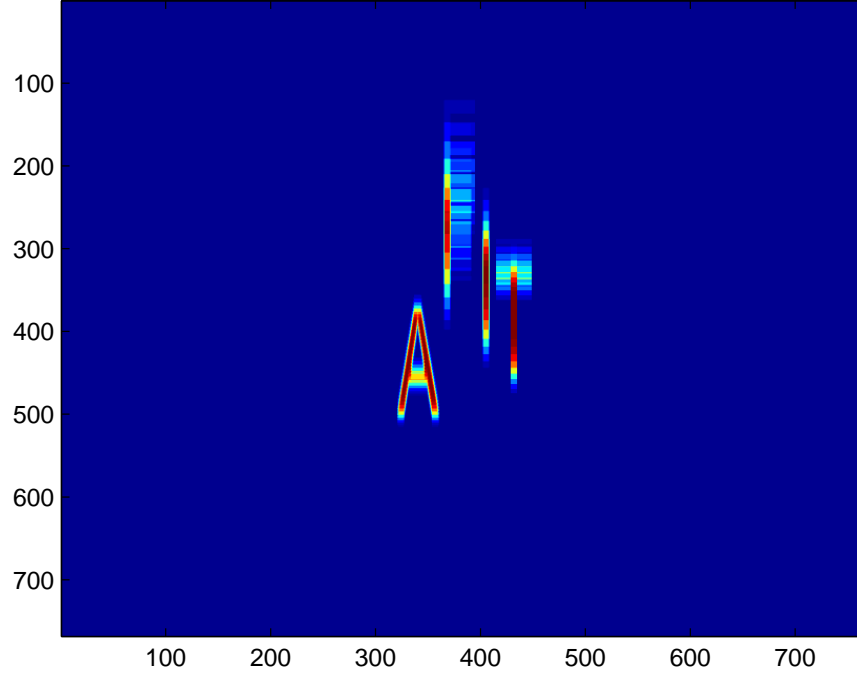
Figure 4.11. Each letter is shifted at different distances due to their varying spectral content. The latter three letters have approximately 50 nm of overlap.

The reconstructed images at their respected peaks are shown in Figures 4.12(a)-4.12(d). For each figure, the unfiltered and filtered reconstructed images are shown left and right, respectively. As depicted, the filtering reduces the noise from the surrounding spectral content.

The spectrum of the reconstructed images is computed as the mean intensity for each spatial letter as a function of wavelength. Figures 4.13(a) and 4.13(b) show the peaks at the shorter wavelengths are shifted and that the intensity increases considerably at longer wavelengths.

The unfiltered spectrum has significant bleeding into the blue source from the other spectral channels. The filtered spectrum considerably eliminates most of the cross-source bleeding. The unfiltered spectrum results have much larger FWHM for each source, as summarized in Table 4.1. The filtered spectrum's FWHM are close to the actual input FWHMs of 50 nm. The blue and green source peaks are shifted

70

(a) 450 nm

(b) 500 nm

(c) 550 nm

(d) 650 nm
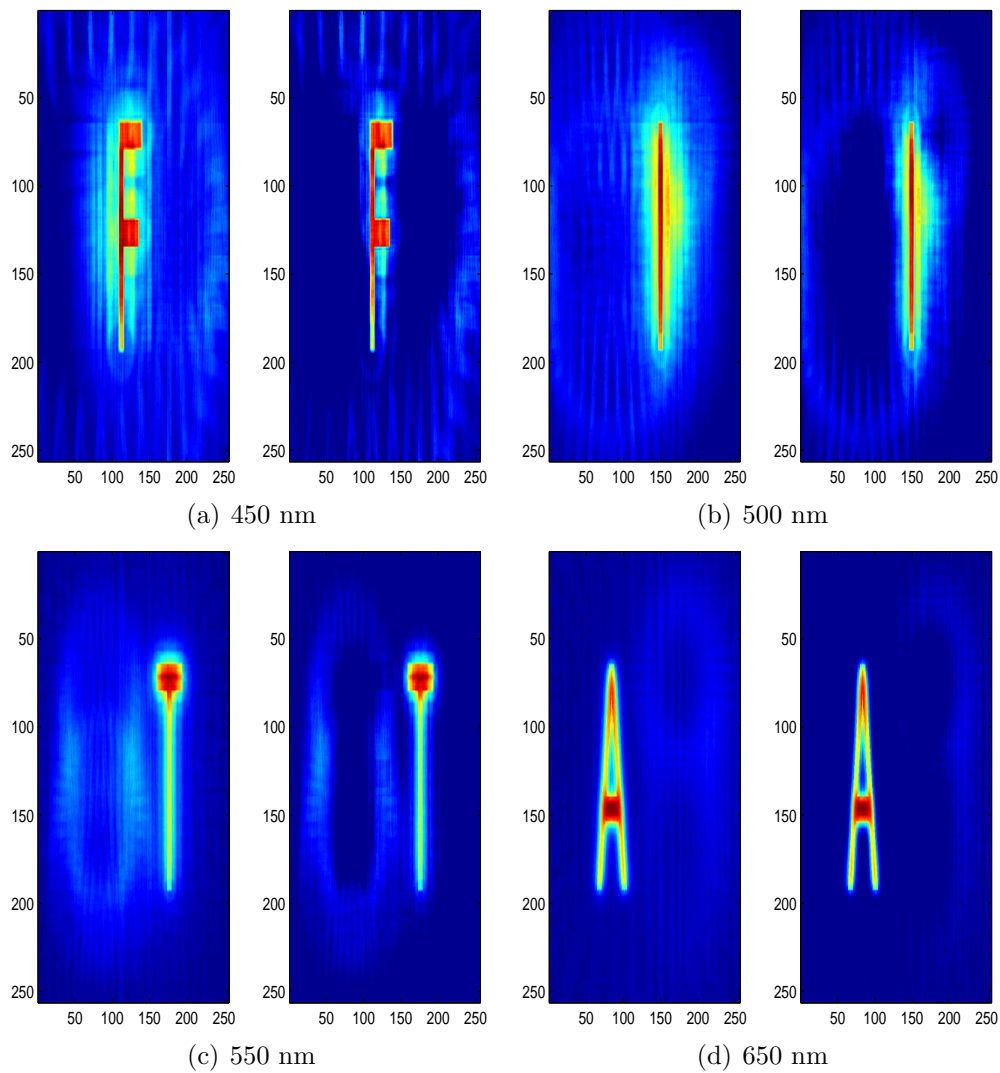
Figure 4.12. (a-d) Displays the reconstructed image for the unfiltered (left) and filtered (right) of each spectral peak wavelength.
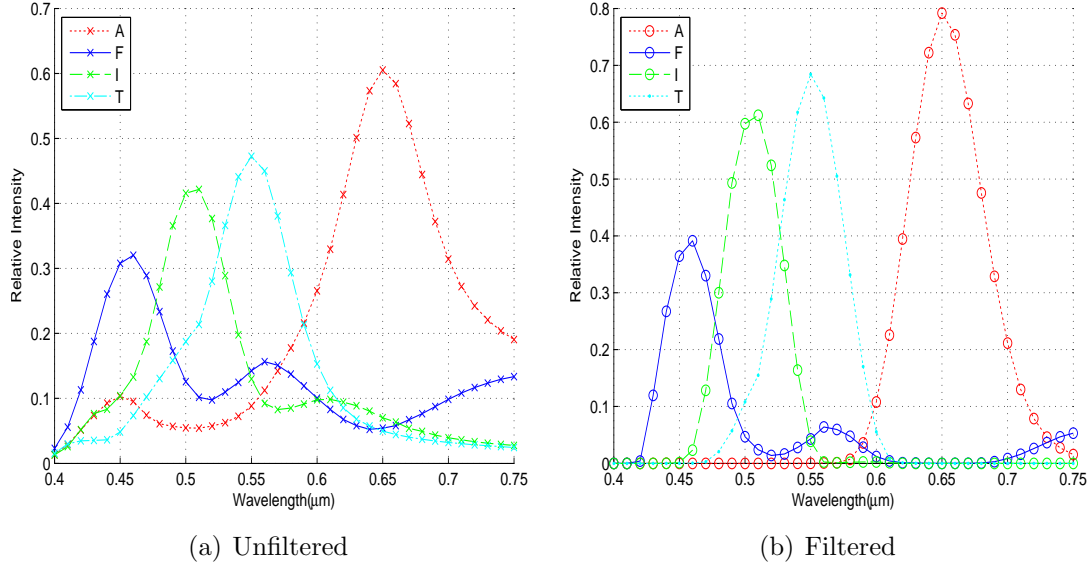
Figure 4.13. (a) Unfiltered spectrum showing bleeding of the sources. (b) Filtered spectrum significantly reduces the spectral widening. The shorter wavelength peaks shift as the intensity of the longer wavelengths increases.

by 10 nm for both sets of reconstructed images.

All of the sources have lower reconstructed intensities than the actual source amount. The drop in intensity is more pronounced at the shorter wavelengths where the dispersion from the prism is at its greatest. The fast reconstruction algorithm is unable to maintain the absolute radiometric intensity but the general profile or shape of the spectrum is maintained.

Table 4.1. FWHM of the unfiltered and filtered reconstructed spectrum. Ideally, the FWHM should be 50 nm for each source.

Letter (color)	Unfiltered FWHM (nm)	Filtered FWHM (nm)
A(red)	97.0	65.3
F(blue)	66.4	46.9
I(green)	65.8	52.0
T(yellow)	73.7	52.0

The MSE of the filtered images are also better than the unfiltered as indicated in Figure 4.14. Interestingly, MSE degrades at the spectral peaks, more so for the

72

shorter wavelengths than the longer wavelengths.
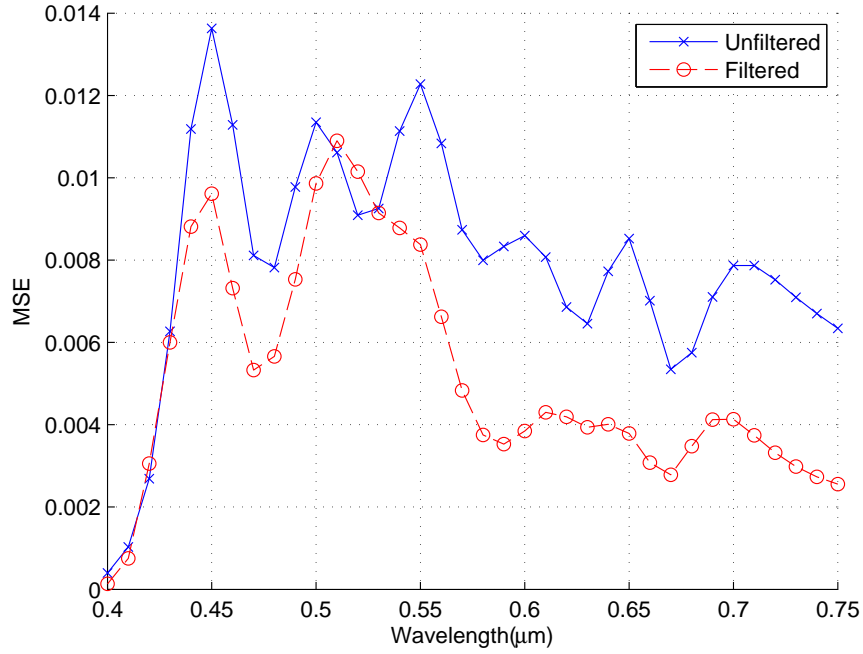
Figure 4.14. MSE spikes at the shorter wavelength peaks due to the difference of the reconstructed signal strength verse the actual signal. The error in the filtered reconstructed images is lower because the residual noise artifacts from the other spectral channels are reduced.

The elevated MSE at the peaks are due to the difference from the reconstructed signal strength verse the actual signal. As the actual signal peak occurs, the large signal difference drives the MSE upwards. Conversely, as the wavelengths move from the spectral peaks, the difference between signals is not as great resulting in a lower MSE. This explains why the MSE at the 650 nm, where the reconstructed intensity is greater, has a lower MSE value.

In short, the fast reconstruction algorithm is able to resolve the spectral features; however, it is unable to maintain its absolute radiometric quantity. Filtering is required to prevent noise from the other spectral channels from seeping into the channel of interest.

4.3 Chromatic Model Test Case

This test case uses the chromatic model to investigate how chromatic blurring impacts reconstruction. A simple scene with an object with high spatial frequency, shown in Figure 4.15, is simulated.
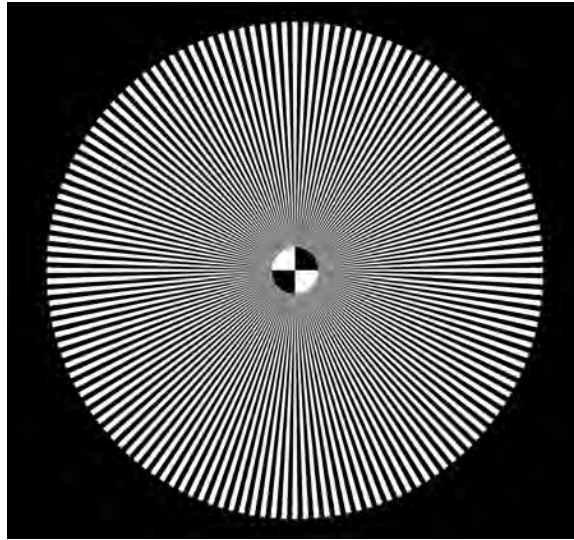
Figure 4.15. This object has high spatial frequency which will be blurred by chromatic aberrations.

The object's spectral intensity is uniform over the spectral range from 400-750 nm and the scene is simulated in 25 nm increments. The chromatic model was focused at the 550 nm wavelength. A uniform spectrum was chosen to remove any negative impacts the spectral features may have in the reconstruction algorithm. Since high spatial frequency content is lost due the cone of missing information, the same test case was also simulated in the paraxial model for comparison. The filtered reconstruction does not perform well reconstructing the high spatial frequency content, so only the unfiltered results are presented. Figures 4.16(a)-4.16(d) show the reconstructed images for paraxial (left) and chromatic (right) simulations for several wavelengths over the spectral range.

(a) 400nm

(b) 550nm

(c) 650nm

(d) 750nm
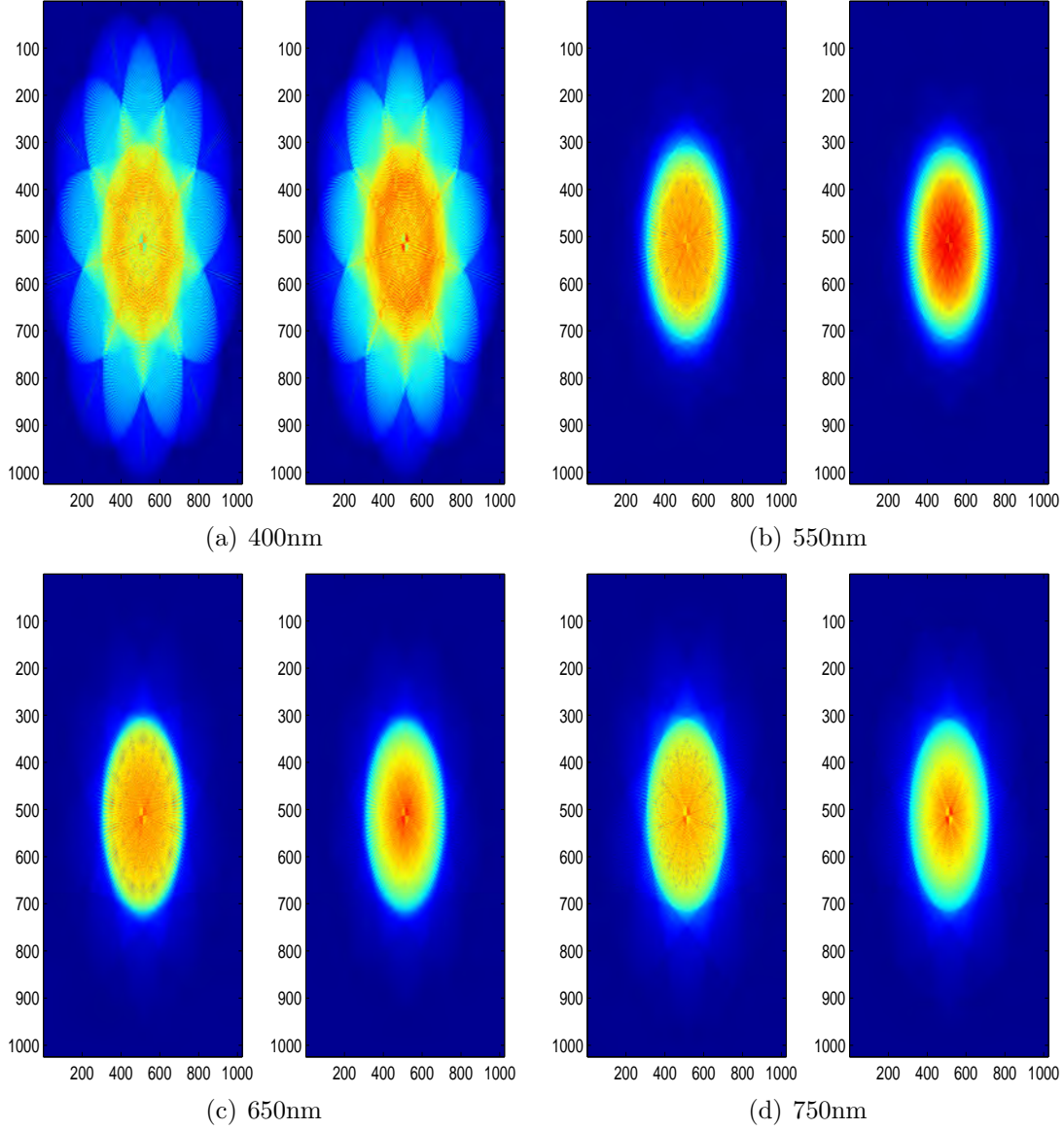
Figure 4.16. (a-d) Reconstruction of the high spatial frequency object using the paraxial, left, and chromatic, right, models. Due to the cone of missing information, both sets of reconstructed images have a significant degradation in image quality. Loss in image quality is more pronounced at the ends of the spectral range.

The 400 nm reconstructed images do not constructively combine each shifted projection as effectively as the other wavelengths, resulting in the residual artifacts to be more prevalent. This is consistent with the static scene and AFIT test cases where the short wavelength reconstructed images have poor image quality and the longer wavelengths performed better. This again is attributed to the cone of missing information, where the longer dispersion at the short wavelengths cause a larger cone to be formed therefore degraded reconstructed images.

The chromatic aberrations shift the spectral location of the highest quality reconstructed image as shown in Figures 4.16(b) and 4.16(c). Since the chromatic model was focused at 550 nm, the highest quality reconstructed image occurs near the 550 nm while the paraxial model forms the best reconstructed image at 650 nm. To qualify the image quality, the LMSE metric is used to put emphasis edges of the high spatial frequency object. Figure 4.17 plots the LMSE over the spectral range.

The chromatic model performs better than the paraxial model at the shorter wavelengths likely from the adjustment in focus in the chromatic model. However, the chromatic model performs poorly at the longer wavelengths and a the chromatic model substantial difference in the troughs of the curves. The chromatic model has a narrow operating range from roughly 525 nm to 575 nm where high spatial frequency content is best maintained.

4.4 Zernike Phase Surface Model Test Case

This test case is similar to the chromatic model with the exception that different combinations of Zernike coefficients are used to add controlled amounts of aberrations. Like the chromatic model test, each aberration term is simulated by a uniform spectrum to observe how the aberrations degrade image quality of the high spatial frequency object, shown in Figure 4.15. This provides a characterization of which
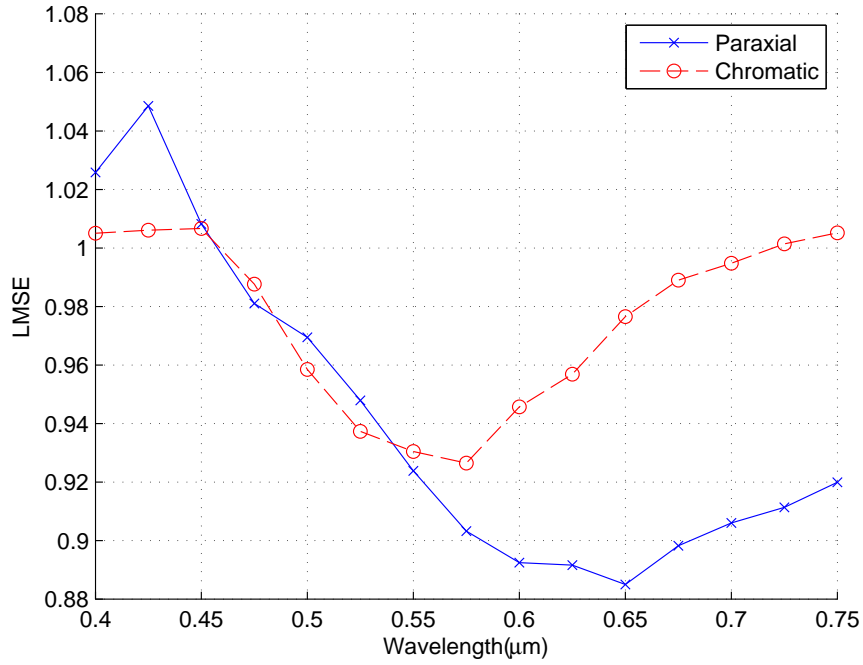
Figure 4.17. The high spatial frequency content is best preserved at 550 nm where the focus of the chromatic model was at. A small operating range exists for maintaining the spatial content.

aberrations are the most detrimental for the future spaced-based system to avoid.

This test case only considers the effects of astigmatism, coma, and spherical aberrations. From Table 2.3, the astigmatism and coma aberration terms consist of two Zernike coefficients, each of the coefficients are equally increased. Furthermore, the coefficients where balanced such that only the aberration under test existed in the Zernike phase surface. For example, coma consists of the Z_6 and Z_7 coefficients which are also present in the tilt combination. To zero out the tilt, an offsetting amount of the Z_1 and Z_2 were applied.

Each aberration was incrementally increased from 1 wave to 5 waves to 10 waves. All of the aberration terms are referenced to 550 nm. Zemax's geometric image simulation, vice the image simulation, was used for these simulations since geometric ray tracing is required in the presence of strong aberrations. Once again, the LMSE

77

metric is used to qualify the high spatial frequency object. Figures 4.18(a)- 4.18(c) plot the LMSE for each of the aberrations as the number of waves increases. Each plot contains a reference LMSE where no aberrations were added.

(a) 1 wave

(b) 5 waves

(c) 10 waves
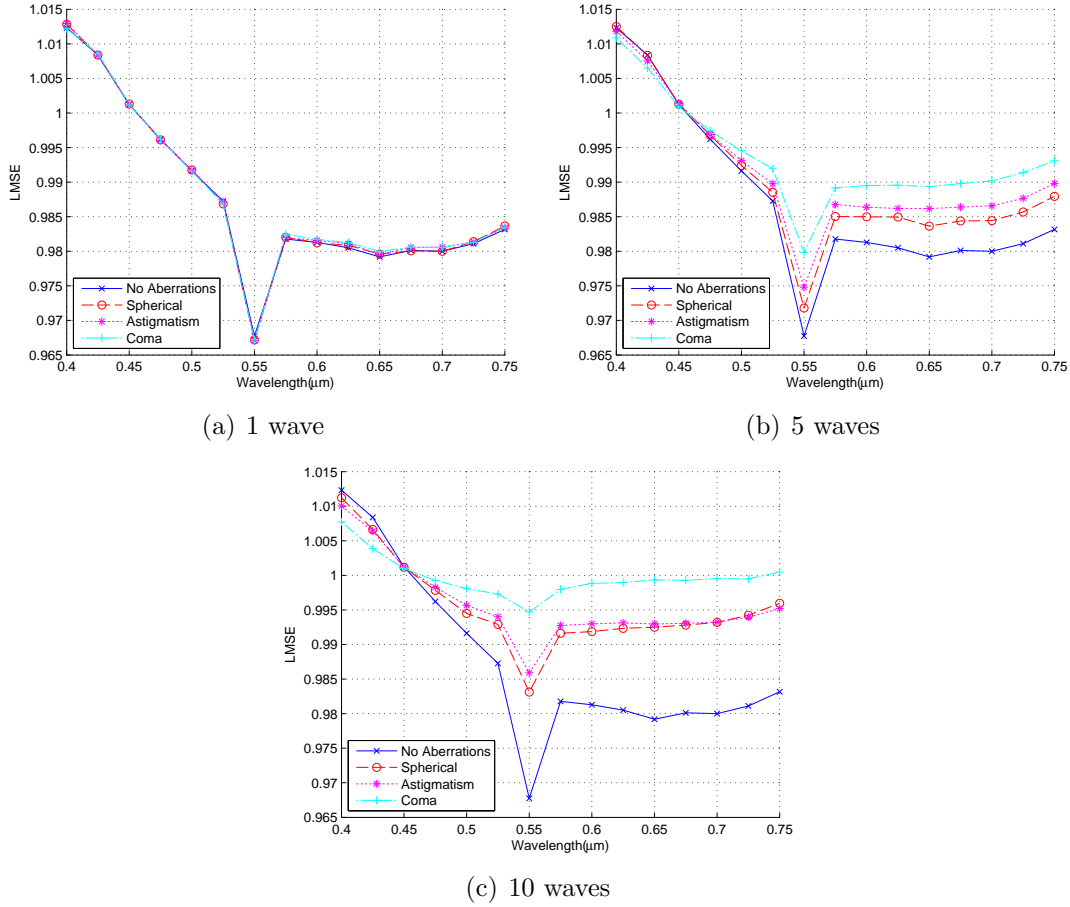
Figure 4.18. (a-c) LMSE for each aberration as the number of waves are increased. One wave of aberrations have little impact on the image quality. However, steadily increasing the amount of waves shows that coma degrades the reconstruction performance the most. The longer wavelengths reconstruction performance degrades more rapidly than the shorter wavelengths.

A subjective LMSE threshold of 0.990 is used determining if the reconstruction images are acceptable for identifying the actual object. The threshold was based upon looking at reconstructed images from the simulations produced without any aberrations. Spatial features, such as the spokes of the object, are clearly discernible with

a LMSE of 0.990 or lower. Figures 4.19(a) and 4.19(b) illustrate two reconstructed images across the LMSE threshold.

(a) LMSE=0.9916   (b) LMSE=0.9873
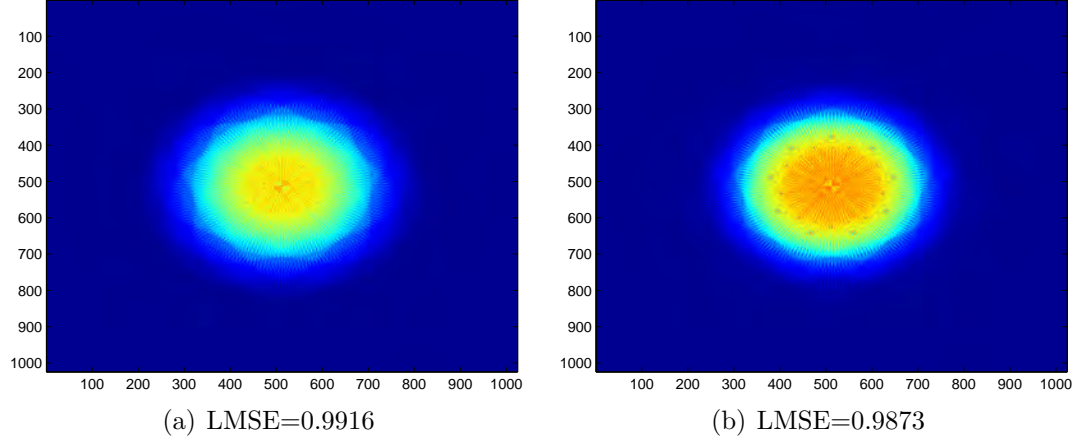
Figure 4.19. Two reconstructed images above (a) and below (b) the subjective LMSE threshold value of 0.990.

Once again, the shorter wavelengths perform worse than the longer wavelengths. The 550 nm reconstructed image produces the best reconstructed image for all sets of reconstructed images. This differs from the chromatic test case where the paraxial model produced the best reconstructed at 650 nm. The results vary from differences in the image simulations as the geometric image simulation does not maintain the object's high spatial frequency content as well as the convolution image simulation. The differences in the simulations are trivial provided trends of how aberrations impact reconstruction performance are identified.

One wave from each of the three aberrations have little effect on the reconstruction performance. However increasing the amount to 5 waves, the reconstruction performance is degraded predominantly at the longer wavelengths. Coma clearly negatively effects the reconstruction performance the most, while spherical aberrations degrade image quality slightly more than astigmatism. At 10 waves of aberrations, the negative effects on reconstruction are compounded. Coma effectively blurs the

reconstructed images over entire spectral range. Astigmatism and spherical aberrations have a narrow range of 40 nm centered at 550 nm where the image quality is below the threshold value.

4.5 Lab Experiment Test Cases

Simple laboratory experiments of a monochromatic scene of the Air Force bar chart was collected. Next, an iris directly in front of a mercury pen lamp was placed to simulate a point source. For each of these experiments, the transverse offset correction was applied to the reconstruction algorithm.

4.5.1 Air Force Bar Chart.

An Air Force bar chart was measured using a mercury light source with a narrowband filter at 546.8 nm. The prism was spinning at a rate less than 1 rev/sec. Data recorded at a single projection is shown in Figure 4.20. Notice that two bar charts are observed in the measured projection, with one in focus and the other blurred. The blurred bar chart is believed to be a ghost reflection caused by internal reflections within the instrument.

It is possible that secondary blurred bar chart is from another emission line from the source; however, the shift between each bar chart is more than 90 pixels which corresponds to 1.2 degrees of deviation. Since the bar chart in focus is at 546.8 nm, the 1.2 degrees of deviation corresponds to emission lines roughly at 460 nm or 800 nm, neither of which are strong emission lines for a mercury source.

A total of 50 projections of the bar chart were collected and applied the reconstruction algorithm without any correction for transverse offset. The resulting reconstructed image is shown in Figure 4.21.

The reconstructed algorithm severely degrades the image. The transverse offset
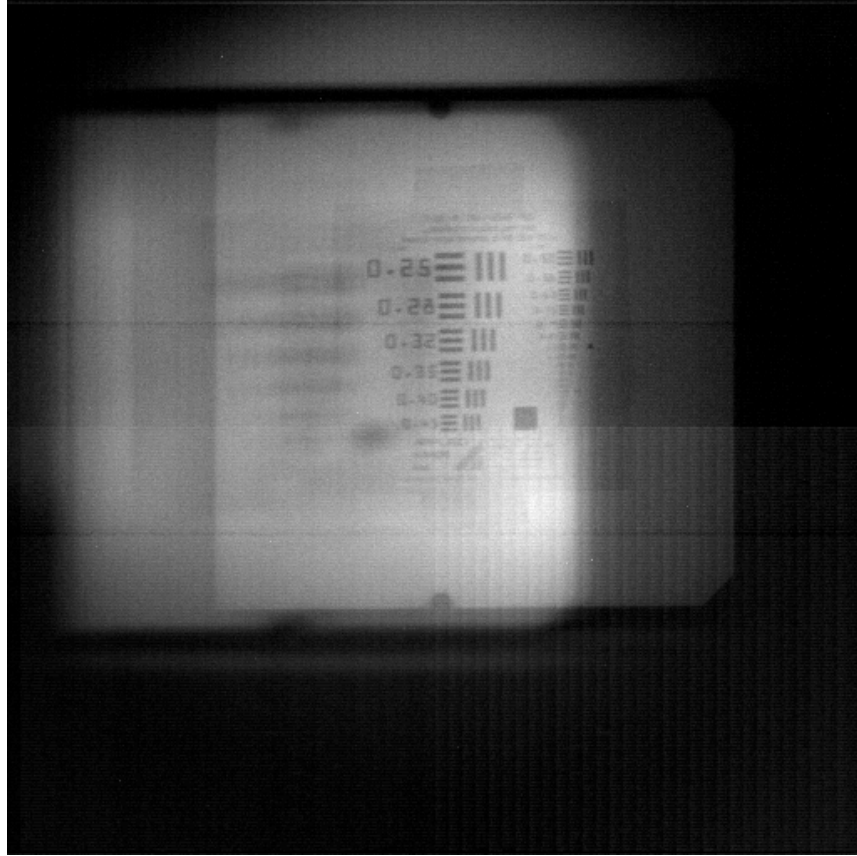
Figure 4.20. Air Force bar chart illuminated by a monochromatic source at 546.8nm.

causes the object to destructively interfere with itself resulting in a blurred image. This is quickly resolved by applying change in the reconstruction algorithm, described in Section 3.5.1, to account for the transverse offset. The reconstructed image of the bar chart is shown in Figure 4.22.

A significant improvement from the two reconstructed images. The spatial content of the image is now maintained with the correction. The lower spatial frequencies are saturating the reconstructed image thereby lowering the contrast. A Gaussian high-pass filter is also applied to the reconstructed image to enhance the contrast as shown in Figure 4.23.

The MTF of the corrected reconstructed image with and without the high-pass filter was calculated using Equation (2.5) by Hawks [20]. The results are plotted in
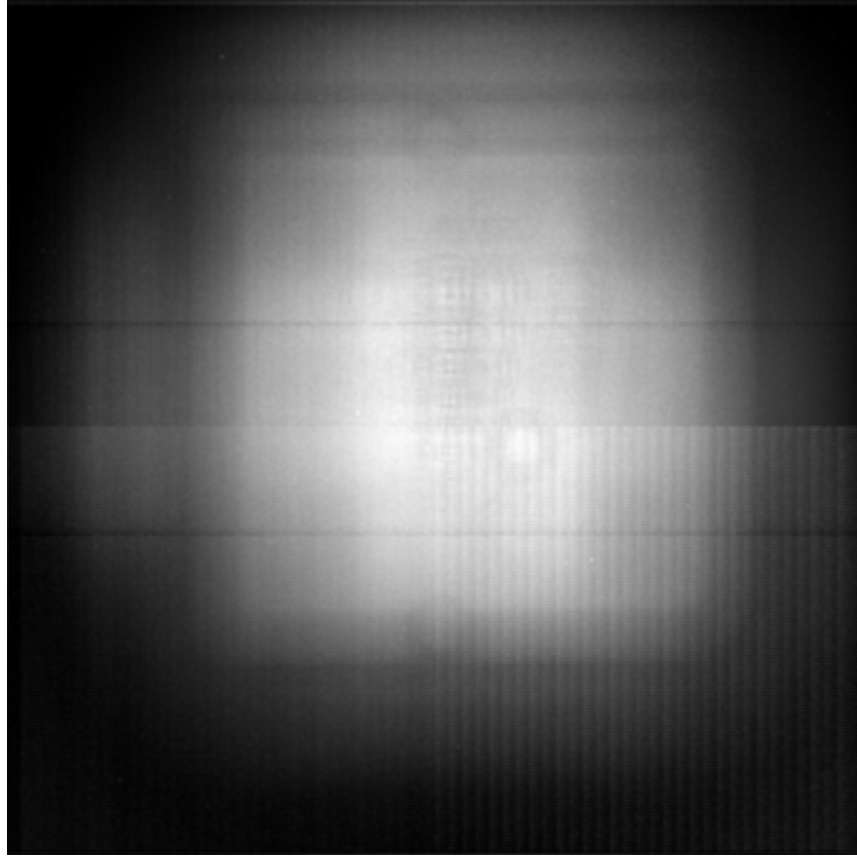
Figure 4.21. Air Force bar chart reconstructed without applying the transverse offset correction.

Figure 4.24.

The high pass filter improves the MTF by 4 times the lower frequencies. The significance of these results validates that transverse offset correction and upgrade in electronics deliver the correct prism angles necessary to perform accurate reconstruction. No additional corrections were applied or manual manipulation of the data was used in the data collection and/or reconstruction algorithm.

4.5.2 Mercury Pen Lamp.

The objective of this test case is to determine if the fast reconstruction algorithm produce a data cube of a spectrally simplistic scene. A point source using a mercury
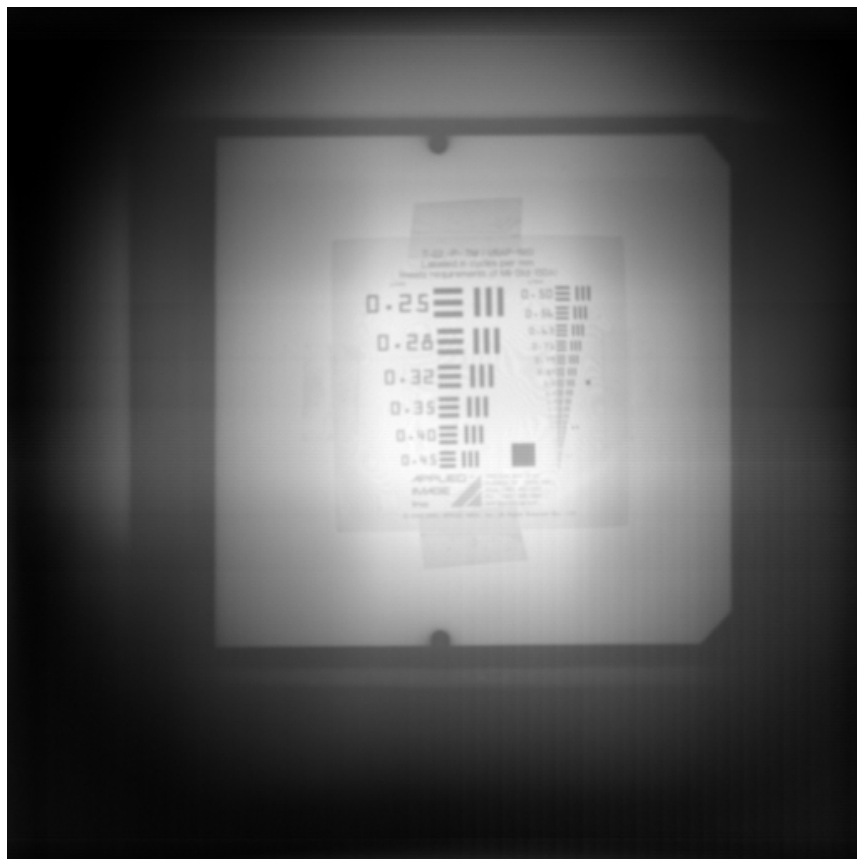
Figure 4.22. Transverse offset applied and the bar chart's lines are now observable and distinct.

pen lamp was collected using the GCTEx instrument. The reconstructed images of the mercury pen lamp were constructed from 50 projections and are shown in Figures 4.25(a)- 4.25(c). The instrument was adjusted such that the 546.8 nm line was in focus.

The transverse offset correction was applied and the phase lag terms were adjusted so each spectral bin would converge to a point. Table 4.2 lists amount of phase lag for required for each emission line. All of the phase lags terms are calculated empirically.

The 435.8 nm spot size is considerably larger than the other emission lines due to chromatic aberrations. The phase lag correction is not perfect as the reconstruction doubled the spot size of the 435.8 nm line. However, it does perform well where the
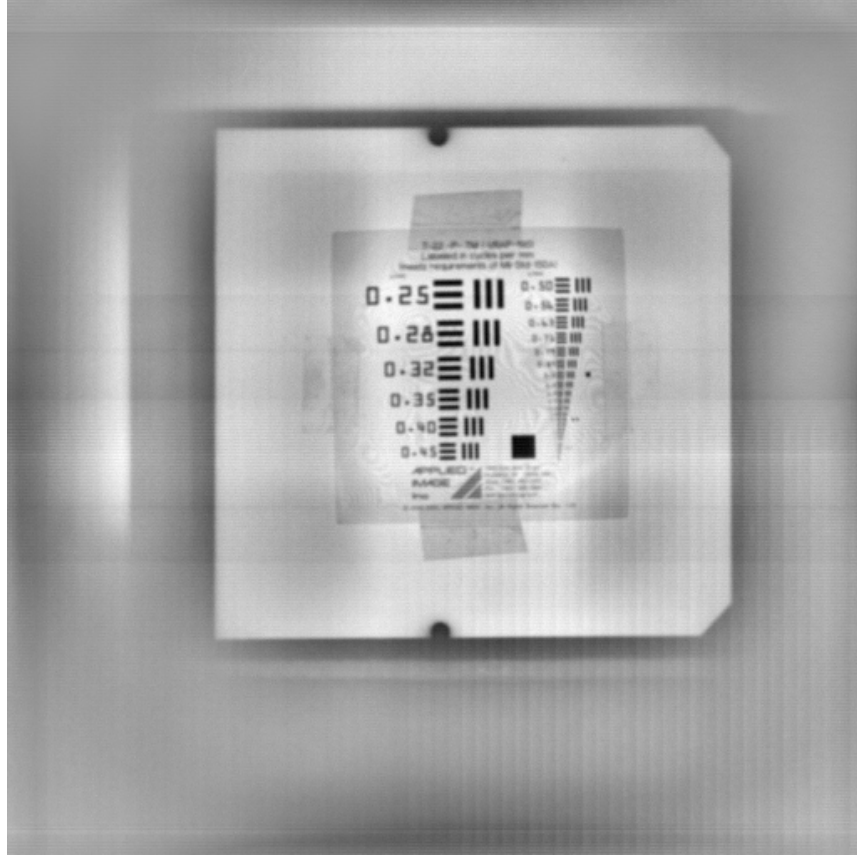
Figure 4.23. High pass filter improves the contrast of the reconstructed image. [20]

emission lines had a tighter focus. The results show the corrected algorithm is capable of adjusting for scenes with varying spectral content.

To provide an estimate of the fast the reconstruction algorithm is, this test case was clocked using MATLAB's code timing mechanisms. To load the 512x512 pixels camera files, read in the prism angle data, backproject 50 projections for 3 spectral bins, and apply a filter takes an average of 3.50 seconds. The previous AFIT backprojection algorithm required several minutes for an equivalent reconstruction.
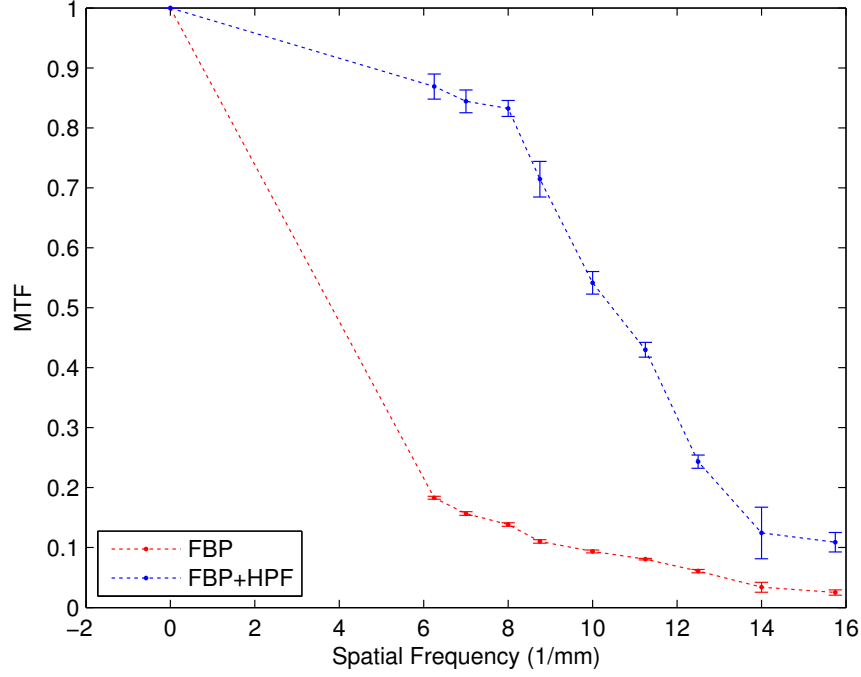
Figure 4.24. MTF calculated from the US Air Force bar chart with and without the high-pass filter. The high-pass filter substantially improves the resolving power of the reconstruction algorithm. [20]

Table 4.2. Phase lag adjustment required for each emission line in reconstruction.

Emission Line (nm)	Phase Lag (Degrees)
435.8	-35.21
546.8	-11.92
576.9	0

4.6   Summary of Results

This chapter demonstrated that the fast reconstruction algorithm is capable of reconstructing simple and complex scenes. For each reconstructed image, 64 projections that span from 0 to 2π produce the best results. More than 64 projections do not provide any significant improvement in the reconstruction results.

The fast reconstruction algorithm is able to reconstruct static scenes and distinguish spectral features such as the water absorption line. However, the algorithm's performance over the spectral range is poor due to the cone of missing informa-

(a) 435.8 nm

(b) 546.8 nm

(c) 576.9 nm
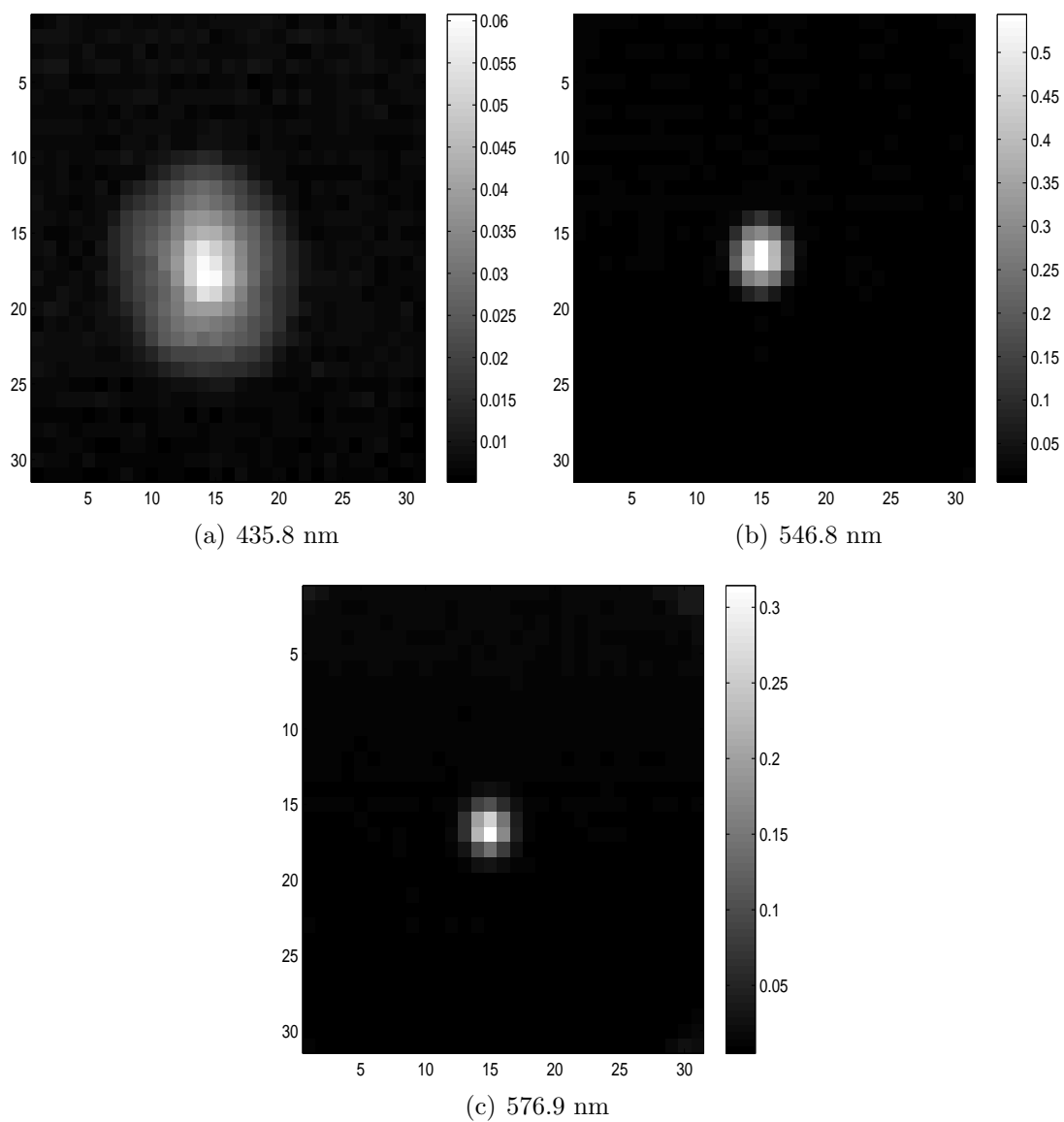
Figure 4.25. (a-c) Reconstructed images of the mercury pen lamp point source.

tion. The reconstruction algorithm is able to identify the shape of spectral sources as demonstrated with the polychromatic test case. However, shifts in the peak along with an lowered intensities, particularly at the shorter wavelengths, prevent it from providing absolute radiometric profile. The fast reconstruction algorithm has utility as a "quick look" algorithm and can an input for more complex algorithms such as the algorithm developed by Gould [16].

From the chromatic test case, high spatial frequency objects do not maintain integrity attributed to the cone of missing information. The reconstruction performance is degraded by the effects of chromatic and monochromatic aberrations. The chromatic aberrations force a small operating range where the blurring does not significantly degrade reconstruction performance. The aberration test case concluded that coma hindered reconstruction performance the most.

Finally, lab experiments showed accounting for the transverse offset is critical for the system to obtain valid reconstructed images. The bar chart test validated that the upgrade in electronics now sufficiently sync the camera and prism angles. The instrument and reconstruction algorithm are ready for more complex scenes and transients to be observed.

5. Conclusions and Recommendations

This chapter provides a summary of the research conducted in this thesis. Conclusions are made on the model and simulation, the fast reconstruction algorithm, and the transverse offset. Future work recommendations are then given. The conclusions made do not fully summarize the instrument's performance. Since the instrument's performance is dependent on the scene, the conclusions drawn are specifically for the scenes simulated.

5.1 Model and Simulation

Zemax and MATLAB proved to be a powerful combination. The simulated scenarios are a small portion of the simulation's capability. The simulated scenarios in this thesis demonstrated the orthogonal basis set of possible scenarios: spatially complex but spectrally simple and spectrally complex but spatially simple. Furthermore, the simulation allows flexibility in the design of the optical system. Controlled amounts of aberrations or optical alignment errors can be analyzed for future trade-space choices in the design of the space-based system.

Evaluation of the Zemax models demonstrated that the realistic models of the GCTEx can be made. The paraxial model provides a tool for simulating the theoretical limits of the chromtomographic instrument. Additionally, it was an invaluable tool for developing the reconstruction algorithm and identification of the transverse offset.

The chromatic model demonstrated simulation results match those observed by the GCTEx. The chromatic simulations showed the reconstruction performance is degraded over most of the spectral range. It also shifts the spectral location of the best reconstructed image according to where the focus was set. The chromatic test

case also showed that the cone of missing information limits reconstruction of high spatial frequency objects.

The Zernike phase surface model was able to control amounts of spherical, astigmatism, and coma aberrations. The results showed that 1 wave of aberrations had little effect on the reconstruction performance. However, increasing the amount of aberrations to 5 waves, make the reconstructed images spatial features difficult to distinguish. Coma consistently negatively impacted the reconstruction performance more than the other two aberrations simulated. In designing the space-based system, reducing coma should be held as priority.

5.2 Fast Reconstruction Algorithm

The fast reconstruction algorithm demonstrated that it can reconstruct scenes spatial and spectral content. The filter applied by the reconstruction algorithm showed improved performance for most cases. There were test cases, such as the high spatial frequency object, where the performance of the filter was unacceptable. Despite its deficiencies, the fast reconstruction algorithm is able to reconstruct strong spatial and spectral features but its performance is limited due to the cone of missing information. The radiometric performance is not reliable as shifts in peaks and varying intensities were found. Additionally, the residual noise artifacts from the spectral channels are significant if left unfiltered. The algorithm would be well-suited for an input to iterative reconstruction algorithms.

5.3 Transverse Offset

The transverse offset was determined to be an alignment error in the prism, most likely from a rotation of a glass about the normal to the interface surface where the glasses meet. The total amount of lateral shift was measured to be 16.9 pixels, cor-

responding to an alignment error of 20.5 arc minutes. Since the transverse offset is symmetric, the corresponding correction is simple to implement by adding an additional shift to the reconstruction algorithm and not correcting for the transverse offset significantly degrades performance. Finally, the adjustment in the reconstruction algorithm and upgrade in electronics marked the first time AFIT was successful in reconstructing an a measured scene without manually manipulating the data.

5.4 Recommendations

The ground instrument is primed and ready for collecting more laboratory and field experiments. Simple tests such as investigating the effects of blurring due to the prism rotation need to be investigated. The effects of prism rotation blurring will determine how fast the prism can spin for a given camera integration time.

More field experiments are required to demonstrate that CTI is a palatable technology. Static scenes and spectrally interesting scenes are needed to affirm that the instrument is suitable as a spectrometer. Additionally, capturing transient events is a high priority objective for the project. The effects of transient events on the reconstruction algorithm need to be explored.

Prior to extensive laboratory and field experiments, a more advanced reconstruction algorithm is required to obtain radiometric precision. However, the fast reconstruction algorithm would serve as an excellent "quick look" algorithm that could be implemented onto a digital signal processor and provide near-real time reconstruction.

Finally, the Zemax and MATLAB combination serves as an excellent tool for future trade study design choices for the spaced-based system. Atmospheric effects or the slewing of the space station can be incorporated into the simulation to give a representative model of space-system mission.

Appendix A. Matlab Code

A.1   Fast Reconstruction Algorithm

```matlab
1  %% Min—norm Filtered Backprojection Reconstruction
2  % Chad Su'e
3  %%
4  %
5  close all;
6  %% Load the cine files and encoder position
7  %
8  if ~(exist('cameraFile') && exist('positionFile'))
9      [cameraFile cameraPath] = uigetfile('*.cin', 'Select the camera ...
           data file');
10     [positionFile positionPath] = uigetfile('*.mat', 'Select the ...
           adjusted position file');
11 end
12
13 if isequal(cameraFile,0) || isequal(positionFile,0)
14    error('Either camera or encoder data not selected')
15 end
16
17 %Load the Phantom Libraries to read in the cine files
18 if ~libisloaded('phfile') %phfile is the only library file really ...
      needed to convert data
19     %script was having troubles locating the drivers to read camera data
20     %so you will need to adjust the directory to where the ...
          PhantonSDK sits
21     %currDir = pwd;
22     %cd('C:\Users\Chad\Documents\MATLAB\Workspace\Phantom\PhMatlabSDK\Bin\x64\');
23     LoadPhantomLibraries(); %this will load all libraries
24     RegisterPhantom(true); %Register the Phantom dll's ignoring ...
          connected cameras.
25     %cd(currDir);
26 end
27
28 %% Create the cine handle from the cine file.
29 % This script does not support a batch of files
30 [HRES, cineHandle] = PhNewCineFromFile(fullfile(cameraPath,cameraFile));
31 if (HRES<0)
32     [message] = PhGetErrorMessage( HRES );
33     error(['Cine handle creation error: ' message]);
34 end
35 %% Find the range and bit depth
36 % Get the first image and image range of the cine file and the bit ...
      depth of
37 % the camera data. The image range is a subset of the total image count.
38 % The image range is defined by the Phantom software to converse ...
      image file
```

```matlab
39  % sizes
40  pFirstIm = libpointer('int32Ptr',0);
41  pImRange = libpointer('uint32Ptr',0);
42  pTotalImCount = libpointer('uint32Ptr',0);
43  PhGetCineInfo(cineHandle, PhFileConst.GCI_FIRSTIMAGENO, pFirstIm);
44  PhGetCineInfo(cineHandle, PhFileConst.GCI_IMAGECOUNT, pImRange);
45  PhGetCineInfo(cineHandle, PhFileConst.GCI_TOTALIMAGECOUNT, ...
        pTotalImCount);
46  imRange = pImRange.Value;
47  firstIm = pFirstIm.Value;
48  lastIm = int32(double(firstIm) + double(imRange) − 1);
49  totalImCount = int32(pTotalImCount.Value);
50
51  %Get cine image buffer size
52  pInfVal = libpointer('uint32Ptr',0);
53  PhGetCineInfo(cineHandle, PhFileConst.GCI_MAXIMGSIZE, pInfVal);
54  imgSizeInBytes = pInfVal.Value;
55
56  %Create the image range to be read. Unfortunately, the function ...
        calls are
57  %not working correctly to support multiple images at a time
58  imgRange = get(libstruct('tagIMRANGE'));
59  imgRange.Cnt = 1;
60  imgRange.First = 0; %used to determine the image size to preallocate ...
        imwrite
61  [HRES, unshiftedIm, imgHeader] = PhGetCineImage(cineHandle, ...
        imgRange, imgSizeInBytes);
62
63  %% Setup the spectral bins, load the collected frames then perform ...
        the 2D Fourier Transform
64  %
65
66  N = 50; %number of spectral bins
67  %wave = linspace(0.525,0.575,N);
68  wave = [0.4358335 0.546 0.576]; %Hg Pen
69  %wave = [0.58525 0.58819 0.59448 0.60962 0.61534 0.62173 0.62665 ...
        0.63344 ...
70  %    0.64016 0.65065 0.66010 0.66780 0.67170 0.69225 0.70283 0.72452 ...
        0.74889]; %Ne Pen
71  %wave = 0.546;
72
73  %Specify which dataset from the angular position make a full revolution
74  %imageSequence = int32([1163 1516 1868 2220]);%Hg Pen
75  imageSequence = int32(linspace(1163,2556,N)); %Hg Pen
76  %imageSequence = int32([234 594 950 1309]); %Ne Pen
77  %imageSequence = int32(linspace(1,1376,N)); %Ne Pen
78  %imageSequence = int32([19 109 198 287]); %Bar chart
79  %imageSequence = int32(linspace(1,356,N)); %Bar chart
80
81  %Load the angular position files and convert the image sequence to a
82  %negative range
83  load(fullfile(positionPath,positionFile))
```

```matlab
84  %1st col:timestamp(MJD), 2nd col:start position, 3rd col:  end position
85  xPixels = imgHeader.biWidth; yPixels = imgHeader.biHeight;
86  imageSequence=imageSequence−totalImCount;
87  M = length(imageSequence);
88
89  %read the camera files, transform into frequency space, and fuse angluar
90  %data
91  G = zeros(xPixels,yPixels,M);
92  prismAngle = zeros(M,1);
93  for m=1:M;
94      imgRange.First = imageSequence(m);
95      [HRES, unshiftedIm, imgHeader] = PhGetCineImage(cineHandle, ...
            imgRange, imgSizeInBytes);
96      if (HRES >= 0)
97          [unshiftedIm] = ...
                ExtractImageMatrixFromImageBuffer(unshiftedIm, imgHeader);
98          img = reshape(unshiftedIm',imgHeader.biWidth, ...
                imgHeader.biHeight);
99          g = double(img)/255;
100         G(:,:,m) = fft2(g);
101     end
102     prismAngle(m) = ...
            deg2rad(prismAngles(totalImCount+imageSequence(m),2)); %take ...
            the first angluar position
103 end
104
105 %% Setup the Prism Dispersion
106 %
107
108 %load prism dispersion from Zemax model to be more accurate
109 load 'prismDispersion.mat'
110 f3 = 85.0; %mm
111 pixPitch = 0.02; %mm per pixel
112 k = f3*tan(interp1(prismDispersion(:,1)',prismDispersion(:,2), wave));
113 N = length(wave);
114
115 %% Setup the spatial frequency
116 %
117 Fs = 1/pixPitch; %pixels per mm
118 %find the pixel sampling rate
119 dFx = Fs/xPixels;
120 dFy = Fs/yPixels;
121
122 %Setup the spatial frequency parameters as matlab likes it to properly
123 %shift the collected/simulated frames
124 Fx = [0:dFx:Fs/2−dFx  −Fs/2:dFx:−dFx];
125 Fy = [0:dFy:Fs/2−dFy  −Fs/2:dFy:−dFy]';
126 %Setup the Bessel filter for the reconstruction. Use a meshgrid, reshape
127 %the array, and for each spatial frequency, take the 1D−FFT wrt lambda
128 [X Y] = meshgrid(Fx,Fy);
129 R = sqrt(X.^2+Y.^2);
130 Mbess = 2*pi*besselj(0,2*pi*R(:)*k*0.001);
```

```matlab
131  Mbessel = reshape(Mbess,[size(X),length(wave)]);
132  Mfilter = fft(Mbessel,[],3);
133
134  %% Reconstruction
135  % Ready to reconstruct! For each spatial frequency, find A (an MxN) ...
          matrix
136  % then multiply by the measured data cube. Sum all of the ...
          projections to
137  % backprojection. A 1-D filter is then applied to acheive the Min-Norm
138  % solution. After applying the filter, take the inverse 2D fourier
139  % transform to obtain the hyper cube
140
141  R = 16.866*pixPitch;
142  %phase lag term
143  %offset = 0;
144  offset = deg2rad(-11.9242);
145  %offset = deg2rad(45);
146  whandle=waitbar(0);
147  Fprime = zeros(xPixels, yPixels,N);
148  for n=1:N
149      for m=1:M
150          phi = prismAngle(m);
151          Ax = exp(-2*pi*1i*(k(n)*sin(phi)+R*cos(phi+offset))*Fx);
152          Ay = exp(-2*pi*1i*(k(n)*cos(phi)-R*sin(phi+offset))*Fy);
153          % Force conjugate symmetry. Otherwise this frequency ...
                  component has no
154          % corresponding negative frequency to cancel out its ...
                  imaginary part.
155          Ax(xPixels/2+1) = real(Ax(xPixels/2+1));
156          Ay(yPixels/2+1) = real(Ax(yPixels/2+1));
157          Fprime(:,:,n) = G(:,:,m).*(Ay*Ax)+Fprime(:,:,n);
158      end
159      waitbar(n/N,whandle,'Backprojecting...')
160  end
161  close(whandle);
162  %% Apply the filter
163  %
164  mu = 1;
165  Fw = fft(Fprime,[],3);
166  Fmu = Fw ./(mu + Mfilter);
167  F = ifft(Fmu,[],3);
168
169  %% Take the inverse Fourier Transform to get the image cube
170  %
171  f = zeros(xPixels, yPixels, N);
172  fprime = zeros(xPixels, yPixels, N);
173  for n=1:N
174      fprime(:,:,n) = ifft2(Fprime(:,:,n))/M;
175      f(:,:,n)=real(ifft2(F(:,:,n)))/M;
176  end
```

A.2 Mercury Pen Lamp Simulation

```matlab
1  %% Mercury (Hg) Pen Lamp Simulation of GCTEx
2  % Capt Chad Su'e
3  %%
4  %
5  clear all
6  close all
7
8  %% Load and define simulation parameters
9  % Load common simulation parameters from simParams class and define
10 % specific parameters for this simulation
11
12 %Load default simulation parameters from class
13 hgSim = simParams();
14
15 %% Load & Initialize Zemax
16 %
17 zDDEInit(); %need an error check to determine if Zemax is open
18 zLoadFile(hgSim.modelPath);
19 zPushLens(1);
20
21 %% Load Image Simulation Parameters
22 %
23
24 % TODO: implement a shape vs time profile
25 imgSim = imgSimParams();
26 %imgSim.ISM_INPUTFILE = 'ALPHABET.IMA';
27 %imgSim.ISM_FIELDHEIGHT = 0.4;
28 imgSim.ISM_INPUTFILE = 'CIRCLE.IMA';
29 imgSim.ISM_FIELDHEIGHT = 0.02;
30 imgSim.updateSettings();
31
32 %% Set up prism angles
33 %
34
35 %For reconstruction, were are going to use 25 wavelength bins, so ...
       break the
36 %prism rotations into 25 equal rotations
37
38 %TODO: integrate the discrete nature of the encoder
39 %bins = 100;
40 bins = 36;
41 prismSteps = 360/bins;
42 prismAngles = linspace(0,360-prismSteps,bins);
43 hgSim.numAngles = length(prismAngles);
44
45
46 %% Configure the wavelength profile
47 %
```

```
48
49  wave = [0.4046565 0.4358335 0.5460750 0.5769610 0.5790670]; %um
50  waveIntensity = [4400 10000 10000 1100 1200];
51
52  waveIntensity = waveIntensity/max(waveIntensity);
53  hgSim.numWave = length(wave); %keep track in the simulation class
54
55  %% Start the simulation
56  %
57
58  %The text file is a large file size, so rather parsing a text file, ...
         Zemax
59  %allows for the simulation results to be output the sim as a rgb bitmap.
60  %The sim settings will always output a each wavelength iteration ...
         onto the
61  %blue channel and the text file is completely ignored. For each ...
         wavelength
62  %iteration, the sim output is normalized and then scaled. For each angle
63  %iteration, the wavelengths results are then summed and saved.
64
65  % simResults holds the sim outputs for each wavelength for every angle
66  g = zeros(hgSim.xPixels, hgSim.yPixels, hgSim.numAngles);
67  simResults = zeros(hgSim.xPixels, hgSim.yPixels);
68  tempResult = zeros(hgSim.xPixels, hgSim.yPixels);
69
70  whandle=waitbar(0);
71  for j = 1:hgSim.numAngles
72      %set the prism angle
73      zSetMulticon(1,1,prismAngles(j));
74      for k = 1:hgSim.numWave
75          waveData = zSetWave(1,wave(k),1);
76          status = zGetTextFile([hgSim.simTempResultPath ...
                 '\tempSimResult.txt'], 'Sim', hgSim.settingsFile, ...
                 hgSim.flag);
77          tempResult=imread([hgSim.simTempResultPath ...
                 '\tempSimResult.bmp']);
78          %get sim results from blue channel, normalize and then scale.
79          simResults=simResults+double(tempResult(:,:,3))/255*waveIntensity(k);
80      end
81      g(:,:, j) = simResults;
82      simResults = zeros(hgSim.xPixels, hgSim.yPixels);
83      waitbar(j/hgSim.numAngles,whandle,'Simulating...');
84  end
85  close(whandle);
86
87  %% Save simulation output and close DDE server
88  %
89
90  prismAngles = deg2rad(prismAngles);
91  save([hgSim.simResultsPath '\simout.mat'],'g','prismAngles','—mat');
92  zDDEClose();
```

A.3   Simulation Parameters

```matlab
1  classdef simParams
2      % % define the default properties of the simulation
3      properties(GetAccess = 'public', SetAccess = 'public')
4
5          %%Directory & Filename Path Parameters
6          modelPath = ...
               'C:\Users\Chad\Documents\MATLAB\Workspace\CTEx\Simulation\Models\GCTEx_Bosti
7          simResultsPath = ...
               'C:\Users\Chad\Documents\MATLAB\Workspace\CTEx\Simulation\hgSimResults';
8          simTempResultPath = 'C:\Users\Chad\Documents\ZEMAX\IMAFiles';
9          settingsFile = ...
               'C:\Users\Chad\Documents\ZEMAX\Configs\MySIM.CFG';
10
11          %%Prism Parameters
12          prismSpeed = 15;     %revolutions/second
13          numAngles;
14
15          %%Wavelength Parameters
16          numWave;
17
18          %%Image Simulation & Camera Parameters
19          INPUTFILE = 'CIRCLE.IMA'; % The input file in which to simulate
20          xPixels = 512;
21          yPixels = 512;
22          pixPitch = 0.02; %units: mm
23          flag = 1; %img sim settings: 0—default, 1—settings file, ...
                  2—prompt
24
25          %%Encoder Parameters %maybe add prism angles
26          encoderBitResolution = 12;
27          encoderResolution;
28
29      end
30
31      properties(Constant = true)
32          %add any constants here
33
34      end
35
36      methods
37          % methods, including the constructor are defined in this block
38          function obj = simParams()
39                  % class constructor
40                  obj.encoderResolution = 2^obj.encoderBitResolution;
41          end
42          %Define what Zemax model to load
43          function obj = setZemaxModel(obj,filePath)
44                  if(nargin > 0)
```

97

```matlab
45                  obj.modelPath = filePath;
46              else
47                  %add a filepath chooser
48              end
49          end
50          %Define the folder directory to store simulation results
51          function obj = setResultsDir(obj,dir)
52              if(nargin > 0)
53                  obj.simResultsPath = dir;
54              else
55
56              end
57          end
58      end
59 end
```

A.4 Image Simulation Parameters

```
1  classdef imgSimParams
2      %%Define the default properties of the simulation
3      properties(GetAccess = 'public', SetAccess = 'public')
4  % ISM_INPUTFILE: The input file name.
5  % ISM_FIELDHEIGHT: The Y field height.
6  % ISM_OVERSAMPLING: Oversample value. Use 0 for none, 1 for 2X, 2 ...
       for 4x,etc.
7  % ISM_GUARDBAND: Guard band value. Use 0 for none, 1 for 2X, 2 for ...
       4x, etc.
8  % ISM_FLIP: Flip Source. Use 0 for none, 1 for TB, 2 for LR, 3 for ...
       TB&LR.
9  % ISM_ROTATE: Rotate Source: Use 0 for none, 1 for 90, 2 for 180, 3 ...
       for 270.
10 % ISM_WAVE: Wavelength. Use 0 for RGB, 1 for 1+2+3, 2 for wave #1, 3 ...
       for wave#2, etc.
11 % ISM_FIELD: Field number.
12 % ISM_PSAMP: Pupil Sampling. Use 1 for 32x32, 2 for 64x64, etc.
13 % ISM_ISAMP: Image Sampling. Use 1 for 32x32, 2 for 64x64, etc.
14 % ISM_PSFX, ISM_PSFY: The number of PSF grid points.
15 % ISM_ABERRATIONS: Use 0 for none, 1 for geometric, 2 for diffraction.
16 % ISM_POLARIZATION: Use 0 for no, 1 for yes.
17 % ISM_SHOWAS: Use 0 for Simulated Image, 1 for Source Bitmap, and 2 ...
       for PSF Grid.
18 % ISM_REFERENCE: Use 0 for chief ray, 1 for vertex, 2 for primary ...
       chief ray.
19 % ISM_SUPPRESS: Use 0 for no, 1 for yes.
20 % ISM_PIXELSIZE: Use 0 for default or the size in lens units.
21 % ISM_XSIZE, ISM_YSIZE: Use 0 for default or the number of pixels.
22 % ISM_OUTPUTFILE: The output file name or empty string for no output ...
       file.
23         settingsFileName = ...
               'C:\Users\Chad\Documents\ZEMAX\Configs\MySIM.CFG';
24         ISM_INPUTFILE = 'CIRCLE.IMA';
25         ISM_FIELDHEIGHT = 0.02;
26         ISM_OVERSAMPLING = uint16(0);
27         ISM_GAURDBAND = uint16(0);
28         ISM_FLIP = uint16(0);
29         ISM_ROTATE = uint16(0);
30         ISM_WAVE = uint16(2)
31         ISM_FIELD = uint16(1)
32         ISM_PSAMP = uint16(1)
33         ISM_ISAMP = uint16(1)
34         ISM_PSFX = uint16(3)
35         ISM_PSFY = uint16(3)
36         ISM_ABERRATIONS = uint16(2)
37         ISM_POLARIZATION = uint16(0)
38         ISM_SHOWAS = uint16(0)
39         ISM_REFERENCE = uint16(1)
```

```matlab
40            ISM_SUPPRESS = uint16(0)
41            ISM_PIXELSIZE = 0.02
42            ISM_XSIZE = uint16(512)
43            ISM_YSIZE = uint16(512)
44            ISM_OUTPUTFILE = 'tempSimResult.bmp'
45        end
46        methods
47            % methods, including the constructor are defined in this block
48            function obj = imgSimParams()
49                % class constructor
50            end
51            function obj = updateSettings(obj)
52                zSetSettingsFile(obj.settingsFileName,'ISM_INPUTFILE', ...
                      obj.ISM_INPUTFILE);
53                zSetSettingsFile(obj.settingsFileName,'ISM_FIELDHEIGHT', ...
                      obj.ISM_FIELDHEIGHT);
54                zSetSettingsFile(obj.settingsFileName,'ISM_OVERSAMPLING', ...
                      obj.ISM_OVERSAMPLING);
55                zSetSettingsFile(obj.settingsFileName,'ISM_GAURDBAND', ...
                      obj.ISM_GAURDBAND);
56                zSetSettingsFile(obj.settingsFileName,'ISM_FLIP', ...
                      obj.ISM_FLIP);
57                zSetSettingsFile(obj.settingsFileName,'ISM_ROTATE', ...
                      obj.ISM_ROTATE);
58                zSetSettingsFile(obj.settingsFileName,'ISM_WAVE', ...
                      obj.ISM_WAVE);
59                zSetSettingsFile(obj.settingsFileName,'ISM_FIELD', ...
                      obj.ISM_FIELD);
60                zSetSettingsFile(obj.settingsFileName,'ISM_PSAMP', ...
                      obj.ISM_PSAMP);
61                zSetSettingsFile(obj.settingsFileName,'ISM_ISAMP',obj.ISM_ISAMP);
62                zSetSettingsFile(obj.settingsFileName,'ISM_PSFX',obj.ISM_PSFX);
63                zSetSettingsFile(obj.settingsFileName,'ISM_PSFY',obj.ISM_PSFY);
64                zSetSettingsFile(obj.settingsFileName,'ISM_ABERRATIONS',obj.ISM_ABERRATIONS);
65                zSetSettingsFile(obj.settingsFileName,'ISM_POLARIZATION',obj.ISM_POLARIZATIO
66                zSetSettingsFile(obj.settingsFileName,'ISM_SHOWAS', ...
                      obj.ISM_SHOWAS);
67                zSetSettingsFile(obj.settingsFileName,'ISM_REFERENCE', ...
                      obj.ISM_REFERENCE);
68                zSetSettingsFile(obj.settingsFileName,'ISM_SUPPRESS', ...
                      obj.ISM_SUPPRESS);
69                zSetSettingsFile(obj.settingsFileName,'ISM_PIXELSIZE', ...
                      obj.ISM_PIXELSIZE);
70                zSetSettingsFile(obj.settingsFileName,'ISM_XSIZE', ...
                      obj.ISM_XSIZE);
71                zSetSettingsFile(obj.settingsFileName,'ISM_YSIZE', ...
                      obj.ISM_YSIZE);
72                zSetSettingsFile(obj.settingsFileName,'ISM_OUTPUTFILE', ...
                      obj.ISM_OUTPUTFILE);
73            end
74        end
75  end
```

Appendix B. GCTEx Electrical System Block Diagram
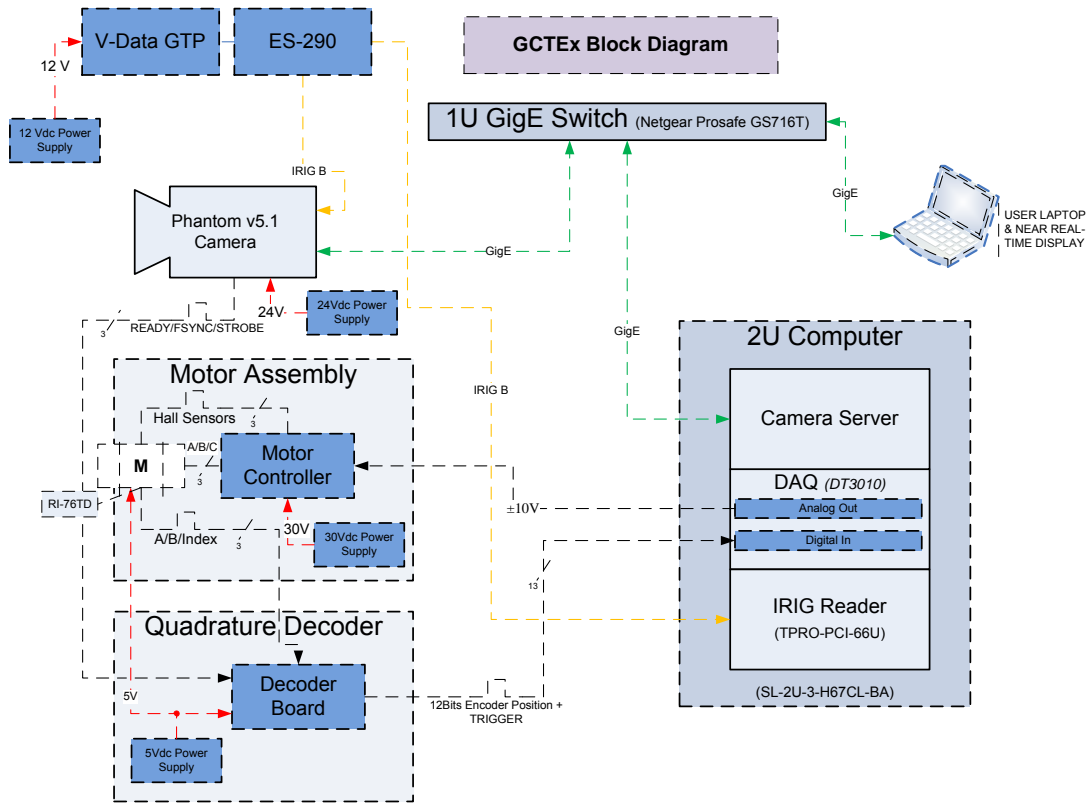
*Motor Assembly, Quadrature Decoder, & Power Supplies housed inside a 3U self

Bibliography

[1] Bayram, Sevinc, Ismail Avcibas, Bulent Sankur, and Nasir Memon. "Image manipulation detection". *Journal of Electronic Imaging*, 15(4):041102, 2006. URL http://link.aip.org/link/?JEI/15/041102/1.

[2] Bernhardt, P. A. "Direct reconstruction methods for hyperspectral imaging with rotational spectrotomography". *J. Opt. Soc. Am. A*, 12(9):1884–1901, Sep 1995. URL http://josaa.osa.org/abstract.cfm?URI=josaa-12-9-1884.

[3] Born, Max and Emil Wolf. *Principles of Optics*. Cambridge University Press, Cambridge, 7th edition, 1999.

[4] Bostick, Randall L. and Glen P. Perram. "Hyperspectral Imaging Using Chromotomography: A Fieldable Visible Instrument for Transient Events". *International Journal of High Speed Electronics and Systems*, 18, Issue 3:519–529, 2008.

[5] Bostick, Randall L., Glen P. Perram, and Ronald Tuttle. "Characterization of spatial and spectral resolution of a rotating prism chromotomographic hyperspectral imager". volume 7319, 731903. SPIE, 2009.

[6] Brodzik, Andrzej K. and Jonathan M. Mooney. "New iterative algorithm for restoration of chromotomographic images". volume 3438, 274–285. SPIE, 1998. URL http://link.aip.org/link/?PSI/3438/274/1.

[7] Brodzik, Andrzej K. and Jonathan M. Mooney. "Convex projections algorithm for restoration of limited-angle chromotomographic images". *J. Opt. Soc. Am. A*, 16(2):246–257, Feb 1999.

[8] Damera-Venkata, N., T. D. Kite, W. S. Geisler, B. L. Evans, and A. C. Bovik. "Image quality assessment based on a degradation model". 9(4):636–650, 2000.

[9] Dearinger, Anthony J. *Simulating a Chromotomographic Sensor for Hyperspectral Imaging in the Infrared*. Master's thesis, Air Force Institute of Technology, 2004.

[10] Deming, Ross W. "Chromotomography for a rotating-prism instrument using backprojection, then filtering". *Opt. Lett.*, 31(15):2281–2283, Aug 2006.

[11] Descour, Michael and Eustace Dereniak. "Computed-tomography imaging spectrometer: experimental calibration and reconstruction results". *Appl. Opt.*, 34(22):4817–4826, Aug 1995. URL http://ao.osa.org/abstract.cfm?URI=ao-34-22-4817.

[12] Eismann, M.T. *Hyperspectral Remote Sensing*. Unpublished, Dayton, OH, first edition, 2011.

[13] F. V. Bulygin, G. G. Levin, G. N. Vishnyakov and D. V. Karpukhin. "Spectrotomography- a new method of obtaining spectrograms of 2-D objects". *Opt. Spectrosc. (USSR)*, 71:561–563, 1991.

[14] Ford, Bridget K., Jose S. Salazar, and Mark P. Wilson. *Reconstruction Algorithm Development and Assessment for a Computed Tomography Based-Spectral Imager.* Technical report, Albuquerque, NM, 2005.

[15] Goodman, Joseph W. *Introduction to Fourier Optics.* Roberts and Company, Greenwood Village, CO, third edition, 2004.

[16] Gould, Malcom G. *Reconstruction of Chromotomographic Imaging System Infrared Hyperspectral Scenes.* Master's thesis, Air Force Institute of Technology, 2005.

[17] Griffith, Derek. "How to Talk to Zemax from Matlab", March 2012. URL `http://www.radiantzemax.com/kb-en/KnowledgebaseArticle50204.aspx?Keywords=matlab`.

[18] Gustke, Kevin C. *Reconstruction Algorithm Characterization and Performance Monitoring in Limited-Angle Chromotomography.* Master's thesis, Air Force Institute of Technology, Wright-Patterson Air Force Base, Ohio, 2004.

[19] Hagen, Nathan and Eustace L. Dereniak. "Analysis of computed tomographic imaging spectrometers. I. Spatial and spectral resolution". *Appl. Opt.*, 47(28):F85–F95, Oct 2008. URL `http://ao.osa.org/abstract.cfm?URI=ao-47-28-F85`.

[20] Hawks, Michael R. "MTF Correspondence". E-Mail, Feb 2012.

[21] Hawks, Michael R. "Transverse Offset Correspondence". E-Mail, Feb 2012.

[22] Hecht, Eugene. *Optics.* Addison-Wesley, forth edition, 2002.

[23] Holst, Gerald C. and Terrence S. Lomheim. *CMOS/CCD Sensors and Camera Systems.* SPIE Press, Bellingham, WA, 2nd edition, 2011.

[24] Hsieh, Jiang. *Computed Tomography.* SPIE Press, Bellingham, WA, second edition, 2009. ISBN 9780819480422.

[25] Janesick, James R. *Photon Transfer.* SPIE Press, Bellingham, WA, 2007. ISBN 9780819478382. URL `http://dx.doi.org/10.1117/3.725073`.

[26] Jet Propulsion Laboratory. "Airborn Visible/Infrared Imaging Spectrometer". Online, Feb 2012. URL `http://aviris.jpl.nasa.gov/aviris/`.

[27] Kaupa, Douglas F. *Structural and Thermal Design Analysis of a Space-Based Chromotomographic Hyperspectral Imaging Experiment.* Master's thesis, Air Force Institute of Technology, 2012.

[28] LeMaster, Daniel A. *Design and Model Verification of an Infrared Chromoto-mographic Imaging System.* Master's thesis, Air Force Institute of Technology, 2004.

[29] Mantravadi, S. "Spatial and Spectral Resolution Limits of Hyperspectral Imagers Using Computed Tomography: A Comparison". *Proc. IEEE Aerospace Conf*, 1–6. 2007.

[30] Mantravadi, Samuel and Stephen C. Cain. "Blind deconvolution of long exposure lens-based chromotomographic spectrometer data". volume 8165, 81650Q. SPIE, 2011. URL http://link.aip.org/link/?PSI/8165/81650Q/1.

[31] Mooney, Jonathan M. "Angularly multiplexed spectral imager". volume 2480, 65–77. SPIE, 1995. URL http://link.aip.org/link/?PSI/2480/65/1.

[32] Mooney, Jonathan M., Andrzej K. Brodzik, and Myoung H. An. "Principal component analysis in limited-angle chromotomography". volume 3118, 170–178. SPIE, 1997. URL http://link.aip.org/link/?PSI/3118/170/1.

[33] Murguia, James E., Toby D. Reeves, Jonathan M. Mooney, William S. Ewing, Freeman D. Shepherd, and Andrzej K. Brodzik. "Compact visible/near-infrared hyperspectral imager". volume 4028, 457–468. SPIE, 2000. URL http://link.aip.org/link/?PSI/4028/457/1.

[34] National Institute of Standards and Technology. "NIST Atomic Spectra Database Lines Form". Online, Feb 2012. URL http://physics.nist.gov/PhysRefData/ASD/lines_form.html.

[35] Niederhauser, Jason D. *Design and Characterization of a Space Based Chro-motomographic Hyperspectral Imaging Experiment.* Master's thesis, Air Force Institute of Technology, 2011.

[36] O'Dell, Daniel C. *Development and Demonstration of a Field-Deployable Fast Chromotomographic Imager.* Master's thesis, Air Force Institute of Technology, Wright-Patterson Air Force Base, Ohio, 2010.

[37] O'Dell, Daniel C., Randy Bostick, Michael R. Hawks, Eric D. Swenson, Jonathan T. Black, Richard G. Cobb, and Glen P. Perram. "Chromotomographic imager field demonstration results". volume 7668, 766804. SPIE, 2010.

[38] Sansonetti, Craig J., Marc L. Salit, and Joseph Reader. "Wavelengths of spectral lines in mercury pencil lamps". *Appl. Opt.*, 35(1):74–77, Jan 1996. URL http://ao.osa.org/abstract.cfm?URI=ao-35-1-74.

[39] Sato, Susumu. "Internal Focusing Telephoto Lens", 1994.

[40] Shibata, Satoru. "Optical System, Method for Focusing, and Imaging Apparatus Equipped Therewith", 2009.

[41] Vision Reseach Inc. "Phantom v640 Spectral Response". Online, Aug 2011. URL `http://www.visionresearch.com/uploads/docs/SpectralResponse`.

[42] Weisstien, Eric W. "Zernike Polynomial". MathWorld–A Wolfram Web Resource. URL `http://mathworld.wolfram.com/ZernikePolynomial.html`.

[43] Wyant, James C. and Katherine Creath. "Basic Wavefront Aberration Theory for Optical Metrology". *Applied Optics and Optical Engineering*, XI, 1992.

[44] Zemax Development Corporation. *Zemax User's Manual*, Feb 2011.

[45] Zygo Corporation. *MetroPro Reference Guide OMP-0347*, 2004.

REPORT DOCUMENTATION PAGE

1. REPORT DATE *(DD–MM–YYYY)*	2. REPORT TYPE	3. DATES COVERED *(From — To)*
22–03–2012	Master's Thesis	Aug 2011 — Mar 2012

4. TITLE AND SUBTITLE

Characterization of a Hyperspectral Chromotomographic Imaging Ground System

5a. CONTRACT NUMBER

5b. GRANT NUMBER

5c. PROGRAM ELEMENT NUMBER

6. AUTHOR(S)

Su'e, Chad B., Capt, USAF

5d. PROJECT NUMBER

5e. TASK NUMBER

5f. WORK UNIT NUMBER

7. PERFORMING ORGANIZATION NAME(S) AND ADDRESS(ES)

Air Force Institute of Technology
Graduate School of Engineering and Management (AFIT/EN)
2950 Hobson Way
WPAFB OH 45433-7765

8. PERFORMING ORGANIZATION REPORT NUMBER

AFIT/EE.ABET/ENP/12-M03

9. SPONSORING / MONITORING AGENCY NAME(S) AND ADDRESS(ES)

Intentionally Left Blank

10. SPONSOR/MONITOR'S ACRONYM(S)

11. SPONSOR/MONITOR'S REPORT NUMBER(S)

12. DISTRIBUTION / AVAILABILITY STATEMENT

DISTRIBUTION STATEMENT A
APPROVED FOR PUBLIC RELEASE; DISTRIBUTION UNLIMITED.

13. SUPPLEMENTARY NOTES

14. ABSTRACT

A field-deployable hyperspectral chromotomographic imager has been developed and tested as a risk-reduction prototype to assist design of a space-based system. The instrument uses a high-speed video camera looking through a rotating direct-vision prism to simultaneously observe the full field of view in all visible wavelength channels. The chromotomographic process multiplexes the spectral and spatial so an advanced reconstruction algorithm is required to separate the spectral channels. A physics-based model of the instrument was developed to assist in future trade-space choices for design of the spaced-based system. Additionally, the model is used for the development and assessment of the filtered backprojection reconstruction algorithm. Laboratory experiments from the field-deployable instrument were collected, and the results are compared to physics-based model predictions. Results from the simulated and experimental data show that the instrument and algorithm are capable of detecting spectral and spatial information of complex scenes.

15. SUBJECT TERMS

Hyperspectral Imagery, Chromotomography, Direct-Vision Prism, Image Reconstruction

16. SECURITY CLASSIFICATION OF:			17. LIMITATION OF ABSTRACT	18. NUMBER OF PAGES	19a. NAME OF RESPONSIBLE PERSON
a. REPORT	b. ABSTRACT	c. THIS PAGE			Lt Col Michael R. Hawks, AFIT/ENP
U	U	U	UU	122	19b. TELEPHONE NUMBER *(include area code)* (937) 255-3636, x4828; mhawks@afit.edu